



UNIVERSITY OF LEEDS

This is a repository copy of *Glimmerite: A product of melt-rock interaction within a crustal-scale high-strain zone*.

White Rose Research Online URL for this paper:

<https://eprints.whiterose.ac.uk/178161/>

Version: Accepted Version

---

**Article:**

Silva, D, Daczko, NR, Piazzolo, S [orcid.org/0000-0001-7723-8170](https://orcid.org/0000-0001-7723-8170) et al. (1 more author) (2022) *Glimmerite: A product of melt-rock interaction within a crustal-scale high-strain zone*. *Gondwana Research*, 105. pp. 160-184. ISSN 1342-937X

<https://doi.org/10.1016/j.gr.2021.09.005>

---

© 2021 International Association for Gondwana Research. This manuscript version is made available under the CC-BY-NC-ND 4.0 license <http://creativecommons.org/licenses/by-nc-nd/4.0/>.

**Reuse**

This article is distributed under the terms of the Creative Commons Attribution-NonCommercial-NoDerivs (CC BY-NC-ND) licence. This licence only allows you to download this work and share it with others as long as you credit the authors, but you can't change the article in any way or use it commercially. More information and the full terms of the licence here: <https://creativecommons.org/licenses/>

**Takedown**

If you consider content in White Rose Research Online to be in breach of UK law, please notify us by emailing [eprints@whiterose.ac.uk](mailto:eprints@whiterose.ac.uk) including the URL of the record and the reason for the withdrawal request.



[eprints@whiterose.ac.uk](mailto:eprints@whiterose.ac.uk)  
<https://eprints.whiterose.ac.uk/>

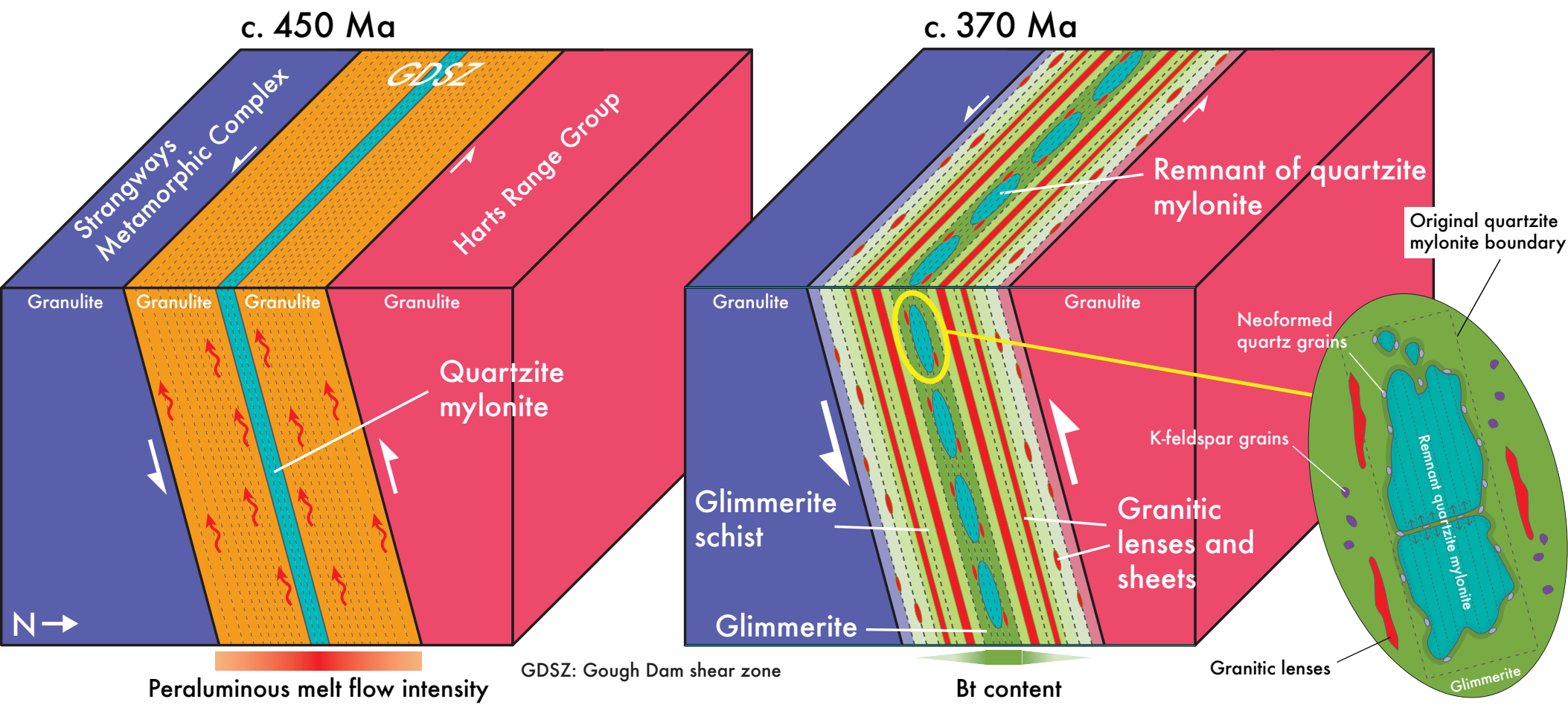
# Gondwana Research

## Glimmerite: a product of melt-rock interaction within a crustal-scale high-strain zone --Manuscript Draft--

<b>Manuscript Number:</b>	GWR-D-21-00082R2
<b>Article Type:</b>	Research Paper
<b>Keywords:</b>	Glimmerite; Metasomatism; High-strain zone; Monazite; Rheology
<b>Corresponding Author:</b>	David Silva, Ph.D. Macquarie University Sydney, NSW AUSTRALIA
<b>First Author:</b>	David Silva, Ph.D.
<b>Order of Authors:</b>	David Silva, Ph.D. Nathan R. Daczko, Associate Professor Sandra Piazzolo, Professor Tom Raimondo, Associate Professor
<b>Abstract:</b>	<p>The paradigm for hydrous high-strain zones that cut dry host rocks is for fluid-rock interaction to have involved aqueous fluids. However, the role of silicate melt is increasingly recognised. This contribution examines the formation of glimmerite (biotitite) bands during melt migration in the Gough Dam shear zone, a high-strain zone in central Australia that was active during the Alice Springs Orogeny (c. 450–300 Ma). The glimmerite bands cut and replace a range of quartzo-feldspathic protoliths, including granitic gneiss and quartzite. Melt that migrated through the high-strain zone is interpreted to have penetrated relict layers along a network of fractures, enhancing dissolution of the precursor rock and causing replacement by glimmerite crystallisation. Microstructures indicative of the former presence of melt in the high-strain zone include: pseudomorphs of former melt pockets of granitic composition; small dihedral angles of interstitial phases; elongate grain boundary melt pseudomorphs; neighbourhoods of grains connected in three dimensions; and localised static grain growth and recovery. Other microstructures indicative of melt-present deformation include randomly oriented neosome grains, and evidence of activation of multiple slip systems during deformation. The degree of quartzite modification to glimmerite is recorded by an increase in biotite mode, and correlated with higher Ti concentrations in biotite (higher apparent temperature) and changes to trace element and REE compositions. Melt-assisted coupled dissolution-precipitation reactions during melt flux are interpreted to partially reset Proterozoic monazite U-Pb ages inherited from the protolith (&gt; 1630 Ma) to younger Palaeozoic ages, with a complex age pattern partially congruent with the Alice Springs Orogeny (apparent ages range from c. 606–371 Ma, with a dominant age peak at c. 451 Ma). We propose that the glimmerite formed during dynamic melt migration of an externally-derived hydrous peraluminous melt, driving reaction replacement of various felsic protoliths during this orogenic event.</p>
<b>Response to Reviewers:</b>	

**D. Silva:** Conceptualization, Methodology, Formal analysis, Investigation, Writing - Original Draft, Visualization, Project administration, Funding acquisition. **N. R. Daczko:** Conceptualization, Methodology, Validation, Investigation, Writing - Review & Editing, Supervision, Project administration, Funding acquisition, Resources. **S. Piaolo:** Conceptualization, Methodology, Validation, Investigation, Writing - Review & Editing, Supervision, Project administration, Resources. **T. Raimondo:** Methodology, Validation, Investigation, Writing - Review & Editing, Resources.

- Reaction replacement glimmerite formed during dynamic hydrous melt migration
- Microstructures as evidence of former melt presence in high-strain zone
- Imperfect dissolution-precipitation reactions of monazite during melt flux
- Glimmerite layers in anhydrous terrains facilitates intracontinental orogenesis



# 1 **Glimmerite: a product of melt-rock interaction within a crustal-scale high-** 2 **strain zone**

3

4 D. Silva<sup>1\*</sup>, N. R. Daczko<sup>1</sup>, S. Piazzolo<sup>1,2</sup> and T. Raimondo<sup>3,4</sup>5 <sup>1</sup> ARC Centre of Excellence for Core to Crust Fluid Systems and GEMOC, Department of  
6 Earth and Environmental Sciences, Macquarie University, NSW 2109, Australia7 <sup>2</sup> School of Earth and Environment, Institute of Geophysics and Tectonics, University of Leeds,  
8 Leeds, LS2 9JT, United Kingdom9 <sup>3</sup> UniSA STEM, University of South Australia, GPO Box 2471, Adelaide, SA 5001, Australia10 <sup>4</sup> Future Industries Institute, University of South Australia, GPO Box 2471, Adelaide, SA 5001,  
11 Australia12  
13 \*Corresponding author. Email: david.barbosa-da-silva@students.mq.edu.au

## 15 **ABSTRACT**

16 The paradigm for hydrous high-strain zones that cut dry host rocks is for fluid-  
17 rock interaction to have involved aqueous fluids. However, the role of silicate melt is  
18 increasingly recognised. This contribution examines the formation of glimmerite (biotitite)  
19 bands during melt migration in the Gough Dam shear zone, a high-strain zone in central  
20 Australia that was active during the Alice Springs Orogeny (*c.* 450–300 Ma). The glimmerite  
21 bands cut and replace a range of quartzo-feldspathic protoliths, including granitic gneiss and  
22 quartzite. Melt that migrated through the high-strain zone is interpreted to have penetrated relict  
23 layers along a network of fractures, enhancing dissolution of the precursor rock and causing  
24 replacement by glimmerite crystallisation. Microstructures indicative of the former presence  
25 of melt in the high-strain zone include: pseudomorphs of former melt pockets of granitic  
26 composition; small dihedral angles of interstitial phases; elongate grain boundary melt

1  
2  
3  
4  
5  
6  
7  
8  
9  
10  
11  
12  
13  
14  
15  
16  
17  
18  
19  
20  
21  
22  
23  
24  
25  
26  
27  
28  
29  
30  
31  
32  
33  
34  
35  
36  
37  
38  
39  
40

pseudomorphs; neighbourhoods of grains connected in three dimensions; and localised static grain growth and recovery. Other microstructures indicative of melt-present deformation include randomly oriented neosome grains, and evidence of activation of multiple slip systems during deformation. The degree of quartzite modification to glimmerite is recorded by an increase in biotite mode, and correlated with higher Ti concentrations in biotite (higher apparent temperature) and changes to trace element and REE compositions. Melt-assisted coupled dissolution-precipitation reactions during melt flux are interpreted to partially reset Proterozoic monazite U-Pb ages inherited from the protolith (> 1630 Ma) to younger Palaeozoic ages, with a complex age pattern partially congruent with the Alice Springs Orogeny (apparent ages range from *c.* 606–371 Ma, with a dominant age peak at *c.* 451 Ma). We propose that the glimmerite formed during dynamic melt migration of an externally-derived hydrous peraluminous melt, driving reaction replacement of various felsic protoliths during this orogenic event.

31  
32  
33  
34  
35  
36  
37  
38  
39  
40  
41  
42

**Key words:** Glimmerite; Metasomatism; High-strain zone; Monazite; Rheology

## 43 1. INTRODUCTION

44  
45  
46  
47  
48  
49  
50  
51  
52  
53  
54  
55  
56  
57  
58  
59  
60  
61  
62  
63  
64  
65

Fluid (or the lack thereof) is key in crustal tectonometamorphic processes because it plays a major role in the progression of reactions, changes to mineral assemblages, metastability, activation of deformation processes and coupled rheological consequences (e.g., Yardley, 2009 and references therein). Both water or solute-rich fluids such as silicate melts have a first-order effect on a wide range of geochemical and deformation processes, acting as important agents at all scales. For example, fluids increase grain boundary mobility (e.g., Piazzolo *et al.*, 2002; Mancktelow & Pennacchioni, 2004), cause crystal hydrolytic weakening (e.g., Griggs & Blacic, 1965; Kronenberg *et al.*, 1990; Girard *et al.*, 2013) and rheological

1  
2  
3  
4  
5  
6  
7  
8  
9  
10  
11  
12  
13  
14  
15  
16  
17  
18  
19  
20  
21  
22  
23  
24  
25  
26  
27  
28  
29  
30  
31  
32  
33  
34  
35  
36  
37  
38  
39  
40  
41  
42  
43  
44  
45  
46  
47  
48  
49  
50  
51  
52  
53  
54  
55  
56  
57  
58  
59  
60  
61  
62  
63  
64  
65  
66  
67  
68  
69  
70  
71  
72  
73  
74  
75  
76  
77  
78  
79  
80  
81  
82  
83  
84  
85  
86  
87  
88  
89  
90  
91  
92  
93  
94  
95  
96  
97  
98  
99  
100

weakening through fluid overpressure (e.g., Thompson & Connolly, 1992; Sibson, 1994), induce water-fluxed melting (e.g., Weinberg & Hasalová, 2015 and references therein), facilitate metasomatism (e.g., Etheridge *et al.*, 1983; Ferry, 1994; Putnis & Austrheim, 2010), enable fast intra- and inter-grain diffusion pathways (e.g., Watson & Baxter, 2007; Wheeler, 2014; Chapman *et al.*, 2019; Gonçalves *et al.*, 2021), and drive coupled dissolution-precipitation replacement reactions (e.g., Putnis & Putnis, 2007; Putnis, 2009; Seydoux-Guillaume *et al.*, 2012). These fluid-aided processes can have major effects at the macroscale for the exhumation of deep crust (e.g., Raimondo *et al.*, 2014 and references therein), rates and style of subduction (e.g., Pichon *et al.*, 1993; Stern, 2002), arc volcanism (e.g., Morris *et al.*, 1990; Sobolev & Chaussidon, 1996; Schmidt & Poli, 1998), and progression and character of orogenesis (e.g., Beaumont *et al.*, 2001; Bercovici, 1998; Jamieson *et al.*, 2011).

Externally sourced fluids are commonly in disequilibrium with the host rocks through which they migrate and are therefore likely to trigger mineral reactions (Yardley, 2009; Putnis, 2009). The most extreme examples of fluid-rock interaction and associated reaction are usually observed in high-strain zones where time-integrated fluid fluxes and reactive surface area at any one time are high and fluid migration is channelised (Etheridge *et al.*, 1983; Oliver *et al.*, 1990; Selverstone *et al.*, 1991; Cartwright & Barnicoat, 2003; Clarke *et al.*, 2005; Daczko *et al.*, 2016; Stuart *et al.*, 2016, 2017, 2018a). In these cases, the rheological consequences are pronounced and fall into four general categories: (i) fluid-rock interaction results in the production of minerals that have a different rheological behaviour to their precursors (e.g., Brodie & Rutter, 1985; Wintsch *et al.*, 1995; Smith *et al.*, 2015); (ii) fluids cause grain size changes that may change the dominant deformation mechanism (Smith *et al.*, 2015; Menegon *et al.*, 2015); (iii) fluids change the rate of the dominant deformation mechanism (e.g., Karato, 1986); and/or (iv) the actual physical presence of the fluid itself has a rheological effect (e.g., Faulkner & Rutter, 2001; Handy *et al.*, 2001).

77                   Until recently, the study of hydrated high-strain zones has been focused on those  
78 that experienced interaction with water-rich fluids, most commonly during retrograde  
79 metamorphic conditions (e.g., White & Knipe, 1978; McCaig *et al.*, 1990; Menegon *et al.*,  
80 2008; Gonçalves *et al.*, 2012). Often, such fluid-fluxed areas exhibit extensive metasomatism,  
81 changing not only the mineral assemblage but also the bulk chemistry of the fluid-fluxed rock  
82 (e.g., Spruzeniece & Piazzolo, 2015 and references therein). However, recently it has been  
83 shown that hydration and strain localisation can also occur when a hydrous silicate melt fluxes  
84 lower crustal rocks in the roots of magmatic arcs (Daczko *et al.*, 2016; Stuart *et al.*, 2016, 2017,  
85 2018a; Meek *et al.*, 2019). In these cases, the main hydrous minerals produced are amphibole  
86 and clinozoisite, controlled by the mafic to intermediate silicate melts inferred to have migrated  
87 through the actively deforming high-strain zone. A similar process of melt-rock interaction as  
88 melt migrates up high-strain zones has also recently been recognised in mid-crustal granulite  
89 facies rocks of central Australia during the Alice Springs Orogeny (Ghatak, 2017; Piazzolo *et*  
90 *al.*, 2020). In this particular case, melt metasomatism is inferred to have involved hydrous  
91 peraluminous melts and produced metasomatic rocks rich in biotite and garnet at pressures of  
92 6–8 kbar. The enrichment in biotite and garnet, and depletion (i.e., replacement) of quartz and  
93 feldspar in precursor rocks suggests that melt temperatures were close to the liquidus, where  
94 fewer minerals are in equilibrium with the high-temperature melt (i.e., at temperatures above  
95 the stability of quartz and feldspar such that these dissolve into the melt; Ghatak, 2017).

96                   Due to the increased porosity and permeability that accompanies deformation,  
97 high-strain zones are ideal pathways for fluid migration, either by aqueous fluids or melts (e.g.,  
98 White & Knipe, 1978; Hutton, 1988; McCaig & Knipe, 1990; D’lemos *et al.*, 1992; Brown &  
99 Solar, 1998; Rosenberg, 2004; Menegon *et al.*, 2008; Menegon *et al.*, 2015; Stuart *et al.*, 2018a;  
100 Etheridge *et al.*, 2020; Gonçalves *et al.*, 2012, 2021). Both types of fluid migration in high-  
101 strain zones are well understood and easily recognised if, in the case of melt, a certain threshold

102 of interconnected fluid (> 10%) is present during deformation (e.g., Brown & Solar, 1998;  
103 Collins & Sawyer, 1996; Weinberg & Hasalová, 2015; Závada *et al.*, 2018). Such high  
104 proportions are suggested in the field by the high percentage of leucosome (Sawyer, 2008). In  
105 contrast, lower proportions of melt in a deforming rock (< 10%) will have limited rheological  
106 effect (Rosenberg & Handy, 2005), although this is debatable.

107           However, a lack of field evidence for high proportions of melt does not exclude  
108 the possibility of melt-present rheological weakening, because during the last stages of  
109 deformation the melt phase may have been largely evacuated (Schulmann *et al.*, 2008; Stuart  
110 *et al.*, 2018b). Additionally, recent work has shown that high-strain rocks lacking typical sub-  
111 solidus crystal-plastic deformation microstructures (e.g., crystallographic preferred  
112 orientations, dynamic recrystallisation, undulose extinction) may be used as an indicator of  
113 melt-present deformation and are suggestive of weakened rocks (Stuart *et al.*, 2018b). Key  
114 microstructures used to recognise former melt flux through high-strain zones include: (1) small  
115 dihedral angles of interstitial phases; (2) elongate interstitial grains; (3) neighbourhoods of  
116 quartz or feldspar grains connected in three dimensions; (4) fine-grained multiphase aggregates  
117 representing crystallised melt pockets or inclusions (e.g., Cesare *et al.*, 2015; Meek *et al.*,  
118 2019); and (5) mm- to cm-scale felsic dykelets (Stuart *et al.*, 2018b). Other melt  
119 microstructures such as those observed in migmatites (Sawyer, 1999; Vernon, 2011) may also  
120 be useful indicators of melt-present deformation in high-strain zones.

121           Glimmerite (“biotitite” in the IUGS classification) is defined as rock with a very  
122 high proportion of mica (> 75%, mainly biotite or phlogopite) and has been reported globally  
123 in diverse geological settings (e.g., Waters, 1987; Rakotondrazafy *et al.*, 1997; Becker *et al.*,  
124 1999; Fuertes-Fuente *et al.*, 2000; Grégoire *et al.*, 2002; Rajesh *et al.*, 2004; Lin & Sawyer,  
125 2019). Glimmerite is exceptionally hydrous, and its bulk composition does not resemble any  
126 classic sedimentary or igneous rock type, apart from small-scale gradational concentrations of

127 mafic minerals in granites and migmatites, i.e., schlieren (Weinberg *et al.*, 2001; Milord &  
128 Sawyer, 2003; Žák *et al.*, 2008). Hence, it is likely that glimmerites represent rocks that have  
129 undergone extreme chemical change or metasomatism *sensu lato* (*s.l.*). The most commonly  
130 reported occurrence of glimmerite is associated with highly metasomatised mantle rocks  
131 caused by interaction with a percolating melt/fluid (e.g., Becker *et al.*, 1999; Grégoire *et al.*,  
132 2002; Smart *et al.*, 2019). Glimmerites have also been reported to occur adjacent to granitic  
133 intrusions in mantle rocks (e.g., Fuertes-Fuente *et al.*, 2000), carbonatite intrusions and  
134 associated fenitisation of surrounding rocks (e.g., Tappe *et al.*, 2006; Elliott *et al.*, 2018) and  
135 have been interpreted to represent progressive fractional crystallisation of mantle melts injected  
136 into the lower crust (e.g., Rajesh *et al.*, 2004).

137           Contrary to these latter examples, the glimmerite studied here is located in a  
138 high-strain zone known as the Gough Dam shear zone, central Australia. They are spatially  
139 adjacent to and/or surrounded by felsic mid-crustal rocks (granitic and felsic granulitic  
140 gneisses). The chosen field example forms part of a regional-scale, 10 km long and 2–4 km-  
141 thick belt of glimmerite and other biotite-rich schistose rocks of varying biotite mode. In this  
142 contribution, we explore the mechanism of formation of glimmerite by examining well-  
143 exposed continuous outcrops that allow detailed field and multi-technique analysis. Based on  
144 the glimmerite assemblage, geochemistry, deformation, reaction textures and geochronology,  
145 we suggest that this intriguing rock type formed as a consequence of extreme melt-rock  
146 interaction during peraluminous melt migration through high-strain zones during orogenesis.

147

## 148 **2. GENERAL GEOLOGICAL BACKGROUND**

149           The area of interest lies in the Strangways Metamorphic Complex (SMC),  
150 Arunta Region, central Australia. This basement terrane is a broad belt of dominantly  
151 anhydrous upper amphibolite and granulite facies rocks, up to ~125 km wide, metamorphosed

152 during the Strangways Event at *c.* 1735–1690 Ma (Fig. 1) (Shaw *et al.*, 1984; Collins &  
153 Teyssier, 1989; Claoué-Long *et al.*, 2008; Scrimgeour, 2003, 2013). Subsequently, it was  
154 extensively reworked during the Alice Springs Orogeny (ASO), an intracontinental orogeny  
155 active during the middle to late Palaeozoic (450–300 Ma) (Collins & Teyssier, 1989; Raimondo  
156 *et al.*, 2014). This event caused crustal thickening and deep exhumation of ensialic granulitic  
157 basement in the Arunta Region, resulting in an orogen with an estimated horizontal shortening  
158 of up to 100 km at its eastern margin (Shaw *et al.*, 1984; Teyssier, 1985; Collins & Teyssier,  
159 1989; Fig. 1). An extensive regional network of anastomosing, km-wide high-strain zones  
160 bounding the Strangways Metamorphic Complex were reactivated during the ASO, facilitating  
161 much of the observed exhumation (e.g., Cartwright *et al.*, 1999; Hand & Sandiford, 1999;  
162 Mawby *et al.*, 1999; Ballèvre *et al.*, 2000; Scrimgeour, 2013; Raimondo *et al.*, 2011, 2014;  
163 Prent *et al.*, 2020; Fig. 1). These schistose high-strain zones include the West Bore shear zone  
164 and Gough Dam shear zone at the northern boundary of the SMC, and the Harry Creek shear  
165 zone toward the south.

166 Shear zones in the Arunta Region display hydrous mineral assemblages with  
167 high modal proportions of biotite and muscovite (e.g., SMC and Reynolds-Anmatjira Ranges  
168 (Fig. 1; Raimondo *et al.*, 2011, 2014). In the Reynolds-Anmatjira Ranges, hydrous shear zones  
169 are linked to metasomatic processes and retrogression of amphibolite facies rocks and gneisses,  
170 instead of common alternatives such as stress-induced mineral segregation or highly evolved  
171 schlieren bands (Cartwright & Buick, 1999; Raimondo *et al.*, 2011, 2012; Prent *et al.*, 2020).  
172 Similar to the Reynolds-Anmatjira Ranges, the SMC is cut by shear zones forming broad  
173 hydrous schist belts containing a high proportion of micas. These shear zones and schist belts  
174 are interpreted as strongly deformed and hydrated versions of granulite precursor rocks, which  
175 formed at deeper crustal levels when compared to those of the Reynolds-Anmatjira Ranges  
176 (Ballèvre *et al.*, 2000; Raimondo *et al.*, 2011, 2014).

177 The studied glimmerite occurs in the Gough Dam shear zone (GDSZ; labelled  
178 #1 in Fig. 1), located at the northern boundary of the Strangways Metamorphic Complex. The  
179 GDSZ trends roughly E-W to NNW-SSE, is steeply dipping (60–90°) to the north and presents  
180 a typical width of 1–2 km but can reach up to 4 km wide. The GDSZ is interpreted to have  
181 deformed in the presence of externally-derived melt that induced reaction softening and  
182 rheological weakening (Piazolo *et al.*, 2020). The high-strain zone is described as a significant  
183 tectonic discontinuity in the Arunta Region, controlling crustal block separation and reverse  
184 south-directed thrusting of the Harts Range Group relative to the Strangways Metamorphic  
185 Complex, kinematically informed by shear bands and sigma tails around porphyroclasts  
186 (Collins & Shaw, 1995; Bendall, 2000; Fig. 1). The GDSZ high-strain zone is characterised by  
187 hydration of the bimodal interlayered mafic-felsic granulites, quartzo-feldspathic and quartzite  
188 gneisses, and minor calcsilicate and amphibolite rocks constituting the Paleoproterozoic  
189 basement of the Arunta Region.

190

## 191 **2. 1. Gough Dam shear zone field relationships**

192 The GDSZ features several different rock types throughout the schist belt, the  
193 most recurrent being phyllonitic biotite-rich quartzo-feldspathic gneiss, felsic and mafic  
194 granulite pods of comparatively lower strain, and quartz-rich rafts (Norman, 1991; Ballèvre *et*  
195 *al.*, 1997). Some low-strain areas of the GDSZ include garnet-bearing granulites with garnet  
196 crystals up to 8 cm in diameter. A steeply northeast-dipping/plunging foliation/mineral  
197 lineation is defined by biotite and sillimanite, and locally kyanite. Highly strained rock types  
198 have variable bulk rock compositions and include granitic mylonite closer to the shear zone's  
199 southern boundary (Fig. 2a), and feldspar-biotite-quartz schist (identified hereafter in the text  
200 as glimmerite schist) with elongated granitic lenses located towards and in the centre of GDSZ  
201 (Fig. 2b, c). The width of granitic lenses increases towards the centre of GDSZ (Fig. 2b to 2c)

202 and these have been shown to have igneous microstructure consistent with syntectonic melt  
1  
2  
3 203 migration through the GDSZ (Piazolo *et al.*, 2020).

4  
5 204 The selected study area is localised in the central section of the GDSZ and  
6  
7 205 comprises an outcrop of approximately 10 m width by 15 m length of glimmerite schist, which  
8  
9 206 contains cm to dm scale lenses and layers of strained quartzite (up to 50 cm thick and 10 m in  
10  
11 207 length; Fig. 2d, g–i), and felsic granulite and granitic gneiss that are elongate parallel to the  
12  
13 208 schistose foliation (Fig. 2d–f). The matrix of the glimmerite schist is dominated by biotite  
14  
15 209 (~50%) and subordinate quartz, muscovite and sillimanite, with mm to cm-wide feldspar grains  
16  
17 210 (Fig. 2d–i). Within 200 m of the study area, kyanite and staurolite are also observed.  
18  
19 211 Centimetre-wide glimmerite sleeves (identified hereafter as glimmerite) with high proportions  
20  
21 212 of biotite (> 75%) are present adjacent to, cross-cutting, or ‘invading’ felsic bodies (i.e.,  
22  
23 213 quartzite mylonite, granitic gneiss and pegmatite), and dispersed as elongated lenses within  
24  
25 214 glimmerite schist (Fig. 2f–i). The relationships detailed at our study site are representative of  
26  
27 215 the most biotite-rich (i.e., most extensively hydrated) rocks within the hydrous shear zones of  
28  
29 216 the Alice Springs Orogen.  
30  
31  
32  
33  
34  
35

36 217 In the field, quartzite lenses exhibit classic mylonite features including a strong  
37  
38 218 alignment of biotite and quartz to form a steeply plunging lineation. Mylonitic foliations in  
39  
40 219 quartzite and foliations in granitic gneiss are parallel to the foliation in glimmerite schist (Fig.  
41  
42 220 2e, f). Quartzite mylonite and granitic gneiss are partially dismembered by perpendicular  
43  
44 221 fractures of mm to cm size, exhibiting a range of isolated lenses and blocks ranging from mm  
45  
46 222 to dm size (Fig. 2d–i). Glimmerite is seen in brittle fractures oriented perpendicular to the  
47  
48 223 foliation, and in embayments and irregular partings that define the lenses and blocks (Fig. 2d–  
49  
50 224 i), where it contains the same mineral assemblage as observed in the main glimmerite schist  
51  
52 225 unit. Field evidence suggests that there is a near continuum between quartzite mylonite,  
53  
54 226 glimmerite schist and glimmerite, with an increasing amount of biotite content from < 10%  
55  
56  
57  
58  
59  
60  
61  
62  
63  
64  
65

227 biotite (Bt) representing the original quartzite mylonite, to > 80% Bt in glimmerite (Fig. 2h, i).  
228 This progressive increase in Bt content, commonly associated with structural features such as  
229 fractures, suggests that there is a genetic relationship between Bt content and dismemberment.  
230 Hence, field observations suggest an association between chemical change (i.e., reduced quartz  
231 and feldspar content and increased Bt content), reaction and dismemberment commonly  
232 observed in metasomatic zones (Ferry, 1994).

233

### 234 3. SAMPLE SELECTION AND ANALYSIS

#### 235 3. 1. Sample selection

236 The majority of samples for this study (Fig. 2d–i and Fig. 4 onward) were  
237 collected along a transect in the central section of the Gough Dam shear zone (GPS coordinates  
238 23.1469°S, 134.56517°E, WGS84) and include components of quartz-rich mylonite and  
239 glimmerite, along with the contacts between them. The remaining samples (Fig. 2a–c and Fig.  
240 3) were collected close to the southern GDSZ boundary (Fig. 2a; GPS coordinates 23.1519°S,  
241 134.56388°E, WGS84) and approximately halfway towards the centre of GDSZ (Fig. 2b, c;  
242 GPS coordinates 23.1453°S, 134.56722°E, WGS84). The transect samples from the central  
243 GDSZ were selected to represent the observed change in Bt content from a highly quartz-rich  
244 mylonite (< 10 vol.% biotite) to glimmerite sleeves (> 80 vol.% biotite). We therefore selected  
245 a sequence of four domains represented by three hand specimens and thin sections: (i) low,  
246 < 10% Bt content, least-reacted quartzite (Sample L-Qtz [field ID number GD1609A]; Fig. 2h  
247 and 4a), (ii) medium, ~10% Bt content, medium-reacted quartzite (sample M-Qtz [field ID  
248 number GD1609C]; Fig. 2i and lower part of Fig. 4c), (iii) high, ~15% Bt content, highly-  
249 reacted quartzite (sample H-Qtz [field ID number GD1609B]; Fig. 2i and 4b) and (iv)  
250 glimmerite with > 80% Bt (Sample GL [field ID number GD1609C]; Fig. 2g–i and upper part  
251 of Fig. 4c). It should be noted that within one hand specimen [field ID number GD1609C], the

1  
2  
3  
4  
5  
6  
7  
8  
9  
10  
11  
12  
13  
14  
15  
16  
17  
18  
19  
20  
21  
22  
23  
24  
25  
26  
27  
28  
29  
30  
31  
32  
33  
34  
35  
36  
37  
38  
39  
40  
41  
42  
43  
44  
45  
46  
47  
48  
49  
50  
51  
52  
53  
54  
55  
56  
57  
58  
59  
60  
61  
62  
63  
64  
65

252 boundary between M-Qtz and GL is contained. Unless otherwise stated, the two parts of the  
253 same sample will be treated separately.

254

### 255 **3. 2. Methods of analysis**

#### 256 *3. 2. 1. Petrography and quantitative orientation analysis*

257 Polished thin sections were made from blocks cut perpendicular to foliation and  
258 parallel to lineation in both the quartz mylonite and glimmerite samples. Petrographic  
259 observations of the mineral assemblages were made using a petrographic microscope, the  
260 Virtual Petrographic Microscope (Tetley & Daczko, 2014) and ImageJ 1.47v (Rasband, 1997-  
261 2018). Microstructural/crystallographic characterisation of thin sections was performed using  
262 a FEI Quanta 650 FEG-ESEM with AZtec software and an Oxford/HKL Nordlys S EBSD  
263 system at the University of Leeds, UK. EBSD mapping was performed covering large areas of  
264 the thin section. Working conditions were 20 kV accelerating voltage, 20–26 mm working  
265 distance, 70° specimen tilt and a step size of 8 µm. Automatic indexation was performed using  
266 AZtec software (Oxford Instruments). HKL software was used to execute standard noise  
267 reduction and to extrapolate missing data using at least and in succession 8, 7, 6 and finally 5  
268 identical neighbours with similar orientation. Grain orientation maps using Euler angles and  
269 inverse pole figures (IPF) were generated using the MTEX package (Bachmann *et al.*, 2010;  
270 Henry *et al.*, 2017; Henry, 2018). Grains were calculated using a boundary angle > 10°  
271 misorientation. Dauphine twin boundaries for quartz were defined as quartz-quartz grain  
272 boundaries with a 60° rotation around the c-axis. Crystallographic preferred orientation (CPO)  
273 of quartz was assessed using pole figures plotted on lower hemisphere, equal area projections  
274 with one point per grain. J- and M-indices (Bunge, 2013; Skemer *et al.*, 2005) were computed  
275 to quantify the intensity of the CPO. Average grain size of minerals was determined using the  
276 EBSD data. We present grain size data where Dauphine twins were disregarded.

277

278 3. 2. 2. *Imaging and geochemical analysis*

279 Micro X-ray Fluorescence ( $\mu$ -XRF) analysis of the polished thin sections was  
280 used for mineral identification and spatial distribution mapping, quantification of modal  
281 proportions, and analysis of thin section-scale “whole-rock” major oxides.  $\mu$ -XRF analyses  
282 were performed using the Bruker M4 Tornado spectrometer at Macquarie University  
283 Geoanalytical (MQGA), Sydney, Australia. The  $\mu$ -XRF analyses were run with a tube voltage  
284 of 50 kV, a beam current of 200  $\mu$ A, a chamber pressure of 20 mbar, an acquisition time of 15  
285 ms/pixel and a step size of 25  $\mu$ m. AMICS (Advanced Mineral Identification and  
286 Characterization System) was used to convert the X-ray fluorescence spectra to produce  
287 detailed mineral maps.

288 High-resolution, high-sensitivity element mapping of polished thin sections on  
289 pure silica glass slides was performed to assess the trace element distribution within the reacted  
290 quartzite. Mapping was completed using the X-Ray Fluorescence Microscopy (XFM) beamline  
291 and the Maia-384 detector on the Kirkpatrick-Baez mirror microprobe at the Australian  
292 Synchrotron, Melbourne (Ryan *et al.*, 2010; Paterson *et al.*, 2011). A beam energy of 18.5 keV  
293 focussed to a 2  $\mu$ m spot size was used. Samples were scanned using a 4 mm step size in both  
294 the x and y directions, at a speed of 4 mm/s and a dwell time of 1 ms/pixel. A set of standard  
295 foils (Pt, Mn, Fe, YF3) were periodically analysed for calibration. Data reduction was  
296 performed using GeoPIXE (Ryan *et al.*, 1990), which uses the fundamental parameter model  
297 for the layered sample, the Maia detector efficiency model, and the DA matrix method to  
298 deconvolute spectra (Ryan *et al.*, 1995, 2015).

299 Backscatter Electron (BSE) images and associated Energy-dispersive X-ray  
300 spectroscopy (EDS) point analysis were used for both mineral identification and imaging of  
301 microstructures. Polished thin sections were carbon coated and imaged in a Hitachi Desktop

1  
2  
3  
4  
5  
6  
7  
8  
9  
10  
11  
12  
13  
14  
15  
16  
17  
18  
19  
20  
21  
22  
23  
24  
25  
26  
27  
28  
29  
30  
31  
32  
33  
34  
35  
36  
37  
38  
39  
40  
41  
42  
43  
44  
45  
46  
47  
48  
49  
50  
51  
52  
53  
54  
55  
56  
57  
58  
59  
60  
61  
62  
63  
64  
65

302 Scanning Electron Microscope (SEM) at the OptoFab node of the Australian National  
303 Fabrication Facility, Macquarie University, Sydney, Australia. The operating conditions of the  
304 SEM were low vacuum and 15 kV accelerating voltage. For rapid identification of monazite  
305 grains the BSE image based Mineral Liberation Analysis on the FEI 650 ESEM at the  
306 University of Tasmania, Australia, was used at low vacuum and 20 kV accelerating voltage.

307 Cathodoluminescence (CL) images were used to identify alteration of elemental  
308 concentration and/or crystallographic defects within quartz grains by migrating fluids  
309 interacting with the quartzite samples from the study area. The CL images were acquired using  
310 a Tescan VEGA3 XM SEM (University of Leeds, UK), operating at 20 kV and a beam current  
311 of 20 nA.

312 Electron microprobe (EMP) analysis was used to acquire compositional data of  
313 silicates using a JEOL JXA 8530F Plus field emission electron microprobe at the Central  
314 Science Laboratory, University of Tasmania. The instrument is equipped with a field emission  
315 source, running an accelerating voltage of 15 kV, a beam current of 15 nA and a beam size of  
316 10  $\mu\text{m}$ . The instrument has 5 wavelength dispersive spectrometers and is operated using the  
317 Probe Software Inc. "Probe For EPMA" software package. Plagioclase Lake County,  
318 Hornblende Kakanui, Augite Kakanui, Pyrope Kakanui, Olivine Springwater, Garnet Roberts  
319 Victor Mine (all Smithsonian; Jarosewich *et al.*, 1980) and Orthoclase from P&H  
320 Developments UK were analysed as secondary standards to confirm the quality of the analysis  
321 of the unknown material. A time dependent intensity correction was applied on Na and K if  
322 applicable. Oxygen was calculated by cation stoichiometry and included in the matrix  
323 correction. Hydrogen was calculated based on the mineral formula and included in the matrix  
324 correction as well. The matrix correction algorithm utilised was Armstrong/Love Scott  
325 (Armstrong, 1988) and the mass absorption coefficients dataset was LINEMU < 10 keV  
326 (Henke, 1985) and CITZMU > 10 keV (Heinrich, 1966).

327 Laser Ablation Inductively Coupled Plasma Mass Spectrometry (LA-ICP-MS)

328 was used to collect monazite U-Pb data for age determination using a Resonetics M-50-LR 193  
329 nm excimer laser coupled to an Agilent 7700x Quadrupole ICP-MS housed at Adelaide  
330 Microscopy, University of Adelaide. Data were collected from thin sections using 5 pre-  
331 ablation shots, 30 seconds of background measurement and 30 seconds sample ablation at 5  
332 Hz, 2 J/cm<sup>2</sup> fluence and a spot size of 19 or 13 µm. The raw data signal was reduced using  
333 Iolite software (Paton *et al.*, 2011). U-Pb fractionation was corrected using the MAdel monazite  
334 standard (TIMS normalisation data: <sup>207</sup>Pb/<sup>206</sup>Pb age = 492.01 ± 0.77 Ma; <sup>206</sup>Pb/<sup>238</sup>U age = 517.9  
335 ± 2.6 Ma; <sup>207</sup>Pb/<sup>235</sup>U age = 513.13 ± 0.20 Ma; updated from Payne *et al.* (2008) with additional  
336 TIMS analyses). Accuracy was also monitored by repeat analyses of the in-house internal  
337 standard 94-222/Bruna-NW (<sup>206</sup>Pb/<sup>238</sup>U = 450.2 ± 3.4 Ma; Maidment *et al.*, 2005).

338 The concentration of rare earth elements in biotite was determined in thin  
339 section using a Teledyne Analyte Excite 193 nm excimer laser coupled to an 7700x ICP-MS  
340 housed at Macquarie University Geoanalytical (MQGA), Sydney, Australia. Data were  
341 collected from thin sections using 30 seconds of background measurement and 30 seconds  
342 sample ablation at 10 Hz, 5 J/cm<sup>2</sup> fluence and spot size of 150 µm. Silicon (measured by EMP)  
343 was used as an internal standard for all minerals, and NIST 610 and 612, and basalt from the  
344 Columbia River (BCR-2) were used as external standards. The raw data signal was reduced  
345 using GLITTER software (Griffin, 2008).

346

### 347 3. 2. 3. Biotite and phengite geothermobarometers

348 The *P-T* conditions for each sample are estimated using the titanium-in-biotite  
349 thermometer of Henry *et al.* (2005) and the silicon-in-phengite geobarometer of Massonne &  
350 Schreyer (1987). The Henry *et al.* (2005) geothermometer is based on the titanium (Ti a.p.f.u.)  
351 composition of biotite in a peraluminous metapelite with Ti-bearing minerals (ilmenite or

352 rutile) and graphite in the mineral assemblage, equilibrated at 4–6 kbar. Temperature estimates  
353 are made by using the concentration of Ti, Fe and Mg in the biotite present in all samples (Table  
354 1 and Table S1). Compared to the Henry *et al.* (2005) experimental conditions for the  
355 geothermometer, the expected accuracy of the temperature estimates is approximately  $\pm 50^{\circ}\text{C}$ .  
356 This large error is due to the absence of graphite and accessory Ti-bearing minerals in the  
357 samples from this study (Fig. 4). Henry *et al.* (2005) describes the Ti-in-biotite temperature  
358 estimate calculations in the absence of Ti-saturating phases as being minimum temperatures  
359 estimates.

360 The Massonne & Schreyer (1987) geobarometer is based on the silicon (Si)  
361 composition in magnesium muscovite (phengite) coexisting with alkali feldspar,  
362 phlogopite/biotite and quartz. The maximum Si composition in phengite can only be attained  
363 using the geobarometer if the phengite coexists with the aforementioned mineral assemblage.  
364 For phengite present in glimmerite schist and glimmerite, the pressure estimates are expected  
365 to be precise since all the necessary minerals for the best pressure calculations are present (Fig.  
366 4). Phengite in quartzite does not coexist with alkali feldspar, limiting the estimates to a  
367 minimum pressure of formation (Fig. 4).

368

## 369 4. RESULTS

### 370 4.1. Petrography and microstructures

#### 371 4.1.1. Least Reacted Quartzite (sample L-Qtz; < 10 vol.% biotite)

372 Sample L-Qtz (field ID number GD1609A) contains the mineral assemblage  
373 quartz (Qz; ~90 vol.%), biotite (Bt; 8 vol.%) and magnetite (Mt; < 1 vol.%) (Fig. 4a), along  
374 with accessory zircon and monazite (see Section 4.4 for geochronology). The quartz grains  
375 show variable morphology from equant, mostly visible in the smaller grains (100  $\mu\text{m}$  to 1.5  
376 mm), to elongate and ribbon-like in the coarser grains (2 to 3.5 mm) that define small shear

1 377 bands (Fig. 4a). Most quartz grains show signs of high mobility of the grain boundaries as  
2 378 deeply sutured, curved and interlobate quartz-quartz boundaries (Fig. 4a). In areas of interstitial  
3  
4 379 biotite between quartz grains, the mobility of the quartz grain boundaries is retarded, from  
5  
6  
7 380 curved or lobate quartz-quartz boundaries to more rectilinear quartz-biotite boundaries (Fig.  
8  
9 381 4a).

11 Biotite grains in quartzite are light to dark green, usually of rectangular shape  
12 382  
13  
14 383 and show variable grain dimensions from 100  $\mu\text{m}$  to 5 mm in length and up to 1 mm in width  
15  
16  
17 384 (Fig. 4a). Magnetite and biotite are only locally associated and share straight grain boundaries.  
18  
19 385 However, magnetite has irregular boundaries with quartz. Biotite grains have a shape preferred  
20  
21  
22 386 orientation consistent with the tectonic reverse sense of shear (i.e., ASO mid-crustal terrane  
23  
24 387 exhumation) for the high-strain zone. Biotite is concentrated between quartz grains or in  
25  
26  
27 388 fractures present in quartzite (Fig. 4a).

28  
29 389

30  
31 390 *4. 1. 2. Highly Reacted Quartzite (sample H-Qtz; < 15 vol.% biotite)*

32  
33  
34 391 In comparison to sample L-Qtz, sample H-Qtz (field ID number GD1609B) is  
35  
36 392 similarly dominated by quartz (> 80 vol.%) and biotite (~15 vol.%), but has lower magnetite  
37  
38  
39 393 (a few isolated grains) and contains sillimanite (Sil; < 5 vol.%) (Fig. 4b, d) and accessory zircon  
40  
41 394 and monazite. Quartz grains generally display an elongate or ribbon-shaped morphology and  
42  
43  
44 395 are coarser than sample L-Qtz (Fig. 4b). The shape preferred orientation of the quartz  
45  
46 396 elongation is again consistent with the tectonic reverse sense of shear observed in the high-  
47  
48  
49 397 strain zone. Sample H-Qtz shares with sample L-Qtz a high degree of grain boundary mobility  
50  
51 398 in the quartz grains, recorded as deeply sutured, curved and interlobate quartz-quartz  
52  
53  
54 399 boundaries (Fig. 4b). However, in contrast to sample L-Qtz, sillimanite-rich bands are observed  
55  
56 400 where quartz-quartz boundaries are not as lobate (i.e., lower half of sample H-Qtz  
57  
58  
59  
60  
61  
62  
63  
64  
65

1  
2  
3  
4  
5  
6  
7  
8  
9  
10  
11  
12  
13  
14  
15  
16  
17  
18  
19  
20  
21  
22  
23  
24  
25  
26  
27  
28  
29  
30  
31  
32  
33  
34  
35  
36  
37  
38  
39  
40  
41  
42  
43  
44  
45  
46  
47  
48  
49  
50  
51  
52  
53  
54  
55  
56  
57  
58  
59  
60  
61  
62  
63  
64  
65

401 photomicrograph in Fig. 4b), inverting the overall boundary migration to more rectilinear  
402 quartz-quartz boundaries and to more common ribbon quartz morphology.

403           Biotite grains in sample H-Qtz are light to dark green, similar to the colouration  
404 observed in sample L-Qtz (Fig. 4d). In comparison with sample L-Qtz, there is a two-fold  
405 increase in biotite abundance, accompanied by an overall increase in grain size and the presence  
406 of contiguous bands (Fig. 4b). Biotite grains present rare finger-like protrusions into adjacent  
407 quartz grains and quartz-quartz boundaries (Fig. 5a–c). The protrusions terminate with low  
408 apparent dihedral angles between the quartz-quartz grains (Fig. 5b, c). Biotite and muscovite  
409 are locally intergrown, or muscovite truncates biotite (Fig. 5b, c). A sillimanite-biotite-rich  
410 band is observed in the ribbon quartz domains and is highlighted by blue arrows in Fig. 4. In  
411 this band (at left), a circular-shaped lens contains equigranular, euhedral to subhedral biotite,  
412 plagioclase, muscovite and quartz, with the biotite interlocked with the host quartz (Figs. 4b, d  
413 and 5a). A very fine-grained Al-Si-rich alteration product after plagioclase and sillimanite,  
414 inferred to be kaolinite or pyrophyllite (labelled on figures as Alt.), occurs in grain boundaries  
415 and micro-fractures (Figs. 4b, d, e and 5a).

416  
417 *4. 1. 3. Medium Reacted Quartzite (M-Qtz) and Glimmerite (GL) contact (composite sample*  
418 *M-Qtz/GL; ~10 vol.% and ~80 vol.% biotite)*

419           The M-Qtz and GL composite sample (field ID number GD1609C) includes the  
420 contact between a quartzite sample (labelled M-Qtz) similar in mode to H-Qtz described above  
421 and a glimmerite seam (labelled GL; both in Fig. 4c). The GL domain has 80 vol.% biotite, 8  
422 vol.% quartz, 6 vol.% sillimanite and 6 vol.% muscovite (Fig. 4c), along with accessory zircon  
423 and monazite (see Section 4.4 for geochronology).

424           Quartz grains in sample M-Qtz have strong similarities in their shape and  
425 boundary morphology to those previously described for sample H-Qtz. Dissimilar to H-Qtz,

1 426 unusually shaped quartz grains with complex embayment-like grain concavities and  
2 427 protrusions are observed in proximity to the large sillimanite-rich band present in the quartzite  
3  
4 428 (Figs. 4c and 5d, e). These unusually shaped quartz grains present a variation in  
5  
6  
7 429 crystallographic grain orientation less than or equal to  $10^\circ$  within the respective selected group  
8  
9  
10 430 (Fig. 6c, d). Multiple quartz grains near the quartzite-glimmerite contact are surrounded by  
11  
12 431 biotite, where biotite-filled embayments or fractures segment quartz grains with similar  
13  
14 432 crystallographic orientation (highlighted by white arrows in Fig. 6e).

15  
16  
17 433 Biotite in sample M-Qtz displays generally similar grain shape and  
18  
19 434 microstructure to that described for sample H-Qtz, with the presence of finger-like protrusions  
20  
21 435 into adjacent quartz-quartz boundaries (Fig. 5d). Sillimanite occurs in bands within the  
22  
23 436 quartzite in association with biotite (Figs. 4c and 6a), forming elongate prisms that contain  
24  
25 437 extension fractures perpendicular to the sense of elongation. An alteration product inferred to  
26  
27 438 be kaolinite or pyrophyllite is observed in the fractures (Fig. 5e).

28  
29  
30  
31 439 All the major minerals show a strong preferred orientation in the GL domain  
32  
33 440 (Fig. 5f). Similar to sample H-Qtz, biotite and muscovite are sometimes intergrown or truncate  
34  
35 441 each other (Fig. 5f), with muscovite truncating biotite more commonly. Sillimanite has an  
36  
37 442 elongate morphology similar to that observed in M-Qtz and H-Qtz samples, with fractures  
38  
39 443 perpendicular to their long axes (Fig. 5e), and is likewise concentrated into bands (Fig. 4c).  
40  
41 444 Some of the coarser muscovite grains show a sigmoidal shape with biotite wrapping around  
42  
43 445 the larger grains (Fig. 5f). A notable higher proportion of monazite and zircon grains is  
44  
45 446 observed in the GL component compared to the quartzite domain (i.e., M-Qtz) and the other  
46  
47 447 L-Qtz and H-Qtz samples (see Section 4.4 for geochronology).  
48  
49  
50

51  
52  
53 448 SEM cathodoluminescence (CL) images (Fig. 5g-j) show darker CL bands that  
54  
55 449 transgress single grains of quartz. The darker luminescence intensity is also observed at the  
56  
57 450 majority of quartz grain boundaries. These microstructures observed in the CL images are more  
58  
59  
60  
61  
62  
63  
64  
65

1 451 common in domains where biotite mode is higher (within or close to sample GL) (Fig. 5g, h),  
2 452 and are less common in domains with lower biotite mode (sample M-Qtz) (Fig. 5i, j).  
3

4  
5 453

#### 7 454 **4. 2. Quantitative quartz orientation analysis**

9  
10 455 Inverse pole figure (IPF) coloured maps for both the M-Qtz and H-Qtz samples  
11  
12 456 show a crystallographic preferred orientation (CPO) of quartz grains. The majority of grains  
13  
14 457 contain c-axes oriented perpendicular to the stretching lineation of the sample (Fig. 7a, d).  
15

16  
17 458 Crystallographic orientation data for quartz grains in samples M-Qtz, GL and  
18  
19 459 H-Qtz are plotted as pole figures (Fig. 7b, e). The J-index for all quartz grains in the mapping  
20  
21  
22 460 area is 2.86 and 3.35 for the composite M-Qtz/GL sample and H-Qtz sample, respectively (Fig.  
23  
24 461 7b, e). Sample M-Qtz/GL quartz CPO features a [c]-axis maximum parallel to the Z-axis and  
25  
26 462 spreading 45° in the NE sector of the pole figure. <a> axes define a distribution close to the  
27  
28  
29 463 primitive circle with a main cluster for the <a> axis at ~30–45° from X-axis (Fig. 7b).  
30

31 464 Results from the three regions delineated for the composite M-Qtz and GL  
32  
33  
34 465 sample map show a discrepancy in the quartz CPO, J- and M-index between the different  
35  
36 466 regions (region 1 vs regions 2 and 3), or put simply, sample GL vs sample M-Qtz (Fig. 7a, b).  
37  
38  
39 467 Region 1 quartz CPO presents a [c]-axis maximum close to the primitive circle at ~45° from X  
40  
41 468 and Y in the SE sector. This distribution of the <c> axes in region 1 contrasts from the observed  
42  
43  
44 469 <c> axes distribution close to Z for both regions 2 and 3 in sample M-Qtz. Overall, axes are  
45  
46 470 more randomly distributed in region 1, i.e., sample GL, when compared to regions 2 and 3, i.e.,  
47  
48  
49 471 sample M-Qtz (Fig. 7b). In regions 2 and 3, a clustering of <a> axes close to the primitive  
50  
51 472 circle is distinguishable (Fig. 7b).  
52

53 473 For quartz in sample H-Qtz, variations between regions are not as extreme as  
54  
55  
56 474 those observed for the composite M-Qtz/GL sample. The <c> axes in regions 1 and 2 are  
57  
58 475 similar to the entirety of quartz in the H-Qtz sample – a NE-SW oriented girdle. However, a  
59  
60  
61  
62  
63  
64  
65

1 476 [c]-axis maximum is observed in region 1 close to the primitive circle, whereas for region 2,  
2 477 the two maxima are close to Z. The <a> axes show similar orientation and distribution for both  
3  
4 478 regions, with a slightly greater girdle like distribution in region 1 (Fig. 7e).

5  
6  
7 479 The distribution of misorientation between pairs of quartz grains shows a higher  
8  
9 480 proportion of angles below 60° than that expected for a random quartz distribution for the  
10  
11 481 composite sample M-Qtz/GL (Fig. 7c), when compared to sample H-Qtz data (Fig. 7f). In  
12  
13 482 sample M-Qtz/GL, quartz misorientation contrasts between region 1 and the full sample quartz  
14  
15 483 misorientation data set (Fig. 7c). Region 1 shows a nearly perfect random distribution, whereas  
16  
17 484 sample M-Qtz/GL returns a stronger correlated misorientation distribution. H-Qtz quartz  
18  
19 485 misorientations are similar to sample M-Qtz/GL, a slightly correlated distribution below 60°  
20  
21 486 (Fig. 7f).

22  
23  
24 487 Mean area weighted (MAW) quartz grain size analysis was performed for the  
25  
26 488 regions of samples M-Qtz/GL and H-Qtz indicated in Fig. 7. A higher MAW quartz grain size  
27  
28 489 is observed for region 2 in sample M-Qtz (1752.63 mm<sup>2</sup>) and region 1 in sample H-Qtz  
29  
30 490 (1638.63 mm<sup>2</sup>), compared to region 3 (1258.39 mm<sup>2</sup>) and region 2 (1067.04 mm<sup>2</sup>) in samples  
31  
32 491 M-Qtz and H-Qtz, respectively. Quartz grains in sample GL have an order of magnitude lower  
33  
34 492 MAW quartz grain size (130.73 mm<sup>2</sup>) compared to the remaining regions described above (Fig.  
35  
36 493 8).

37 494

### 38 495 **4. 3. Geochemistry**

#### 39 496 *4. 3. 1. Glimmerite whole-rock major oxides*

40  
41 497 Harker diagrams for whole rock compositions of representative samples of the  
42  
43 498 Strangways Metamorphic Complex (SMC; Fig. 1), including ferromagnesian granulites,  
44  
45 499 quartzo-feldspathic granulites, metasedimentary rocks and the schistose high-strain zones that  
46  
47 500 cut them (Table S2), are compared with data from sample GL in Fig. 9. The felsic and mafic  
48  
49  
50  
51  
52  
53  
54  
55  
56  
57  
58  
59  
60  
61  
62  
63  
64  
65

1  
2  
3  
4  
5  
6  
7  
8  
9  
10  
11  
12  
13  
14  
15  
16  
17  
18  
19  
20  
21  
22  
23  
24  
25  
26  
27  
28  
29  
30  
31  
32  
33  
34  
35  
36  
37  
38  
39  
40  
41  
42  
43  
44  
45  
46  
47  
48  
49  
50  
51 granulites generally form a distribution similar to fractionation trends in igneous suites (e.g.,  
52 Winter, 2013; Frost & Frost, 2013). Data for granulite facies metasedimentary rocks of the  
53 SMC and the schistose high-strain zones largely follow the same trends, forming a distribution  
54 from lower SiO<sub>2</sub> metapelitic rocks to higher SiO<sub>2</sub> metapsammitic rocks. Quartzo-feldspathic  
55 granulites are distinct in their high SiO<sub>2</sub> content and lower concentrations of Al<sub>2</sub>O<sub>3</sub>, TiO<sub>2</sub>, FeO,  
56 and MgO. Data for schistose high-strain zones is difficult to distinguish from the geochemical  
57 pattern of metasedimentary rocks, having generally lower K<sub>2</sub>O concentrations. Sample GL has  
58 lower Al<sub>2</sub>O<sub>3</sub>, higher K<sub>2</sub>O and higher TiO<sub>2</sub> compared to the majority of the other rocks from  
59 schistose high-strain zones in the SMC, and lower concentration of TiO<sub>2</sub> and FeO compared to  
60 average biotite in peraluminous granite (Neiva *et al.*, 2002).

61  
62  
63  
64  
65

#### 66 4.3.2. Mineral major element chemistry and geothermobarometry

67  
68  
69  
70  
71  
72  
73  
74  
75  
76  
77  
78  
79  
80  
81  
82  
83  
84  
85  
86  
87  
88  
89  
90  
91  
92  
93  
94  
95  
96  
97  
98  
99  
100  
101  
102  
103  
104  
105  
106  
107  
108  
109  
110  
111  
112  
113  
114  
115  
116  
117  
118  
119  
120  
121  
122  
123  
124  
125  
126  
127  
128  
129  
130  
131  
132  
133  
134  
135  
136  
137  
138  
139  
140  
141  
142  
143  
144  
145  
146  
147  
148  
149  
150  
151  
152  
153  
154  
155  
156  
157  
158  
159  
160  
161  
162  
163  
164  
165  
166  
167  
168  
169  
170  
171  
172  
173  
174  
175  
176  
177  
178  
179  
180  
181  
182  
183  
184  
185  
186  
187  
188  
189  
190  
191  
192  
193  
194  
195  
196  
197  
198  
199  
200  
201  
202  
203  
204  
205  
206  
207  
208  
209  
210  
211  
212  
213  
214  
215  
216  
217  
218  
219  
220  
221  
222  
223  
224  
225  
226  
227  
228  
229  
230  
231  
232  
233  
234  
235  
236  
237  
238  
239  
240  
241  
242  
243  
244  
245  
246  
247  
248  
249  
250  
251  
252  
253  
254  
255  
256  
257  
258  
259  
260  
261  
262  
263  
264  
265  
266  
267  
268  
269  
270  
271  
272  
273  
274  
275  
276  
277  
278  
279  
280  
281  
282  
283  
284  
285  
286  
287  
288  
289  
290  
291  
292  
293  
294  
295  
296  
297  
298  
299  
300  
301  
302  
303  
304  
305  
306  
307  
308  
309  
310  
311  
312  
313  
314  
315  
316  
317  
318  
319  
320  
321  
322  
323  
324  
325  
326  
327  
328  
329  
330  
331  
332  
333  
334  
335  
336  
337  
338  
339  
340  
341  
342  
343  
344  
345  
346  
347  
348  
349  
350  
351  
352  
353  
354  
355  
356  
357  
358  
359  
360  
361  
362  
363  
364  
365  
366  
367  
368  
369  
370  
371  
372  
373  
374  
375  
376  
377  
378  
379  
380  
381  
382  
383  
384  
385  
386  
387  
388  
389  
390  
391  
392  
393  
394  
395  
396  
397  
398  
399  
400  
401  
402  
403  
404  
405  
406  
407  
408  
409  
410  
411  
412  
413  
414  
415  
416  
417  
418  
419  
420  
421  
422  
423  
424  
425  
426  
427  
428  
429  
430  
431  
432  
433  
434  
435  
436  
437  
438  
439  
440  
441  
442  
443  
444  
445  
446  
447  
448  
449  
450  
451  
452  
453  
454  
455  
456  
457  
458  
459  
460  
461  
462  
463  
464  
465  
466  
467  
468  
469  
470  
471  
472  
473  
474  
475  
476  
477  
478  
479  
480  
481  
482  
483  
484  
485  
486  
487  
488  
489  
490  
491  
492  
493  
494  
495  
496  
497  
498  
499  
500  
501  
502  
503  
504  
505  
506  
507  
508  
509  
510  
511  
512  
513  
514  
515  
516  
517  
518  
519  
520  
521  
522  
523  
524  
525  
526  
527  
528  
529  
530  
531  
532  
533  
534  
535  
536  
537  
538  
539  
540  
541  
542  
543  
544  
545  
546  
547  
548  
549  
550  
551  
552  
553  
554  
555  
556  
557  
558  
559  
560  
561  
562  
563  
564  
565  
566  
567  
568  
569  
570  
571  
572  
573  
574  
575  
576  
577  
578  
579  
580  
581  
582  
583  
584  
585  
586  
587  
588  
589  
590  
591  
592  
593  
594  
595  
596  
597  
598  
599  
600  
601  
602  
603  
604  
605  
606  
607  
608  
609  
610  
611  
612  
613  
614  
615  
616  
617  
618  
619  
620  
621  
622  
623  
624  
625  
626  
627  
628  
629  
630  
631  
632  
633  
634  
635  
636  
637  
638  
639  
640  
641  
642  
643  
644  
645  
646  
647  
648  
649  
650  
651  
652  
653  
654  
655  
656  
657  
658  
659  
660  
661  
662  
663  
664  
665  
666  
667  
668  
669  
670  
671  
672  
673  
674  
675  
676  
677  
678  
679  
680  
681  
682  
683  
684  
685  
686  
687  
688  
689  
690  
691  
692  
693  
694  
695  
696  
697  
698  
699  
700  
701  
702  
703  
704  
705  
706  
707  
708  
709  
710  
711  
712  
713  
714  
715  
716  
717  
718  
719  
720  
721  
722  
723  
724  
725  
726  
727  
728  
729  
730  
731  
732  
733  
734  
735  
736  
737  
738  
739  
740  
741  
742  
743  
744  
745  
746  
747  
748  
749  
750  
751  
752  
753  
754  
755  
756  
757  
758  
759  
760  
761  
762  
763  
764  
765  
766  
767  
768  
769  
770  
771  
772  
773  
774  
775  
776  
777  
778  
779  
780  
781  
782  
783  
784  
785  
786  
787  
788  
789  
790  
791  
792  
793  
794  
795  
796  
797  
798  
799  
800  
801  
802  
803  
804  
805  
806  
807  
808  
809  
810  
811  
812  
813  
814  
815  
816  
817  
818  
819  
820  
821  
822  
823  
824  
825  
826  
827  
828  
829  
830  
831  
832  
833  
834  
835  
836  
837  
838  
839  
840  
841  
842  
843  
844  
845  
846  
847  
848  
849  
850  
851  
852  
853  
854  
855  
856  
857  
858  
859  
860  
861  
862  
863  
864  
865  
866  
867  
868  
869  
870  
871  
872  
873  
874  
875  
876  
877  
878  
879  
880  
881  
882  
883  
884  
885  
886  
887  
888  
889  
890  
891  
892  
893  
894  
895  
896  
897  
898  
899  
900  
901  
902  
903  
904  
905  
906  
907  
908  
909  
910  
911  
912  
913  
914  
915  
916  
917  
918  
919  
920  
921  
922  
923  
924  
925  
926  
927  
928  
929  
930  
931  
932  
933  
934  
935  
936  
937  
938  
939  
940  
941  
942  
943  
944  
945  
946  
947  
948  
949  
950  
951  
952  
953  
954  
955  
956  
957  
958  
959  
960  
961  
962  
963  
964  
965  
966  
967  
968  
969  
970  
971  
972  
973  
974  
975  
976  
977  
978  
979  
980  
981  
982  
983  
984  
985  
986  
987  
988  
989  
990  
991  
992  
993  
994  
995  
996  
997  
998  
999  
1000

The totals for added H<sub>2</sub>O in biotite from all samples averages 3.97 wt% (Table 1 and Table S1). Biotite in sample L-Qtz has variable composition, whereas biotite in the remaining samples is relatively homogeneous (Table 1 and Table S1; Fig. 10a–c). Comparison between samples reveals a higher biotite TiO<sub>2</sub> content (ranging from 0.29 to 2.7 wt%) and Al<sub>2</sub>O<sub>3</sub> content (16.64 to 22.03 wt%) from sample L-Qtz to samples H-Qtz/GL (Table 1 and Table S1). Conversely,  $X_{Mg}$  [= Mg/(Fe+Mg)] is higher in sample L-Qtz relative to sample H-Qtz (Fig. 10a). Biotite compositions in all samples have moderate concentrations of F (average 0.71 wt%) and Cl (average 0.26 wt%; Table 1 and Table S1) compared to published igneous biotite data (Neiva *et al.*, 2002; Cesare *et al.*, 2008).

Fig. 10b employs the Nachit *et al.* (1985) biotite classification and the vast majority of biotite analyses (~90%) plot in the combined peraluminous fluid domain and overlap with igneous biotite data from Stussi & Cuney (1996). Samples H-Qtz, M-Qtz and GL plot tightly in the same region of the diagram, each cluster showing a minor range in Al and

1  
2  
3  
4  
5  
6  
7  
8  
9  
10  
11  
12  
13  
14  
15  
16  
17  
18  
19  
20  
21  
22  
23  
24  
25  
26  
27  
28  
29  
30  
31  
32  
33  
34  
35  
36  
37  
38  
39  
40  
41  
42  
43  
44  
45  
46  
47  
48  
49  
50  
51  
52  
53  
54  
55  
56  
57  
58  
59  
60  
61  
62  
63  
64  
65

526 Mg. In contrast, biotite from sample L-Qtz contains noticeably higher Mg and a broader range  
527 of values (Fig. 10b). Using the Nachit *et al.* (2005) biotite classification diagram (Fig. 10c),  
528 based on the assumption that the magmatic biotite composition (primary biotite) is altered with  
529 hydrothermal interaction (reequilibrated biotite) or neocrystallisation at equilibrium with that  
530 fluid (neoformed biotite), analyses from samples M-Qtz, H-Qtz and GL cluster within the  
531 reequilibrated biotite domain and adjacent to the primary biotite domain, whereas sample L-  
532 Qtz is scattered between the neoformed and reequilibrated domains (Fig. 10c).

533 A plot of Ti a.p.f.u. vs  $X_{Mg}$  shows a trend of increasing Ti with decreasing  $X_{Mg}$   
534 in biotite from samples L-Qtz to M-Qtz/GL (Fig. 10a). The application of the Ti-in-biotite  
535 thermometer of Henry *et al.* (2005) indicates highly variable minimum formation temperatures,  
536 300–570 ± 50°C for sample L-Qtz, ~630 ± 50°C for biotite in the quartzite and glimmerite  
537 domains of sample M-Qtz/GL, and ~660 ± 50°C for sample H-Qtz (Fig. 10d). In samples where  
538 phengite is present (H-Qtz and M-Qtz/GL), the Si-in-phengite geobarometer of Massonne &  
539 Schreyer (1987) was applied. Phengite from these samples has Al slightly lower than 3.1  
540 a.p.f.u., which in combination with the Ti-in-biotite thermometer (Henry *et al.*, 2005) allows  
541 us to discriminate their pressure of formation at ~5–6 kbar (Fig. 10d).

542

#### 543 4. 3. 3. Biotite trace element chemistry

544 For all samples, the biotite concentrations for Zr, Hf, Nb and Ta (Table 2 and  
545 Table S3) normalised to chondrite (McDonough & Sun, 1995) follow similar patterns. Zr  
546 values are consistently below chondrite (Fig. 11a–c), except for a single biotite analysis from  
547 the M-Qtz/GL sample (Fig. 11c). Hf values are likewise depleted but to a lesser extent (Fig.  
548 11a–c), except the distinctive Zr-enriched biotite grain conjointly enriched in Hf (Fig. 11c). In  
549 contrast, Nb and Ta show consistently enriched values (Fig. 11a–c). A distinction in Nb and  
550 Ta concentration is observed between the values for sample L-Qtz and the other samples (H-

551 Qtz and M-Qtz/GL), with the former having lower Nb concentrations (Figs. 11a–c), but with  
552 equivalent values of Ta (L-Qtz ~167–232; pair H-Qtz ~143–225 times chondrite; Table 2 and  
553 Table S3; Figs. 11a–c and 12).

554 Biotite compositions in all samples have a consistent depletion in rare-earth  
555 elements (REE) compared to the chondrite values (Table 2 and Table S3; Fig. 11a–c). Similar  
556 relations are observed for all chondrite-normalised REE patterns, with a small decrease in  
557 LREE trending down from La to Sm in comparison to the HREE (Fig. 11a–c). Compared to  
558 biotite in samples H-Qtz and M-Qtz/GL, sample L-Qtz shows less variability and a general  
559 increase in normalised LREE concentrations (Fig. 11a–c). Overall, biotite HREE patterns are  
560 concave-up due to higher Lu normalised concentrations relative to the remaining HREE.  
561 Pronounced positive Eu anomalies are evident for sample H-Qtz and the combined M-Qtz and  
562 GL biotite analyses (Fig. 11a–c), with a slightly smaller anomaly for sample L-Qtz.

563 Fig. 11d and Table S4 contain compilations of published values and sample  
564 descriptions for natural and experimental igneous and metamorphic biotite normalised to  
565 chondrite (McDonough & Sun, 1995). The Gough Dam samples have lower normalised  
566 concentrations of Zr, Hf and REE compared to the compiled data, but have similar values of  
567 Nb and Ta, especially in relation to the metapelitic peraluminous El Hoyazo enclaves (Fig. 11;  
568 Cesare *et al.*, 1997; Acosta-Vigil *et al.*, 2010) and the peraluminous migmatite biotite of Bea  
569 *et al.* (1994b).

570 Two groups of biotite composition are distinguishable on bivariate plots of Ba,  
571 Sc, Nb/Ta and Li versus Ti (Fig. 12). Sample L-Qtz is depleted compared to H-Qtz and the  
572 combined M-Qtz and GL biotite analyses, with the pooled data forming a positive correlation  
573 trend. The enrichment trend is also visible if compared to El Hoyazo biotite (Acosta-Vigil *et*  
574 *al.*, 2010), which plots as either the most Ba and Li enriched analyses or at equivalent Nb/Ta  
575 and Sc concentrations with samples H-Qtz, M-Qtz and GL (Fig. 12). Within the group of Nb-

1 576 enriched biotite (samples H-Qtz, M-Qtz and GL), Nb/Ta values above the chondritic  
2 577 concentrations of McDonough & Sun (1995) is observed for H-Qtz and the combined M-  
3  
4 578 Qtz/GL samples. In general, the order of Ba, Li and Sc in biotite concentration is observed as  
5  
6  
7 579  $L\text{-Qtz} < M\text{-Qtz/GL} \leq H\text{-Qtz}$ .

8  
9 580

#### 11 581 **4. 4. Geochronology (U-Pb monazite)**

12 582 Monazite grains from samples GL (higher biotite vol%; Fig. 13a–b) and M-Qtz  
13  
14 583 (lower biotite vol%; Fig. 13c–d) are generally located in contact with biotite and sillimanite,  
15  
16  
17 584 with few grains adjacent to or in contact with quartz grain boundaries or quartz fractures.  
18  
19 585 Monazite grains are rounded to elongate and commonly 50–200  $\mu\text{m}$  in the longest dimension  
20  
21  
22 586 (Fig. 14a), but with size range of  $\sim 30\text{--}200 \mu\text{m}$ . Several grains show zonation in BSE images,  
23  
24  
25 587 usually with a higher BSE response in core domains or multiple zones of variable BSE  
26  
27  
28 588 responses (Fig. 14a). Curved, inward-penetrating boundaries and cross-cutting textures are  
29  
30  
31 589 visible in some grains between core and rim domains. Thorite inclusions (after monazite) are  
32  
33  
34 590 mostly contained in brighter zones near grain boundaries or in micro-fractures (Fig. 14a). The  
35  
36 591 remaining monazite grains are mostly smaller ( $< 100 \mu\text{m}$ ) and do not display any observable  
37  
38  
39 592 BSE zonation.

40  
41 593 In all, 56 U-Pb spot analyses on 39 monazite grains from sample M-Qtz/GL  
42  
43 594 were obtained using LA-ICP-MS. Data with  $< 2\%$  discordance show two discernible age  
44  
45  
46 595 groups (Fig. 14b and Table S5): (i) Palaeoproterozoic ages ranging from  $1740 \pm 16 \text{ Ma}$  to  $1630$   
47  
48 596  $\pm 19 \text{ Ma}$  with a density age estimation at *c.*  $1669 \text{ Ma}$  (all located in sample M-Qtz); and (ii)  
49  
50  
51 597 Neoproterozoic to Palaeozoic ages ranging from  $606.1 \pm 5.8 \text{ Ma}$  to  $370.9 \pm 3.6 \text{ Ma}$  with a  
52  
53 598 density age estimation at *c.*  $451 \text{ Ma}$ . The remaining discordant analyses from sample M-Qtz fit  
54  
55  
56 599 a linear regression with an upper intercept age of  $1669 \pm 4.6 \text{ Ma}$  and a lower intercept age of  
57  
58 600  $482 \pm 2.5 \text{ Ma}$ , resulting in a high MSWD of 11 due to significant dispersion (Fig. 14b). The

1 majority of these analyses are spread along the discordia line towards its upper intercept, with  
2  
3 602 the remaining analyses together with those of sample GL forming a concordant but widely  
4  
5 603 spread Palaeozoic age group, creating a complex age distribution at the lower intercept (Fig.  
6  
7 604 14b).

8  
9 605 The obtained monazite ages are not homogeneously distributed throughout  
10  
11 606 samples M-Qtz and GL (Fig. 14 and Fig. S1). All the Early Palaeoproterozoic ages are derived  
12  
13 607 from sample M-Qtz, which also contains isolated grain clusters that record a spread of  
14  
15 608 Neoproterozoic-Palaeozoic ages (Fig. S1). In contrast, the adjacent glimmerite component  
16  
17 609 (sample GL) hosts monazite with a much narrower age range, with most monazite returning  
18  
19 610 Palaeozoic ages and a greater proportion falling within the age bounds of the ASO (*c.* 450–  
20  
21 611 300 Ma; Fig. 14 and Fig. S1). Discordant ages from both samples are derived from rim domains  
22  
23 612 and/or monazite grains with lower BSE response zones (Fig. 14a).

24  
25  
26  
27  
28  
29 613

## 30 31 614 **5. DISCUSSION**

### 32 33 34 615 **5.1. Conditions and timing of glimmerite formation**

35  
36 616 Combined petrography, mineral geochemistry and monazite geochronology  
37  
38 617 across the cm-scale transect of variably modified quartzites from the GDSZ provides insight  
39  
40 618 into the geological environment and *P-T-t* evolution responsible for their conversion to  
41  
42 619 glimmerite. The *P-T* estimation using mica in the studied samples suggests mid-crustal  
43  
44 620 conditions of  $P > 4\text{--}5$  kbar and  $T > 570\text{--}660^\circ\text{C}$  (Fig. 10), similar to previously published  
45  
46 621 conditions from the GDSZ and other Palaeozoic shear zones in the Strangways region (Ballèvre  
47  
48 622 *et al.*, 2000; Bendall, 2000). Due to the lack of graphite and Ti-bearing accessory minerals in  
49  
50 623 all samples, temperature estimates are minimum values. Note that this also influences the  
51  
52 624 pressure estimates, suggesting they are likewise minimum values. The upper end of the  
53  
54  
55  
56  
57  
58 625 calculated temperature range lies above the hydrous granite solidus and is consistent with field  
59  
60  
61  
62  
63  
64  
65

626 observations of syn-deformational granitic lenses in the GDSZ (Fig. 2e), along with  
627 microstructural evidence for the former presence of melt (Figs. 3 and 5; see Section 5.2).

628           The relationship between age and textural position of monazite grains in the  
629 studied samples suggests that the precursor quartzite initially experienced metamorphism  
630 during the Strangways Event (*c.* 1735–1690 Ma), followed by a subsequent metamorphic  
631 overprint during the Alice Springs Orogeny (*c.* 450–300 Ma) that is largely recorded in the  
632 cross-cutting glimmerite (Fig. 14). The morphology and zonation of the monazite grains (e.g.,  
633 inward-penetrating boundary interfaces, radial or spotted domains of lower BSE intensity,  
634 porous textures usually present near monazite rims and micro-fractures, and thorite inclusions  
635 near micro-fractures) suggests that they were modified by fluid-assisted (melt-assisted)  
636 coupled dissolution-precipitation reactions (Fig. 14a; Ruiz-Agudo *et al.*, 2014; Varga *et al.*,  
637 2020). The lower intercept age of *c.* 482 Ma intersects a significant spread of Neoproterozoic  
638 to Palaeozoic apparent ages (*c.* 606–371 Ma; Fig. 14). These complex age data can be  
639 interpreted in two ways: (i) the individual analyses are geologically meaningful and reflect  
640 multiple reactivation and fluid flow events in the GDSZ; or (ii) the data reflect partial age-  
641 resetting of inherited monazite grains during one or more Palaeozoic reactivation and fluid  
642 flow events in the GDSZ.

643           Coupled dissolution-precipitation experiments have demonstrated that the  
644 replacement of precursor monazite can be incomplete, either (i) forming nanomixtures of old  
645 and new monazite (Grand’Homme *et al.*, 2016, 2018); or (ii) imperfectly resetting inherited  
646 grains (Varga *et al.*, 2020). Temperature and other physicochemical parameters (i.e., fluid  
647 composition, mineral composition, solubility, primary zoning, stress, reaction kinetics) greatly  
648 affect the replacement mechanism that redistributes U-Pb cargo in the precipitated monazite  
649 (Ruiz-Agudo *et al.*, 2014; Grand’Homme *et al.*, 2016, 2018; Varga *et al.*, 2020). Additional  
650 detailed nano-scale studies of the monazite reaction front microstructures (i.e., nanocracks,

1  
2  
3  
4  
5  
6  
7  
8  
9  
10  
11  
12  
13  
14  
15  
16  
17  
18  
19  
20  
21  
22  
23  
24  
25  
26  
27  
28  
29  
30  
31  
32  
33  
34  
35  
36  
37  
38  
39  
40  
41  
42  
43  
44  
45  
46  
47  
48  
49  
50  
51  
52  
53  
54  
55  
56  
57  
58  
59  
60  
61  
62  
63  
64  
65

651 dislocations, pores/inclusions) are therefore necessary to better understand the exact extent of  
652 monazite partial age resetting and significance of the age spread observed in Fig. 14b. As such,  
653 we prefer the interpretation that the Neoproterozoic to Palaeozoic dates from individual  
654 monazite grains in this study are unlikely to be geologically meaningful. The younger age  
655 cluster ending at *c.* 370 Ma cannot be used to precisely date the timing of glimmerite formation,  
656 beyond stating that it aligns with the Alice Springs Orogeny.

657           Despite this, the spread of concordant ages across this interval may hold some  
658 utility in establishing the broad context for melt-rock interaction. Notably, the most significant  
659 age peak from the kernel density estimation occurs at *c.* 451 Ma (Fig. 14b), consistent with U-  
660 Pb monazite ages from similar shear zones of the Strangways Range (Möller *et al.*, 1999;  
661 Howlett *et al.*, 2014; Fournier *et al.*, 2016). This timing reflects the earliest onset of the Alice  
662 Springs Orogeny recorded regionally (Mawby *et al.*, 1999; Raimondo *et al.*, 2014), perhaps  
663 suggesting a peak in melt-rock interaction and the replacement or resetting of inherited  
664 monazite driven by large-scale changes to deep crustal architecture and basin dynamics that  
665 initiated at this time. Similarly, the youngest monazite age of *c.* 370 Ma most probably  
666 represents the last recorded stage of overprinting metamorphism and/or monazite resetting,  
667 perhaps due to either (i) the cessation of melt migration in the shear zone; or (ii) shear zone  
668 armouring physically buffering melt interaction with the monazite grains incompletely reset by  
669 coupled dissolution-precipitation processes (Daczko *et al.*, 2016; Varga *et al.*, 2020).

## 671 **5. 2. Microstructural evidence for melt-present deformation**

672           Of the five key microstructures indicative of the former presence of melt in  
673 high-strain zones outlined by Stuart *et al.* (2018b), four were observed in the GDSZ samples:  
674 (1) small dihedral angles between biotite, muscovite, plagioclase, magnetite and quartz (Figs.  
675 3 and 5b, c); (2) elongated grain boundary films pseudomorphed by biotite (Figs. 3 and 5a–e);

676 (3) neighbourhoods of small quartz grains connected in three dimensions (Figs. 4c and 6c, d),  
677 presenting less than ten degrees of crystallographic misorientation between grains; (4)  
678 pseudomorphs of inferred cm-scale granitic melt pockets (Fig. 4b, d). Other microstructures  
679 that support the interpretation of melt-present deformation in the GDSZ include myrmekitic  
680 intergrowth of quartz and plagioclase (Fig. 3b, f and h), biotite finger-like protrusions into  
681 adjacent quartz grains (Fig. 5a–d) and CL images highlighting bands of darker CL response in  
682 quartz near biotite (Fig. 5g–j), possibly reflecting microscale fracturing, melt migration  
683 pathways or a CL signature of quartz grain boundary migration (Holness & Watt, 2001;  
684 Bergman & Piazzolo, 2012).

685 Quartz crystallographic orientation data also supports the former presence of  
686 melt in the GDSZ. Quartz grains in the H-Qtz and M-Qtz samples have a strong CPO, whereas  
687 quartz grains present in sample GL have a weak CPO and apparent activation of multiple slip  
688 systems (Fig. 7). The strong CPO for the highly strained quartzite represented by H-Qtz and  
689 M-Qtz samples is not accompanied by intense recrystallisation of the quartz grains. Rather,  
690 they record widespread grain boundary migration, implying deformation temperatures  $> 500^{\circ}\text{C}$   
691 (Stipp *et al.*, 2002*a, b*). The observed CPO in quartzite is most probably an inherited structure  
692 formed at granulite facies, suggesting that the prism  $\langle a \rangle$  slip system was activated during the  
693 Strangways Event rather than the ASO. This interpretation is informed by the lack of plastic  
694 shear band microstructures in the quartzite samples and quartz grains (Gapais & White, 1982;  
695 Menegon *et al.*, 2011) or quartz grain size reduction by recrystallisation (Hobbs, 1968; Lloyd  
696 & Freeman, 1994; Lloyd, 2004; Stipp *et al.*, 2010) (Figs. 4b, c, 7 and 8). The absence of these  
697 features supports that melt flux pathways initiated within the quartzite mylonite, subsequently  
698 crystallising biotite-sillimanite-muscovite and resulted from shear or dilation fractures in a  
699 brittle regime (Lloyd & Knipe, 1992).

700 Alongside the deformation processes documented above, diffusion or

1  
2  
3  
4  
5  
6  
7  
8  
9  
10  
11  
12  
13  
14  
15  
16  
17  
18  
19  
20  
21  
22  
23  
24  
25  
26  
27  
28  
29  
30  
31  
32  
33  
34  
35  
36  
37  
38  
39  
40  
41  
42  
43  
44  
45  
46  
47  
48  
49  
50  
51  
52  
53  
54  
55  
56  
57  
58  
59  
60  
61  
62  
63  
64  
65

701 dissolution-precipitation creep likely played a role in quartz deformation within the proposed  
702 fluid saturated high-strain zone (Farver & Yund, 2000; Bestmann *et al.*, 2004). However, the  
703 presence of fluid could imply reaction with quartz grains and silica loss to the local open  
704 system, undercutting these creep processes (Farver & Yund, 2000). Small quartz grains in  
705 sample GL (Fig. 7a) have a weak CPO and apparent activation of multiple slip systems (Fig.  
706 7b, c), suggesting that they are not relict grains from the main quartzite present in sample M-  
707 Qtz, but instead are the product of neofomed quartz grains that may reflect melt  
708 pseudomorphs. These results are consistent with the concomitant deformation of quartz grains  
709 in the presence of melt, causing strain to be accommodated into the weaker surrounding melt  
710 and preventing the development of a strong CPO similar to that observed for quartz grains in  
711 samples M- and H-Qtz (Fig. 7; Lee *et al.*, 2018; Stuart *et al.*, 2018b; Prakash *et al.*, 2018).

712           A larger mean quartz grain size is observed in domains of the quartzite samples  
713 close or in contact with the inferred melt pathways (Fig. 8). This may be explained by a local  
714 increase in temperature due to melt flux (Fig. 7a, d), leading to static grain growth and recovery  
715 of quartz grains in samples M-Qtz (close to glimmerite) and H-Qtz (distant from glimmerite).  
716 An enhanced local effect suggests that melt flux was short-lived and probably involved several  
717 pulses, rather than a continuous and long-lived event that would anneal a larger area of the  
718 sample (Heilbronner & Tullis, 2002; Piazzolo *et al.*, 2006). During annealing, grain boundaries  
719 migrate to cross biotite boundaries (e.g., Piazzolo *et al.*, 2006), matching the increase in biotite  
720 enclosure with proximity to the inferred melt pathways (Figs. 6e and 7). Furthermore, subgrain  
721 boundaries are rearranged and decrease in abundance (e.g., Borthwick & Piazzolo, 2010), while  
722 the intensity of CPO simultaneously increases (Piazzolo *et al.*, 2010). The much smaller mean  
723 size of quartz present in sample GL can be related to its neofomation by melt pseudomorphism  
724 as previously described.

725           Taken individually, the microstructures described above are not sufficient

1 726 evidence to argue convincingly for the former presence of quartzo-feldspathic melt in high-  
2 727 strain zones. However, it is the combination and consistency of several key microstructural  
3  
4 728 features that lends weight to our interpretation. It should also be noted that preservation of such,  
5  
6  
7 729 often delicate, microstructures is highly dependent on subsequent metamorphic and tectonic  
8  
9  
10 730 overprinting during the retrograde path, which can potentially obliterate indicators of former  
11  
12 731 melt presence (Holness *et al.*, 2011). This suggests that once the melt had crystallised, the  
13  
14 732 quartzites were rheologically strong, enabling their microstructural features to be preserved.  
15  
16  
17 733

### 18 19 734 **5. 3. Glimmerite geochemistry and links to melt-rock interaction processes**

20  
21  
22 735 Comparing the whole rock major oxide geochemistry of sample GL against the  
23  
24 736 range of precursor rock types present in the SMC is necessary to understand the chemical  
25  
26 737 evolution between the different glimmerite rocks present in the study area and their possible  
27  
28  
29 738 protoliths. This analysis reveals that the glimmerite composition generally plots between the  
30  
31 739 major oxide values for ferromagnesian granulites, schistose high-strain zone metapelites and  
32  
33  
34 740 average peraluminous granitic biotite (Fig. 9). It does not demonstrate a strong relationship  
35  
36 741 between the glimmerite rock observed in the GDSZ and the surrounding rocks from the SMC,  
37  
38  
39 742 suggesting that glimmerite formation involved a high degree of geochemical modification (i.e.,  
40  
41 743 metasomatism *s.l.*). We infer that reactive flow of melt through high-strain zones led to the  
42  
43  
44 744 near-complete dissolution of a SMC protolith, likely one of the quartzo-feldspathic rocks based  
45  
46 745 on the scarcely preserved layers and lenses within the glimmerite outcrop. Coupled  
47  
48  
49 746 precipitation of abundant biotite pushed the whole rock composition of the resulting glimmerite  
50  
51 747 rock to values similar to the average composition of peraluminous granitic biotite (Fig. 9).  
52

53 748 Biotite geochemistry affords more detailed insights into the mechanism of melt-  
54  
55  
56 749 present deformation driving glimmerite formation in the GDSZ. Micas (particularly biotite)  
57  
58 750 dominate both the glimmerite mineral assemblage and the inferred reactive melt pathways  
59  
60  
61  
62  
63  
64  
65

1 751 within the partially modified quartzite samples (Figs. 2d–i, 4–7). Low to moderate F and Cl  
2 752 concentrations (< 1 wt%; Table 1 and Table S1) suggest their formation from a halogen-  
3  
4 753 depleted melt in an open system. This interpretation is based on the recognition of F- and Cl-  
5  
6  
7 754 enriched biotite commonly being formed by halogen-enriched aqueous fluid-rock interaction  
8  
9  
10 755 in high-grade metamorphic rocks where fluid flux was limited (Markl & Bucher, 1998; Markl  
11  
12 756 & Piazzolo, 1998; Aranovich & Safonov, 2018). In these case studies of metamorphic fluids, a  
13  
14 757 correlation between halogen-enriched fluids and halogen-enriched biotite reaction formation  
15  
16  
17 758 could be made.

18  
19 759 The discrimination of biotite formed at supra-solidus versus sub-solidus  
20  
21  
22 760 conditions is not straightforward. Here, the discrimination diagram of Nachit *et al.* (1985) is  
23  
24 761 used, based on the inference of melt-present conditions (Fig. 10b). The diagram is potentially  
25  
26  
27 762 useful to inform on the type of melt involved in the formation of glimmerite. The  
28  
29 763 peraluminosity of the melt is inferred from the aluminium content of the equilibrated  
30  
31  
32 764 crystallised biotite (Nachit *et al.*, 1985; Stussi & Cuney, 1996), and our data suggest that the  
33  
34 765 glimmerite biotite shares similarities with magmatic biotite formed from and partially  
35  
36 766 reequilibrated with peraluminous melt.

37  
38  
39 767 The highly dispersed and overall lower concentrations of Al, Ti, Fe and Mn of  
40  
41 768 biotite in the L-Qtz sample likely reflects variable inheritance from the precursor quartzite over  
42  
43  
44 769 the externally-derived melt, compared to H-Qtz and M-Qtz/GL biotite that are dominated by  
45  
46 770 the chemistry of the melt (i.e., are melt buffered; Fig. 10). About half of the L-Qtz biotite  
47  
48  
49 771 analyses trend towards the formation conditions observed for H-Qtz and M-Qtz/GL biotite,  
50  
51 772 showing an increase in the apparent temperature of formation and peraluminosity of  
52  
53 773 crystallising fluid, concordant with the igneous biotite data compiled by Stussi & Cuney (1996).  
54  
55  
56 774 This wide range of L-Qtz biotite compositions likely records variable but low local melt  
57  
58 775 volumes in the quartzite domains and lower degrees of equilibration with the fluxing melt.  
59  
60  
61  
62  
63  
64  
65

776 The trace element analyses of biotite in all samples shows lower chondrite-  
1  
2 777 normalised concentrations of REE, Zr and Hf, and higher chondrite-normalised concentrations  
3  
4 778 of Nb and Ta (Figs. 11 and 12). The latter likely resulted from the high partition coefficient  
5  
6  
7 779 between biotite and granitic melt. In their experiments and analysis of natural examples,  
8  
9 780 Stepanov & Herman (2013) observed that biotite in partial melting environments preferentially  
10  
11 781 incorporates Nb over Ta, concluding that biotite plays an important role for the missing Nb-  
12  
13 782 paradox observed in the continental crust. Such behaviour of Nb incorporation over Ta in  
14  
15 783 biotite is observed in our data, with most of the L-Qtz biotite grains having lower Nb  
16  
17 784 concentrations and overall lower Nb/Ta ratios when compared to H-Qtz, M-Qtz and GL biotite  
18  
19 785 grains (Figs. 11 and 12).  
20  
21  
22  
23

24 786 Concentrations of Zr and Hf in biotite for all samples are similar, although lower  
25  
26 787 than biotite from the partially melted metapelite enclaves of El Hoyazo (Acosta-Vigil *et al.*,  
27  
28 788 2010), and lower by 2–3 orders of magnitude when compared to rhyodacite biotite (Nash &  
29  
30 789 Crecraft, 1985) (Fig. 11). The broad similarity in Zr and Hf concentrations between GDSZ and  
31  
32 790 El Hoyazo biotites can be explained by the presence of abundant zircon grains in equilibrium  
33  
34 791 with biotite, possibly allowing the zircon grains to buffer Zr and Hf in the melt (Acosta-Vigil  
35  
36 792 *et al.*, 2010; Nash & Crecraft, 1985). Conversely, for rhyodacite biotite it is proposed that Zr  
37  
38 793 and Hf melt buffering did not occur during rhyodacite formation due to the relative timing of  
39  
40 794 zircon crystallisation.  
41  
42  
43  
44  
45

46 795 The GDSZ biotites are characterised by low REE values, with chondrite-  
47  
48 796 normalised concentrations below unity and slightly higher LREE over HREE (Fig. 11a–c).  
49  
50 797 Such low REE concentrations are similar to the biotite REE chemistry of (i) partial melting  
51  
52 798 environments of the El Hoyazo enclave; (ii) migmatite leucosomes of the Peña Negra Complex  
53  
54 799 (Acosta-Vigil *et al.*, 2010; Bea *et al.*, 1994b); and (iii) closed system fractional crystallisation  
55  
56 800 from peraluminous melt of the Pedrobernardo pluton (Bea *et al.*, 1994a) (Fig. 11d). The REE-  
57  
58  
59  
60  
61  
62  
63  
64  
65

1 801 depleted patterns observed for El Hoyazo, Peña Negra and Pedrobernardo biotites (Table S4  
2 802 and Fig. 11d) are consistent with the presence of accessory minerals with higher REE  
3  
4 803 mineral/melt partitioning ratios (i.e., monazite, zircon and apatite), or by REE-depleted melt  
5  
6  
7 804 due to REE retention in residual accessory minerals in the palaeosome (e.g., Prent *et al.*, 2019;  
8  
9 805 Gonçalves *et al.*, 2021). Either of these mechanisms, or a combination of both, can be  
10  
11 806 considered viable explanations for the biotite REE compositions of H-Qtz, M-Qtz and GL  
12  
13 807 samples in our study, due to the presence of monazite and apatite in equilibrium with the  
14  
15 808 glimmerite mineral assemblage, or the externally-derived melt becoming depleted in REE  
16  
17 809 following crystallisation and fractionation of mineral phases rich in REE during prior melt  
18  
19 810 flow.

24 811           Another explanation for the REE-depleted signature of GDSZ biotites may be a  
25  
26 812 smaller equilibration volume and/or variable composition of the fluxing melt, as proposed by  
27  
28 813 Stuart *et al.* (2018a) for variable igneous-like mineral REE patterns measured in metasomatic  
29  
30 814 reactions of the Pembroke Granulite (lower crust of a magmatic arc). Similar to this example,  
31  
32 815 the presence of melt in the GDSZ is implied by the overall enrichment of incompatible elements  
33  
34 816 in biotite from sample L-Qtz to the group of samples H-Qtz, M-Qtz and GL (Fig. 12). The  
35  
36 817 abundance of incompatible elements follows an approximately linear trend with the apparent  
37  
38 818 increase in temperature informed by the increase in biotite Ti concentrations. This pattern can  
39  
40 819 be attributed to a more fractionated melt enriched in incompatible elements (Cerny, 1991;  
41  
42 820 O'Connor *et al.*, 1991; Bea *et al.*, 1994a), or an increasing melt equilibration volume from  
43  
44 821 sample L-Qtz to the most reacted samples, possibly also explaining the apparent temperature  
45  
46 822 difference between sample L-Qtz and sample H-Qtz.

53 823

#### 56 824 **5. 4. Estimates of reactive hydrous melt volume**

825 In the absence of field evidence for upper crustal melt products that would have  
1  
2 826 formed as a consequence of melt flux (i.e., igneous intrusions), we use the modal percentage  
3  
4 827 of hydrous phases in the studied samples to estimate the reactive hydrous melt volume. We  
5  
6  
7 828 consider that the hydrous phases present are a consequence of the time-integrated volume of  
8  
9 829 reactive melt flux (Daczko *et al.*, 2016; Stuart *et al.*, 2018a). Arrested melt flux may occur  
10  
11 830 upon draining of source magma or cooling and freezing of the system. Regardless, the cessation  
12  
13 831 of reactive melt flux formed the microstructures observed in the studied samples, and their  
14  
15 832 patterns suggest that melt migration occurred mainly via intergranular mechanisms and was  
16  
17 833 focused along structurally-controlled planes, such as the main rock foliation and mode 1  
18  
19 834 fractures potentially formed by melt pathway fluid overpressure (Sibson, 1988). In the  
20  
21 835 glimmerite domain, the extreme metasomatism implies higher reactive melt flux, where the  
22  
23 836 protolith is partially dissolved by the reactive melt, enhancing porosity and permeability (e.g.,  
24  
25 837 Daczko *et al.*, 2016) and providing a positive feedback that allows a higher volume of melt  
26  
27 838 flow and consequent increase in the formation of hydrous minerals. In this section, the  
28  
29 839 minimum volume of reactive hydrous melt needed to form glimmerite is estimated for each of  
30  
31 840 the Gough Dam shear zone samples. The observed increase in modal biotite and muscovite of  
32  
33 841 the GDSZ can be related to a melt flow-derived hydrous metasomatism mechanism (following  
34  
35 842 the method of Stuart *et al.*, 2018a). With this interpretation in mind, the calculation of a  
36  
37 843 minimum volume of reactive melt flux can be derived.  
38  
39  
40  
41  
42  
43  
44  
45

844 The minimum volume of reactive melt flux is calculated considering a  
46  
47 845 hypothetical cube of quartzite rock containing no hydrous phases and an H<sub>2</sub>O content close to  
48  
49 846 0%. The proportions and average H<sub>2</sub>O content of the hydrous phases formed during the melt-  
50  
51 847 rock hydrous metasomatism (i.e., biotite and muscovite in this study) are used to calculate the  
52  
53 848 final H<sub>2</sub>O composition of our hypothetical quartzite cube. Calculated H<sub>2</sub>O content for biotite  
54  
55 849 and muscovite from EMP analyses are 3.97 wt% (n = 55) and 4.44 wt% (n = 13), respectively  
56  
57  
58  
59  
60  
61  
62  
63  
64  
65

1 850 (Table 1 and Table S1). Totalling the proportion of biotite and muscovite in each sample gives  
2 851 the final H<sub>2</sub>O content of 0.3 wt% and 0.7 wt% for samples L-Qtz and H-Qtz, respectively  
3  
4 852 (Table 3).  
5

6  
7 853 The reactive melt flux is calculated by using the volume of melt necessary to  
8  
9 854 drive the increase in H<sub>2</sub>O content. Four melts of variable H<sub>2</sub>O content are considered (with 3,  
10  
11 855 6, 9 and 12 wt% H<sub>2</sub>O), which represent a typical range of water content in granitic melts (Holtz  
12  
13 856 *et al.*, 2001). Two simplifying theoretical assumptions are made: (1) the totality of the H<sub>2</sub>O  
14  
15 857 present in the melt is partitioned into the new hydrous phases; and (2) melt flux is homogeneous  
16  
17 858 throughout the rock cube. In nature, this perfect behaviour of H<sub>2</sub>O partitioning and  
18  
19 859 homogeneous flux would not necessarily be expected. The model is also restricted by  
20  
21 860 disregarding some anhydrous phases (plagioclase, sillimanite, K-feldspar) into the H<sub>2</sub>O  
22  
23 861 partition calculation, leading to an underestimation of the amount of melt flux for sample H-  
24  
25 862 Qtz. Further support for an underestimation of melt flux is based on the fact that there is the  
26  
27 863 possibility of armoured and unreactive melt flux following formation of glimmerite layers,  
28  
29 864 analogous to hornblendite channels observed in arc environments (Daczko *et al.*, 2016; Stuart  
30  
31 865 *et al.*, 2018a) or dunite channels observed in mantle rocks (Kelemen *et al.*, 1995). Calculated  
32  
33 866 minimum melt flux volumes range between 0.03 to 0.23 m<sup>3</sup> of melt per m<sup>3</sup> of rock (Table 3).  
34  
35 867 Values of melt flux volume vary according to the interplay of the initial H<sub>2</sub>O present in the  
36  
37 868 fluxing melt and the proportion of reactive hydrous phases observed in the samples. Sample L-  
38  
39 869 Qtz shows the lowest values of melt flux (0.03–0.12 m<sup>3</sup>), with H-Qtz approximately doubling  
40  
41 870 the L-Qtz melt flux values (0.06–0.23 m<sup>3</sup>). Unfortunately, upper crustal rocks that may contain  
42  
43 871 the crystallised products of the unreacted flowing melt are not preserved in the GDSZ (Fig. 1).  
44  
45 872 Attempting a volume estimation of the igneous bodies formed from the channelised melt  
46  
47 873 flowing through the armoured shear zone is thus not possible, making the obtained values of  
48  
49 874 melt flux the absolute minimum necessary for the observed glimmerite hydration reactions.  
50  
51  
52  
53  
54  
55  
56  
57  
58  
59  
60  
61  
62  
63  
64  
65

875

## 5.5. Model for glimmerite schist belt formation and its geotectonic significance

Our proposed model for glimmerite schist belt formation is summarised in Fig. 15. It evolves from an initial stage of melt influx advancing upward within the GDSZ along pre-existing anisotropies within the original rock packages (Fig. 15a), to a final stage of high-strain zone metasomatism resulting in glimmerite formation as a consequence of hydrous peraluminous melt interaction with adjacent anhydrous rocks (Fig. 15b, c). During the initial stage, channelised melt flow within the high-strain zone causes strength contrasts between rock packages that drive the formation of orthogonal extensional fractures, further increasing the surface area for melt-rock interaction and promoting the formation of glimmerite (Fig. 15c). The growth of extensional fractures towards the centre of the high-strain zone allows for the creation of additional interconnected melt pathways, enhancing the glimmerite formation process in the high-strain zone and increasing the size of granite lenses and sheets towards the centre of the shear zone (Fig. 15b).

The interpreted evolution of the GDSZ is distinct to the seminal examples of glimmerite formation driven by metasomatism of mantle rocks (Becker *et al.*, 1999; Grégoire *et al.*, 2002; Rajesh *et al.*, 2004). The “classic” glimmerite rocks generally show a spatial relationship in outcrop between mantle rocks and either a K-rich metasome with or without a third component involving felsic igneous intrusions (Fyfe & McBirney, 1975; Wyllie & Sekine, 1982; Rakotondrazafy *et al.*, 1997; Fuertes-Fuente *et al.*, 2000). The K-rich mantle metasomes are characterised by an assemblage composed usually of biotite + amphibole ± pyroxene (Menzies & Murthy, 1980; Smart *et al.*, 2019). These characteristics of “classic” glimmerites are not observed in sample GL. However, similarities between our proposed mode of glimmerite formation and the classic examples include melt-rock interaction involving a felsic melt, and modification of a protolithic rock (felsic versus ultramafic) by melt-mediated

1 900 coupled dissolution-precipitation, forming abundant biotite (Figs. 4–7). Genetically and  
2 901 mineralogically, sample GL shows a higher degree of similarity to the formation of “back  
3  
4 902 reactive melanosome” in anatectic migmatites described by Kriegsman (2001). In that model,  
5  
6 903 locally-derived in-situ melt is argued to interact with the mesosome. This diverges from our  
7  
8 904 proposed mode of protolith (quartzite) modification and glimmerite formation, where we  
9  
10 905 invoke an externally-sourced melt to drive dissolution of protolith minerals and precipitation  
11  
12 906 of glimmerite minerals, mainly quartz and biotite, respectively.  
13  
14  
15

16  
17 907           We now put our model of melt migration and deformation within GDSZ into  
18  
19 908 the context of crustal evolution. A key feature of the Earth’s crust is its layered character mainly  
20  
21 909 based on chemical composition, with the upper crust having a higher silicic bulk composition  
22  
23 910 and concentration of granitic material compared with the more ferromagnesian bulk  
24  
25 911 composition of the lower crust (Vigneresse, 1995; Brown & Rushmer, 2006). Deeply seated  
26  
27 912 high-strain zones in the lower to middle crust are considered part of the crustal system for melt  
28  
29 913 migration (Brown & Solar, 1998; Daczko *et al.*, 2016). Zones of dominantly flattening strain  
30  
31 914 function as major pathways for the ascent of melt originating from anatectic processes in the  
32  
33 915 lower to middle crust and are partially responsible for batch mass transfer of melt to the upper  
34  
35 916 crust (Hutton, 1988; Brown & Solar, 1999; Sawyer *et al.*, 2011; Daczko *et al.*, 2016; Etheridge  
36  
37 917 *et al.*, 2020), as exemplified by the proposed transfer of melt throughout high-strain zones in  
38  
39 918 our model of glimmerite schist belt formation (Fig. 15).  
40  
41  
42  
43  
44  
45

46 919           In the dehydrated middle to lower crust, the influx of locally- or externally-  
47  
48 920 derived fluids forms pronounced local chemical gradients between fluid and rock, which when  
49  
50 921 paired with high differential stresses, enhances metamorphic reactions (Putnis & Austrheim,  
51  
52 922 2010; Wheeler, 2014; Stuart *et al.*, 2016, 2017). If the fluid has high enough water fugacity,  
53  
54 923 exothermic hydration (or retrograde) metamorphic reactions of anhydrous minerals will occur.  
55  
56 924 The intracontinental Alice Springs Orogeny, involving the GDSZ in particular and possibly  
57  
58  
59  
60  
61  
62  
63  
64  
65

1 925 other equivalent shear zones in central Australia, are good examples of melt flow pathways in  
2 926 high-strain zones that lead to melt-rock interaction and hydration of protolith granulites. This  
3  
4 927 process is proposed as the source of peraluminous melt that initially fluxed through pre-existing  
5  
6  
7 928 rock anisotropies leading to the formation of glimmerite schist belts (Fig. 15).

8  
9 929 The physical presence of melt and metamorphic reactions that produce  
10  
11 930 rheologically weak minerals in high-strain zones (i.e., reaction softening) favour a decrease in  
12  
13 931 the strength of the affected rocks. This increases the accommodation of strain transmitted from  
14  
15 932 the surrounding and more competent host rocks, and facilitates strain localisation to enhance  
16  
17 933 the displacement across the high-strain zone (Hollister & Crawford, 1986; Brown & Solar,  
18  
19 934 1998; Molnar & Dayem, 2010; Cunningham, 2013; Piazzolo *et al.*, 2020). Reaction softening  
20  
21 935 such as that presented in this study, characterised by the formation of layers with high  
22  
23 936 proportions of phyllosilicates within a competent anhydrous granulite terrane (Figs. 2 and 15),  
24  
25 937 can be considered a textbook example of decreased rock strength, enabling deformation  
26  
27 938 accommodation and consequent strain localisation within structures such as the GDSZ.  
28  
29 939 However, we do not observe classic solid-state deformation microstructures in any of our  
30  
31 940 samples, suggesting that either (1) melt was involved in any/all reactivation events, forming  
32  
33 941 microstructures indicative of the former presence of melt each time; or (2) differential stresses  
34  
35 942 at the continental interior were never high enough to reactivate reaction softened high-strain  
36  
37 943 zones.

38  
39 944 Weakening of deforming rocks is proposed by various authors as an important  
40  
41 945 mechanism to enhance orogenesis, especially true for far-field contractional intracontinental  
42  
43 946 orogenies (e.g., Alice Springs and Altai orogenies; Hand & Sandiford, 1999; Raimondo *et al.*,  
44  
45 947 2014; Cunningham, 2005; Silva *et al.*, 2018; Piazzolo *et al.*, 2020), where differential stresses  
46  
47 948 are comparatively lower compared to those observed in areas proximal to collisional plate  
48  
49 949 boundaries (Coblentz *et al.*, 1998; Heidbach *et al.*, 2010). Moreover, weakened rocks are  
50  
51  
52  
53  
54  
55  
56  
57  
58  
59  
60  
61  
62  
63  
64  
65

1 950 described by various authors to be significant in the multiple reactivation events documented  
2 951 for the ASO (Raimondo *et al.*, 2014; Silva *et al.*, 2018; Piazzolo *et al.*, 2020), because they  
3  
4 952 facilitate the accommodation of lithospheric horizontal stresses during increased early  
5  
6  
7 953 Palaeozoic dextral rotation of the northern Australian block (Roberts & Houseman, 2001; Silva  
8  
9  
10 954 *et al.*, 2018). The formation and presence of meter-scale glimmerites, such as we document  
11  
12 955 here in the GDSZ and characterise hydrated high-strain zones elsewhere in the SMC (Fig. 1),  
13  
14 956 indicates that this specific rock type, characterised by its intrinsic low competence and  
15  
16  
17 957 enhanced by the physical presence of melt, was an ideal candidate to intensify intracontinental  
18  
19 958 orogenesis in central Australia.  
20

21  
22 959

## 23 24 960 **6. CONCLUSIONS**

25  
26 961 Glimmerite schists in the study area of the Gough Dam shear zone (GDSZ)  
27  
28  
29 962 formed during the Palaeozoic Alice Springs Orogeny (ASO) by the migration of a hydrous  
30  
31 963 peraluminous melt and its interaction with granulite protoliths of quartzo-feldspathic  
32  
33  
34 964 composition. In addition to melt migration through high-strain rocks, fractures parallel and  
35  
36 965 perpendicular to the shear zone foliation created melt pathways that enhanced melt infiltration  
37  
38  
39 966 into the protolith. High-temperature melt-rock interaction at conditions close to the melt  
40  
41 967 liquidus promoted dissolution of the protolith and precipitation of abundant biotite. Localised  
42  
43  
44 968 temperature-dependent quartz grain growth recovery is observed in highly organised modified  
45  
46 969 quartzite mylonite, whereas a random quartz grain orientation is observed in glimmerite. The  
47  
48  
49 970 mode of hydrous minerals in the various rock types is inferred to relate to variable time-  
50  
51 971 integrated volumes of reactive melt flux. Zones of higher time-integrated melt flux through the  
52  
53 972 shear zone show increased equilibration and homogenisation of the neoformed hydrous  
54  
55  
56 973 minerals. For example, a calculated melt flux between 0.06–0.23 m<sup>3</sup> per m<sup>3</sup> of rock allowed an  
57  
58 974 increase in hydrous minerals within the host rock of 8–17 vol%, concomitantly increasing the  
59  
60  
61  
62  
63  
64  
65

1 975 concentration of trace elements (Ti, Nb, Zr, Hf, Sc, Ba and Li) and REE (mostly Eu). Inherited  
2 976 monazite with ages aligned with the *c.* 1735–1690 Ma Strangways Event is variably reset to  
3  
4 977 early-ASO ages (*c.* 450 Ma) by coupled dissolution-precipitation processes, indicating that the  
5  
6  
7 978 mobility of Pb was low and leading to high dispersion in the age population. The formation of  
8  
9 979 glimmerite schist in anhydrous terranes may be an important mechanism for stress localisation  
10  
11 980 and by consequence strain localisation, facilitating orogenesis in intracontinental regions as we  
12  
13  
14 981 propose for the ASO.  
15  
16

17 982

### 18 19 983 **ACKNOWLEDGMENTS**

20  
21 984 We thank the landowners for permission to access sample localities in the Gough Dam shear  
22  
23  
24 985 zone, central Australia. M. Bebbington, T. Murphy and Y-J. Lai (Macquarie University)  
25  
26 986 assisted with making thin sections and geochemical analysis. Sandrin Feig (University of  
27  
28  
29 987 Tasmania) assisted with electron microprobe analysis. Duncan Hedges and Richard Walshaw  
30  
31 988 (University of Leeds) assisted with EBSD data collection and cathodoluminescence imagery,  
32  
33  
34 989 and Hadrien Henry (University of Toulouse) with MTEX assistance. This work was carried  
35  
36 990 out as part of a PhD study at Macquarie University and was supported by ARC Discovery grant  
37  
38  
39 991 DP160103449 to A. Putnis, T. Raimondo and N. Daczko. We thank Amicia Lee (University of  
40  
41 992 Tromsø) for a constructive review and comments, and Sebastian Tappe (University of  
42  
43  
44 993 Johannesburg) for editorial handling. We thank S. Cruden (Monash University), A. Tommasi  
45  
46 994 (University of Montpellier) and G. Solar (Buffalo State University) for feedback on an earlier  
47  
48  
49 995 version of this manuscript. This study used instrumentation funded by ARC LIEF, DEST  
50  
51 996 Systemic Infrastructure Grants, NCRIS/AuScope, industry partners and Macquarie University.  
52  
53 997 This is contribution 1659 from the ARC Centre of Excellence for Core to Crust Fluid Systems  
54  
55  
56 998 (<http://www.CCFS.mq.edu.au>).  
57

58 999

59  
60  
61  
62  
63  
64  
65

1000 **SUPPLEMENTARY MATERIAL**

1  
2 1001 Supplementary materials are available at Gondwana Research online.  
3

4  
5 1002

6  
7 1003 **REFERENCES**  
8  
9

10 1004 Acosta-Vigil, A., Buick, I., Hermann, J., Cesare, B., Rubatto, D., London, D., Morgan, G.B.,  
11  
12 1005 2010. Mechanisms of crustal anatexis: a geochemical study of partially melted  
13  
14 1006 metapelitic enclaves and host dacite, SE Spain. *J. Petrol.* 51, 785–821.  
15

16  
17 1007 Aranovich, L., Safonov, O., 2018. Halogens in high-grade metamorphism. In: Harlov, D.E.,  
18  
19 1008 Aranovich, L. (eds.), *The Role of Halogens in Terrestrial and Extraterrestrial*  
20  
21 1009 *Geochemical Processes*. Springer International Publ., Switzerland, 713–757.  
22

23 1010 Armstrong, J.T., 1988. Quantitative analysis of silicate and oxide materials: Comparison of  
24  
25 1011 Monte Carlo, ZAF, and  $\psi$  ( $\rho z$ ) procedures. *Microb. Anal.*, 239–246.  
26

27  
28 1012 Bachmann, F., Hielscher, R., Schaeben, H., 2010. Texture analysis with MTEX – free and open  
29  
30 1013 source software toolbox. *Solid State Phenom.* 160, 63–68.  
31  
32

33 1014 Ballèvre, M., Hensen, B.J., Reynard, B., 1997. Orthopyroxene-andalusite symplectites  
34  
35 1015 replacing cordierite in granulites from the Strangways Range (Arunta block, central  
36  
37 1016 Australia): a new twist to the pressure-temperature history. *Geology* 25, 215–218.  
38  
39

40 1017 Ballèvre, M., Möller, A., Hensen, B.J., 2000. Exhumation of the lower crust during crustal  
41  
42 1018 shortening: an Alice Springs (380 Ma) age for a prograde amphibolite facies shear zone  
43  
44 1019 in the Strangways Metamorphic Complex (central Australia). *J. Metamorph. Geol.* 18,  
45  
46 1020 737–747.  
47

48  
49 1021 Bea, F., Pereira, M.D., Corretgé, L.G., Fershtater, G.B., 1994a. Differentiation of strongly  
50  
51 1022 peraluminous, perphosphorus granites: the Pedrobernardo pluton, central  
52  
53 1023 Spain. *Geochim. Cosmochim. Acta* 58, 2609–2627.  
54

55 1024 Bea, F., Pereira, M.D., Stroh, A., 1994b. Mineral/leucosome trace-element partitioning in a  
56  
57 1025 peraluminous migmatite (a laser ablation-ICP-MS study). *Chem. Geol.* 117, 291–312.  
58  
59  
60  
61  
62  
63  
64  
65

- 1026 Beard, J.S., Ragland, P.C., Rushmer, T., 2004. Hydration crystallization reactions between  
1  
2 1027 anhydrous minerals and hydrous melt to yield amphibole and biotite in igneous rocks:  
3  
4 1028 Description and implications. *J. Geol.* 112, 617–621.  
5
- 6  
7 1029 Beaumont, C., Jamieson, R.A., Nguyen, M.H., Lee, B., 2001. Himalayan tectonics explained  
8  
9 1030 by extrusion of a low-viscosity crustal channel coupled to focused surface denudation.  
10 1031 *Nature* 414, 738–742.  
11  
12
- 13 1032 Becker, H., Wenzel, T., Volker, F., 1999. Geochemistry of glimmerite veins in peridotites from  
14  
15 1033 Lower Austria—implications for the origin of K-rich magmas in collision zones. *J.*  
16  
17 1034 *Petrol.* 40, 315–338.  
18  
19
- 20 1035 Bendall, B., 2000. Mid-Palaeozoic shear zones in the Strangways Range: a record of  
21  
22 1036 intracratonic tectonism in the Arunta Inlier, Central Australia (Doctoral dissertation).  
23  
24 1037 University of Adelaide, Adelaide, Australia.  
25
- 26  
27 1038 Bercovici, D., 1998. Generation of plate tectonics from lithosphere–mantle flow and void–  
28  
29 1039 volatile self-lubrication. *Earth Planet. Sci. Lett.* 154, 139–151.  
30
- 31  
32 1040 Bergman, H., Piazzolo, S., 2012. The recognition of multiple magmatic events and pre-existing  
33  
34 1041 deformation zones in metamorphic rocks as illustrated by CL signatures and numerical  
35 1042 modelling: Examples from the Ballachulish contact aureole, Scotland. *Int. J. Earth*  
36  
37 1043 *Sci.* 101, 1127–1148.  
38  
39
- 40 1044 Bestmann, M., Prior, D.J., Veltkamp, K.T., 2004. Development of single-crystal  $\sigma$ -shaped  
41  
42 1045 quartz porphyroclasts by dissolution–precipitation creep in a calcite marble shear  
43  
44 1046 zone. *J. Struct. Geol.* 26, 869–883.  
45
- 46  
47 1047 Borthwick, V.E., Piazzolo, S., 2010. Post-deformational annealing at the subgrain scale:  
48  
49 1048 Temperature dependent behaviour revealed by in-situ heating experiments on deformed  
50  
51 1049 single crystal halite. *J. Struct. Geol.* 32, 982–996.  
52
- 53  
54 1050 Brodie, K.H., Rutter E.H., 1985. On the relationship between deformation and metamorphism,  
55 1051 with special reference to the behaviour of basic rocks. In: Thompson, A.B., Rubie, D.C.  
56  
57 1052 (eds.), *Advances in Physics and Geochemistry. Metamorphic Reactions – Kinetics,*  
58  
59 1053 *Textures and Deformation 4*, Springer-Verlag, 138–179.  
60  
61  
62  
63  
64  
65

- 1054 Brown, M., Rushmer, T., 2006. Evolution and Differentiation of the Continental Crust.  
1  
2 1055 Cambridge University Press, Cambridge, UK, 553 p.  
3  
4  
5 1056 Brown, M., Solar, G.S., 1998. Shear-zone systems and melts: Feedback relations and self-  
6  
7 1057 organization in orogenic belts. *J. Struct. Geol.* 20, 211–227.  
8  
9  
10 1058 Brown, M., Solar, G.S., 1999. The mechanism of ascent and emplacement of granite magma  
11  
12 1059 during transpression: a syntectonic granite paradigm. *Tectonophysics* 312, 1–33.  
13  
14  
15 1060 Bunge, H.J., 2013. *Texture Analysis in Materials Science: Mathematical Methods*. Elsevier,  
16  
17 1061 Amsterdam, Netherlands.  
18  
19  
20 1062 Cartwright, I., Buick, I.S., 1999. Meteoric fluid flow within Alice Springs age shear zones,  
21  
22 1063 Reynolds Range, central Australia. *J. Metamorph. Geol.* 17, 397–414.  
23  
24  
25 1064 Cartwright, I., Barnicoat, A.C., 2003. Geochemical and stable isotope resetting in shear zones  
26  
27 1065 from Täschalp: Constraints on fluid flow during exhumation in the Western Alps. *J.*  
28  
29 1066 *Metamorph. Geol.* 21, 143–161.  
30  
31  
32 1067 Cartwright, I., Buick, I.S., Foster, D.A., Lambert, D.D., 1999. Alice Springs age shear zones  
33  
34 1068 from the southeastern Reynolds Range, central Australia. *Aust. J. Earth Sci.* 46, 355–  
35  
36 1069 363.  
37  
38  
39 1070 Cerny, P., 1991. Fertile granites of Precambrian rare-element pegmatite fields: is geochemistry  
40  
41 1071 controlled by tectonic setting or source lithologies? *Precambrian Res.* 51, 429–468.  
42  
43  
44 1072 Cesare, B., Acosta-Vigil, A., Bartoli, O., Ferrero, S., 2015. What can we learn from melt  
45  
46 1073 inclusions in migmatites and granulites? *Lithos* 239, 186–216.  
47  
48  
49 1074 Cesare, B., Mariani, E.S., Venturelli, G., 1997. Crustal anatexis and melt extraction during  
50  
51 1075 deformation in the restitic xenoliths at El Joyazo (SE Spain). *Mineral. Mag.* 61, 15–27.  
52  
53  
54 1076 Cesare, B., Satish-Kumar, M., Cruciani, G., Pocker, S., Nodari, L., 2008. Mineral chemistry of  
55  
56 1077 Ti-rich biotite from pegmatite and metapelitic granulites of the Kerala Khondalite Belt  
57  
58 1078 (southeast India): Petrology and further insight into titanium substitutions. *Am.*  
59  
60 1079 *Mineral.* 93, 327–338.  
61  
62  
63  
64  
65

- 1080 Chapman, T., Clarke, G.L., Piazzolo, S., Robbins, V.A., Trimby, P.W., 2019. Grain-scale  
1 dependency of metamorphic reaction on crystal plastic strain. *J. Metamorph. Geol.* 37,  
2 1081 1021–1036.  
3  
4 1082  
5
- 6 1083 Claoué-Long, J., Maidment, D., Hussey, K., Huston, D., 2008. The duration of the Strangways  
7 1084 Event in central Australia: Evidence for prolonged deep crust processes. *Precambrian*  
8 1085 *Res.* 166, 246–262.  
9  
10  
11  
12
- 13 1086 Clarke, G.L., Daczko, N.R., Klepeis, K.A., Rushmer, T., 2005. Roles for fluid and/or melt  
14 1087 advection in forming high- P mafic migmatites, Fiordland, New Zealand. *J.*  
15 1088 *Metamorph. Geol.* 23, 557–567.  
16  
17  
18  
19
- 20 1089 Coblenz, D.D., Zhou, S., Hillis, R.R., Richardson, R.M., Sandiford, M., 1998. Topography,  
21 1090 boundary forces, and the Indo-Australian intraplate stress field. *J. Geophys. Res. Solid*  
22 1091 *Earth* 103, 919–931.  
23  
24  
25
- 26 1092 Collins, W.J., Sawyer, E.W., 1996. Pervasive granitoid magma transfer through the lower-  
27 1093 middle crust during non-coaxial compressional deformation. *J. Metamorph. Geol.* 14,  
28 1094 565–579.  
29  
30  
31  
32
- 33 1095 Collins, W., Shaw, R., 1995. Geochronological constraints on orogenic events in the Arunta  
34 1096 inlier: a review. *Precambrian Res.* 71, 315–346.  
35  
36  
37
- 38 1097 Collins, W., Teyssier, C., 1989. Crustal scale ductile fault systems in the Arunta inlier, central  
39 1098 Australia. *Tectonophysics* 158, 49–66.  
40  
41  
42
- 43 1099 Cunningham, D., 2005. Active intracontinental transpressional mountain building in the  
44 1100 mongolian Altai: Defining a new class of orogen. *Earth Planet. Sci. Lett.* 240, 436–444.  
45  
46  
47
- 48 1101 Cunningham, D., 2013. Mountain building processes in intracontinental oblique deformation  
49 1102 belts: Lessons from the Gobi Corridor, Central Asia. *J. Struct. Geol.* 46, 255–282.  
50  
51  
52
- 53 1103 D'lemos, R.S., Brown, M., Strachan, R.A., 1992. Granite magma generation, ascent and  
54 1104 emplacement within a transpressional orogen. *J. Geol. Soc. London* 149, 487–490.  
55  
56  
57
- 58 1105 Daczko, N.R., Piazzolo, S., Meek, U., Stuart, C.A., Elliott, V., 2016. Hornblendite delineates  
59 1106 zones of mass transfer through the lower crust. *Sci. Rep.* 6, 31369.  
60  
61  
62  
63  
64  
65

- 1107 Elliott, H.A.L., Wall, F., Chakhmouradian, A.R., Siegfried, P.R., Dahlgren, S., Weatherley, S.,  
1  
2 1108 Finch, A.A., Marks, M.A.W., Dowman, E., Deady, E., 2018. Fenites associated with  
3  
4 1109 carbonatite complexes: a review. *Ore Geol. Rev.* 93, 38–59.  
5  
6  
7 1110 Etheridge, M.A., Daczko, N.R., Chapman, T., Stuart, C.A., 2020. Mechanisms of melt  
8  
9 1111 extraction during lower crustal partial melting. *J. Metamorph. Geol.* 39, 57–75.  
10  
11  
12 1112 Etheridge, M.A., Wall, V.J., Vernon, R.H., 1983. The role of the fluid phase during regional  
13  
14 1113 metamorphism and deformation. *J. Metamorph. Geol.* 1, 205–226.  
15  
16  
17 1114 Farver, J., Yund, R., 2000. Silicon diffusion in a natural quartz aggregate: Constraints on  
18  
19 1115 solution-transfer diffusion creep. *Tectonophysics* 325, 193–205.  
20  
21  
22 1116 Faulkner, D.R., Rutter, E.H., 2001. Can the maintenance of overpressured fluids in large strike-  
23  
24 1117 slip fault zones explain their apparent weakness? *Geology* 29, 503–506.  
25  
26  
27 1118 Ferry, J.M., 1994. A historical review of metamorphic fluid flow. *J. Geophys. Res. Solid Earth*  
28  
29 1119 99, 15487–15498.  
30  
31  
32 1120 Fournier, H.W., Camacho, A., Lee, J.K.W., 2016. High-strain deformation and fluid infiltration  
33  
34 1121 diachronism of the middle crust: New Devonian–Permian Alice Springs ages (365–290  
35  
36 1122 Ma) of shear zones in the Strangways Metamorphic Complex, Central Australia. *Chem.*  
37  
38 1123 *Geol.* 443, 39–53.  
39  
40  
41 1124 Frost, B.R., Frost, C.D., 2013. *Essentials of Igneous and Metamorphic Petrology*, 1 edition.  
42  
43 1125 Cambridge University Press, New York.  
44  
45  
46 1126 Fuertes-Fuente, M., Martin-Izard, A., Boiron, M.C., Viñuela, J.M., 2000. P–T path and fluid  
47  
48 1127 evolution in the Franqueira granitic pegmatite, central Galicia, northwestern Spain.  
49  
50 1128 *Can. Mineral.* 38, 1163–1175.  
51  
52  
53 1129 Fyfe, W.S., McBirney, A.R., 1975. Subduction and the structure of andesitic volcanic  
54  
55 1130 belts. *Am. J. Sci.* 275, 285–297.  
56  
57  
58 1131 Gapais, D., White, S.H., 1982. Ductile shear bands in a naturally deformed quartzite. *Textures*  
59  
60 1132 *and Microstructures* 5, 1–17.  
61  
62  
63  
64  
65

- 1133 Ghatak, H., 2017. Distinguishing hydration in shear zones by aqueous fluid versus silicate melt  
1134 (Masters dissertation). Macquarie University, Sydney, Australia.
- 1135 Girard, J., Chen, J., Raterron, P., Holyoke III, C.W., 2013. Hydrolytic weakening of olivine at  
1136 mantle pressure: Evidence of [1 0 0] (0 1 0) slip system softening from single-crystal  
1137 deformation experiments. *Phys. Earth Planet. Inter.* 216, 12–20.
- 1138 Gonçalves, P., Olliot, E., Marquer, D., Connolly, J.A.D., 2012. Role of chemical processes on  
1139 shear zone formation: an example from the Grimsel metagranodiorite (Aar massif,  
1140 Central Alps). *J. Metamorph. Geol.* 30, 703–722.
- 1141 Goncalves, P., Raimondo, T., Paquette, J.-L., Santos de Souza de Oliveira, J., 2021. Garnet as  
1142 a monitor for melt–rock interaction: Textural, mineralogical, and compositional  
1143 evidence of partial melting and melt-driven metasomatism. *J. Metamorph. Geol.* 39,  
1144 617–648.
- 1145 Grand’Homme, A., Janots, E., Seydoux-Guillaume, A.M., Guillaume, D., Magnin, V.,  
1146 Hövelmann, J., Höschen, C., Boiron, M.C., 2018. Mass transport and fractionation  
1147 during monazite alteration by anisotropic replacement. *Chem. Geol.* 484, 51–68.
- 1148 Grand’Homme, A., Janots, E., Seydoux-Guillaume, A.M., Guillaume, D., Bosse, V., Magnin,  
1149 V., 2016. Partial resetting of the U-Th-Pb systems in experimentally altered monazite:  
1150 Nanoscale evidence of incomplete replacement. *Geology* 44, 431–434.
- 1151 Grégoire, M., Bell, D., Le Roex, A., 2002. Trace element geochemistry of phlogopite-rich  
1152 mafic mantle xenoliths: their classification and their relationship to phlogopite-bearing  
1153 peridotites and kimberlites revisited. *Contrib. Mineral. Petrol.* 142, 603–625.
- 1154 Griffin, W.L., 2008. GLITTER: data reduction software for laser ablation ICP-MS. *Laser  
1155 Ablation ICP-MS in the Earth Sciences: Current practices and outstanding issues*, 308–  
1156 311.
- 1157 Griggs, D.T., Blacic, J.D., 1965. Quartz: anomalous weakness of synthetic crystals. *Science*  
1158 147, 292–295.

- 1159 Hand, M., Sandiford, M., 1999. Intraplate deformation in central Australia, the link between  
1 1160 subsidence and fault reactivation. *Tectonophysics* 305, 121–140.  
2  
3  
4  
5 1161 Handy, M.R., Mulch, A., Rosenau, M., Rosenberg, C.L., 2001. The role of fault zones and  
6 1162 melts as agents of weakening, hardening and differentiation of the continental crust: a  
7  
8 1163 synthesis. *Geol. Soc. Spec. Publ.* 186, 305–332.  
9  
10  
11 1164 Hasalová, P., Stipska, P., Powell, R., Schulmann, K., Janousek, V., Lexa, O., 1998.  
12  
13 1165 Transforming mylonitic metagranite by open-system interactions during melt flow. *J.*  
14  
15 1166 *Metamorph. Geol.* 26, 55–80.  
16  
17  
18 1167 Heidbach, O., Tingay, M., Barth, A., Reinecker, J., Kurfess, D., Müller, B., 2010. Global crustal  
19  
20 1168 stress pattern based on the World Stress Map database release 2008. *Tectonophysics*  
21  
22 1169 482, 3–15.  
23  
24  
25 1170 Heilbronner, R., Tullis, J., 2002. The effect of static annealing on microstructures,  
26  
27 1171 crystallographic preferred orientations of quartzites experimentally deformed in axial  
28  
29 1172 compression and shear. *Geol. Soc. Spec. Publ.* 200, 191–218.  
30  
31 1173 Heinrich, K.F.J., 1966. X-ray absorption uncertainty. *The electron microprobe*, 296.  
32  
33 1174 Henke, B.L., 1985. Lawrence Berkeley Laboratories, unpublished.  
34  
35  
36 1175 Henry, D., Guidotti, C.V., Thomson, J.A., 2005. The Ti-saturation surface for low-to-medium  
37  
38 1176 pressure metapelitic biotites: Implications for geothermometry and Ti-substitution  
39  
40 1177 mechanisms. *Am. Mineral.* 90, 316–328.  
41  
42  
43 1178 Henry, H., 2018. *Mantle Pyroxenites: Deformation and Seismic Properties*. (Doctoral  
44  
45 1179 dissertation). Macquarie University, Sydney, Australia.  
46  
47  
48 1180 Henry, H., Tilhac, R., Griffin, W.L., O'Reilly, S.Y., Satsukawa, T., Kaczmarek, M.A.,  
49  
50 1181 Ceuleneer, G., 2017. Deformation of mantle pyroxenites provides clues to geodynamic  
51  
52 1182 processes in subduction zones: case study of the Cabo Ortegal Complex, Spain. *Earth*  
53  
54 1183 *Planet. Sci. Lett.* 472, 174–185.  
55  
56 1184 Hobbs, B.E., 1968. Recrystallization of single crystals of quartz: *Tectonophysics* 6, 353–401.  
57  
58  
59  
60  
61  
62  
63  
64  
65

- 1185 Hollister, L.S., Crawford, M.L., 1986. Melt-enhanced deformation: a major tectonic process.  
1  
2 1186 Geology 14, 558–561.  
3
- 4  
5 1187 Holness, M.B., Watt, G.R., 2001. Quartz recrystallization and fluid flow during contact  
6  
7 1188 metamorphism: a cathodoluminescence study. *Geofluids* 1, 215–228.  
8
- 9  
10 1189 Holness, M.B., Cesare, B., Sawyer, E.W., 2011. Melted rocks under the microscope:  
11  
12 1190 microstructures and their interpretation. *Elements* 7, 247–252.  
13
- 14  
15 1191 Holtz, F., Johannes, W., Tamic, N., Behrens, H., 2001. Maximum and minimum water contents  
16  
17 1192 of granitic melts generated in the crust: a reevaluation and implications. *Lithos* 56, 1–  
18 1193 14.  
19
- 20  
21 1194 Howlett, D., Hand, M., Raimondo, T., Bendall, B., 2014. Episodic mid-crustal metamorphism  
22  
23 1195 during the Alice Springs Orogeny: the Strangways Range, central Australia. In: SGTSG  
24  
25 1196 in the Snowies: Biennial Conference of the Specialist Group for Tectonics and  
26  
27 1197 Structural Geology 2014. Abstracts 109. Geological Society of Australia, 48.  
28
- 29  
30 1198 Hulsbosch, N., Hertogen, J., Dewaele, S., André, L., Muchez, P., 2014. Alkali metal and rare  
31  
32 1199 earth element evolution of rock-forming minerals from the Gatumba area pegmatites  
33  
34 1200 (Rwanda): Quantitative assessment of crystal-melt fractionation in the regional  
35 1201 zonation of pegmatite groups. *Geochim. Cosmochim. Acta* 132, 349–374.  
36
- 37  
38 1202 Hutton, D.H., 1988. Granite emplacement mechanisms and tectonic controls: Inferences from  
39  
40 1203 deformation studies. *Earth Environ. Sci. Trans. R. Soc. Edinb.* 79, 245–255.  
41
- 42  
43 1204 Iyer, S.S., 1974. Granulites and associated schists from the northern Strangways Range, central  
44  
45 1205 Australia: Geochemical and isotopic studies. (Doctoral dissertation), University of  
46  
47 1206 Queensland, Australia.  
48
- 49  
50 1207 Jamieson, R.A., Unsworth, M.J., Harris, N.B., Rosenberg, C.L. Schulmann, K., 2011. Crustal  
51  
52 1208 melting and the flow of mountains. *Elements* 7, 253–260.  
53
- 54 1209 Jarosewich, E., Nelen, J.A., Norberg, J.A., 1980. Reference samples for electron microprobe  
55  
56 1210 analysis. *Geostand. Newslett.* 4, 43–47.  
57
- 58  
59  
60  
61  
62  
63  
64  
65

- 1211 Karato, S.I., 1986. Does partial melting reduce the creep strength of the upper mantle? *Nature*  
1 319, 309–310.  
2  
3  
4  
5 1213 Kelemen, P.B., Shimizu, N. Salters, V.J.M., 1995. Extraction of mid-ocean-ridge basalt from  
6 the upwelling mantle by focused flow of melt in dunite channels. *Nature* 375, 747–753.  
7  
8  
9  
10 1215 Kriegsman, L.M., 2001. Partial melting, partial melt extraction and partial back reaction in  
11 anatexitic migmatites. *Lithos* 56, 75–96.  
12  
13  
14  
15 1217 Kronenberg, A.K., Segall, P., Wolf, G.H., 1990. Hydrolytic weakening and penetrative  
16 deformation within a natural shear zone. *Geophys. Monogr.* 56, 21–36.  
17  
18  
19  
20 1219 Laul, J.C., Lepel, E.A., 1987. Rare earth element patterns in biotite muscovite and tourmaline  
21 minerals. *J. Radioanal. Nucl. Chem.* 112, 461–471.  
22  
23  
24  
25 1221 Le Breton, N., Thompson, A.B., 1988. Fluid-absent (dehydration) melting of biotite in  
26 metapelites in the early stages of crustal anatexis. *Contrib. Mineral. Petrol.* 99, 226–  
27 237.  
28  
29  
30  
31 1224 Lee, A.L., Torvela, T., Lloyd, G.E., Walker, A.M., 2018. Melt organisation and strain  
32 partitioning in the lower crust. *J. Struct. Geol.* 113, 188–199.  
33  
34  
35  
36 1226 Lin, L., Sawyer, E.W., 2019. Microstructure and compositional changes across biotite- rich  
37 reaction selvages around mafic schollen in a semipelitic diatexite migmatite. *J.*  
38 1227 *Metamorph. Geol.* 37, 539–566.  
39  
40  
41  
42  
43 1229 Lloyd, G.E., 2004. Microstructural evolution in a mylonitic quartz simple shear zone: the  
44 significant roles of dauphine twinning and misorientation. *Flow Processes in Faults and*  
45 1230 *Shear Zones.* *Geol. Soc. Spec. Publ.* 224, 39–61.  
46  
47  
48  
49  
50 1232 Lloyd, G.E., Freeman, B., 1994. Dynamic recrystallization of quartz under greenschist  
51 1233 conditions. *J. Struct. Geol.* 16, 867–881.  
52  
53  
54  
55 1234 Lloyd, G.E., Knipe, R.J., 1992. Deformation mechanisms accommodating faulting of quartzite  
56 1235 under upper crustal conditions. *J. Struct. Geol.* 14, 127–143.  
57  
58  
59  
60  
61  
62  
63  
64  
65

- 1236 Maidment, D.W., 2005. Palaeozoic high-grade metamorphism within the Centralian  
1  
2 1237 Superbasin, Harts Range region, central Australia. (Doctoral dissertation). Australian  
3  
4 1238 National University, Canberra, Australia.  
5
- 6  
7 1239 Maidment, D.W., Hand, M., Williams, I.S., 2005. Tectonic cycles in the Strangways  
8  
9 1240 Metamorphic Complex, Arunta Inlier, central Australia: geochronological evidence for  
10 1241 exhumation and basin formation between two high-grade metamorphic events. *Aust. J.*  
11  
12 1242 *Earth Sci.* 52, 205–215.  
13  
14
- 15 1243 Mancktelow, N.S., Pennacchioni, G., 2004. The influence of grain boundary fluids on the  
16  
17 1244 microstructure of quartz-feldspar mylonites. *J. Struct. Geol.* 26, 47–69.  
18  
19
- 20 1245 Markl, G., Bucher, K., 1998. Composition of fluids in the lower crust inferred from  
21  
22 1246 metamorphic salt in lower crustal rocks. *Nature* 391, 781–783.  
23  
24
- 25 1247 Markl, G., Piazzolo, S., 1998. Halogen-bearing minerals in syenites and high-grade marbles of  
26  
27 1248 Dronning Maud Land, Antarctica: monitors of fluid compositional changes during late-  
28  
29 1249 magmatic fluid-rock interaction processes. *Contrib. Mineral. Petrol.* 132, 246–268.  
30  
31
- 32 1250 Massonne, H.J., Schreyer, W., 1987. Phengite geobarometry based on the limiting assemblage  
33  
34 1251 with K-feldspar, phlogopite, and quartz. *Contrib. Mineral. Petrol.* 96, 212–224.  
35
- 36  
37 1252 Mawby, J., Hand, M., Foden, J., 1999. Sm-Nd evidence for high-grade ordovician  
38  
39 1253 metamorphism in the Arunta block, central Australia. *J. Metamorph. Geol.* 17, 653–  
40 1254 668.  
41  
42
- 43 1255 McCaig, A.M., Knipe, R.J., 1990. Mass-transport mechanisms in deforming rocks:  
44  
45 1256 Recognition, using microstructural and microchemical criteria. *Geology* 18, 824–827.  
46  
47
- 48 1257 McCaig, A.M., Wickham, S.M., Taylor, H.P., 1990. Deep fluid circulation in alpine shear  
49  
50 1258 zones, Pyrenees, France: field and oxygen isotope studies. *Contrib. Mineral. Petrol.*  
51  
52 1259 106, 41–60.  
53  
54
- 55 1260 McDonough, W.F., Sun, S.S., 1995. The composition of the Earth. *Chem. Geol.* 120, 223–253.  
56  
57  
58  
59  
60  
61  
62  
63  
64  
65

- 1261 Meek, U., Piazzolo, S., Daczko, N.R., 2019. The field and microstructural signatures of  
1 deformation-assisted melt transfer: Insights from magmatic arc lower crust, New  
2 Zealand. *J. Metamorph. Geol.* 37, 795–821.  
3  
4  
5  
6  
7 1264 Menegon, L., Fousseis, F., Stünitz, H., Xiao, X., 2015. Creep cavitation bands control porosity  
8 and fluid flow in lower crustal shear zones. *Geology* 43, 227–230.  
9  
10  
11 1266 Menegon, L., Pennacchioni, G., Spiess, R., 2008. Dissolution-precipitation creep of K-feldspar  
12 in mid-crustal granite mylonites. *J. Struct. Geol.* 30, 565–579.  
13  
14  
15  
16 1268 Menegon, L., Piazzolo, S., Pennacchioni, G., 2011. The effect of Dauphiné twinning on plastic  
17 strain in quartz. *Contrib. Mineral. Petrol.* 161, 635–652.  
18  
19  
20  
21 1270 Menzies, M., Murthy, V.R., 1980. Nd and Sr isotope geochemistry of hydrous mantle nodules  
22 and their host alkali basalts: Implications for local heterogeneities in metasomatically  
23 veined mantle. *Earth Planet. Sci. Lett.* 46, 323–334.  
24  
25  
26  
27  
28 1273 Milord, I., Sawyer, E.W., 2003. Schlieren formation in diatexite migmatite: Examples from the  
29 St Malo migmatite terrane, France. *J. Metamorph. Geol.* 21, 347–362.  
30  
31  
32  
33 1275 Möller, A., Williams, I.S., Jackson, S., Hensen, B.J., 1999. Palaeozoic deformation and mineral  
34 growth in the Strangways Metamorphic Complex: in-situ dating of zircon and monazite  
35 in a staurolite-corundum bearing shear zone. Abstracts 54. Geological Society of  
36 Australia 71–72.  
37  
38  
39  
40  
41 1279 Molnar, P., Dayem, K.E., 2010. Major intracontinental strike-slip faults and contrasts in  
42 lithospheric strength. *Geosphere* 6, 444–467.  
43  
44  
45  
46 1281 Morris, J.D., Leeman, W.P., Tera, F., 1990. The subducted component in island arc lavas:  
47 Constraints from Be isotopes and B–Be systematics. *Nature* 344, 31–36.  
48  
49  
50  
51 1283 Nachit, H., Ibhi, A., Abia, E. H., Ohoud, M.B., 2005. Discrimination between primary  
52 magmatic biotites, reequilibrated biotites and neoformed biotites. *C. R. Geosci.* 337,  
53 1415–1420.  
54  
55  
56  
57  
58 1286 Nachit, H., Razafimahefa, N.J.M.S., Stussi, J.M., Carron, J.P., 1985. Composition chimique  
59 des biotites et typologie magmatique des granitoides. *C. R. Acad. Sci.* 301, 813–818.  
60  
61  
62  
63  
64  
65

- 1288 Nash, W.P., Crecraft, H.R., 1985. Partition coefficients for trace elements in silicic  
1 1289 magmas. *Geochim. Cosmochim. Acta* 49, 2309–2322.  
2  
3  
4  
5 1290 Neiva, A.M.R., Silva, M.M.V.G., Gomes, M.E.P., Campos, T.F.C., 2002. Geochemistry of  
6 1291 coexisting biotite and muscovite of Portuguese peraluminous granitic differentiation  
7 series. *Chem. Erde* 62, 197–215.  
8  
9  
10  
11 1293 Norman, A.R., 1991. The structural and metamorphic evolution of the central Arunta Block:  
12 evidence from the Strangways Metamorphic Complex and the Harts Range Group,  
13 1294 central Australia. (Doctoral dissertation). Macquarie University, Sydney, Australia.  
14  
15 1295  
16  
17  
18 1296 O'Connor, P.J., Gallagher, V., Kennan, P.S., 1991. Genesis of lithium pegmatites from the  
19 Leinster Granite Margin, south-eastern Ireland: Geochemical constraints. *Geol. J.* 26,  
20 1297 295–305.  
21  
22 1298  
23  
24  
25 1299 Oliver, N.H.S., Valenta, R.K., Wall, V.J., 1990. The effect of heterogeneous stress and strain on  
26 metamorphic fluid flow, Mary Kathleen, Australia, and a model for large-scale fluid  
27 1300 circulation. *J. Metamorph. Geol.* 8, 311–331.  
28  
29 1301  
30  
31  
32 1302 Paterson, D., De Jonge, M.D., Howard, D.L., Lewis, W., McKinlay, J., Starritt, A., Kusel, M.,  
33 1303 Ryan, C.G., Kirkham, R., Moorhead, G. Siddons, D.P., 2011. The X- ray fluorescence  
34 microscopy beamline at the Australian synchrotron. *AIP Conference Proceedings* 1365,  
35 1304 219-222.  
36  
37 1305  
38  
39  
40 1306 Patiño-Douce, A.E., Beard, J.S., 1995. Dehydration-melting of biotite gneiss and quartz  
41 amphibolite from 3 to 15 kbar. *J. Petrol.* 36, 707–738.  
42 1307  
43  
44  
45 1308 Paton, C., Hellstrom, J., Paul, B., Woodhead, J., Hergt, J., 2011. Iolite: Freeware for the  
46 visualisation and processing of mass spectrometric data. *J. Anal. At. Spectrom.* 26,  
47 1309 2508–2518.  
48  
49 1310  
50  
51  
52 1311 Payne, J.L., Hand, M., Barovich, K.M., Wade, B.P., 2008. Temporal constraints on the timing  
53 of high-grade metamorphism in the northern Gawler Craton: implications for assembly  
54 1312 of the Australian Proterozoic. *Aust. J. Earth Sci.* 55, 623–640.  
55 1313  
56  
57  
58  
59  
60  
61  
62  
63  
64  
65

- 1314 Piazolo, S., Bestmann, M., Prior, D.J., Spiers, C.J., 2006. Temperature dependent grain  
1 boundary migration in deformed-then-annealed material: observations from  
2 1315 experimentally deformed synthetic rocksalt. *Tectonophysics* 427, 55–71.  
3  
4 1316  
5  
6 1317 Piazolo, S., Bons, P.D., Jessell, M.W., Evans, L., Passchier, C.W., 2002. Dominance of  
7 1318 microstructural processes and their effect on microstructural development: Insights  
8 from numerical modelling of dynamic recrystallization. *Geol. Soc. Spec. Publ.* 200,  
9 149–170.  
10 1319  
11  
12 1320  
13  
14  
15 1321 Piazolo, S., Daczko, N., Silva, D., Raimondo, T., 2020. Melt-present shear zones enable  
16 intracontinental orogenesis. *Geology* 48, 643–648.  
17 1322  
18  
19  
20 1323 Piazolo, S., Jessell, M.W., Bons, P.D., Evans, L., Becker, J.K., 2010. Numerical simulations of  
21 microstructures using the Elle platform: a modern research and teaching tool. *J. Geol.*  
22 1324 *Soc. India* 75, 110–127.  
23  
24 1325  
25  
26  
27 1326 Pichon, X.L., Henry, P., Lallemand, S., 1993. Accretion and erosion in subduction zones: the  
28 role of fluids. *Annu. Rev. Earth Planet. Sci.* 21, 307–331.  
29 1327  
30  
31  
32 1328 Prakash, A., Piazolo, S., Saha, L., Bhattacharya, A., Pal, D.K., Sarkar, S., 2018. Deformation  
33 1329 behavior of migmatites: Insights from microstructural analysis of a garnet–sillimanite–  
34 mullite–quartz–feldspar-bearing anatectic migmatite at Rampura–Agucha, Aravalli–  
35 1330 Delhi Fold Belt, NW India. *Int. J. Earth Sci.* 107, 2265–2292.  
36  
37 1331  
38  
39  
40 1332 Prent, A.M., Beinlich, A., Raimondo, T., Kirkland, C.L., Evans, N.J., Putnis, A., 2020. Apatite  
41 and monazite: An effective duo to unravel superimposed fluid-flow and deformation  
42 1333 events in reactivated shear zones. *Lithos* 376, 105752.  
43  
44 1334  
45  
46  
47 1335 Putnis, A., 2009. Mineral replacement reactions. *Rev. Mineral. Geochem.* 70, 87–124.  
48  
49  
50 1336 Putnis, A., Austrheim, H., 2010. Fluid-induced processes: Metasomatism and  
51 metamorphism. *Geofluids* 10, 254–269.  
52 1337  
53  
54  
55 1338 Putnis, A., Putnis, C.V., 2007. The mechanism of reequilibration of solids in the presence of a  
56 fluid phase. *J. Solid State Chem.* 180, 1783–1786.  
57 1339  
58  
59  
60  
61  
62  
63  
64  
65

- 1340 Raimondo, T., Clark, C., Hand, M., Cliff, J., Harris, C., 2012. High- resolution geochemical  
1 record of fluid–rock interaction in a mid-  
2 1341 crustal shear zone: a comparative study of  
3 major element and oxygen isotope transport in garnet. *J. Metamorph. Geol.* 30, 255–  
4 1342 280.  
5 1343  
6  
7  
8 1344 Raimondo, T., Clark, C., Hand, M., Faure, K., 2011. Assessing the geochemical and tectonic  
9 impacts of fluid–rock interaction in mid-crustal shear zones: a case study from the  
10 1345 intracontinental Alice Springs orogen, central Australia. *J. Metamorph. Geol.* 29, 821–  
11 1346 850.  
12  
13  
14 1347  
15  
16  
17 1348 Raimondo, T., Hand, M., Collins, W.J., 2014. Compressional intracontinental orogens: Ancient  
18 and modern perspectives. *Earth Sci. Rev.* 130, 128–153.  
19 1349  
20  
21  
22 1350 Rajesh, V.J., Arima, M., Santosh, M., 2004. Dunite, glimmerite and spinellite in Achankovil  
23 Shear Zone, South India: implications for highly potassic CO<sub>2</sub>-rich melt influx along  
24 1351 an intra-continental shear zone. *Gondwana Res.* 7, 961–974.  
25 1352  
26  
27  
28 1353 Rakotondrazafy, R., Pierdzig, S., Raith, M.M., Hoernes, S., 1997. Phlogopite-mineralisations  
29 in the Beraketa belt of southern Madagascar: a spectacular example of channelised fluid  
30 1354 flow and fluid–rock interaction. *Gondwana Res. Group Misc. Pub.* 5, 81–82.  
31  
32 1355  
33  
34  
35 1356 Rasband, W.S., 1997–2018. ImageJ, U. S. National Institutes of Health. Bethesda, MD, USA.  
36  
37 1357 <http://imagej.nih.gov/ij/>.  
38  
39  
40 1358 Roberts, E.A., Houseman, G.A., 2001. Geodynamics of central Australia during the intraplate  
41 Alice Springs Orogeny: thin viscous sheet models. *Geol. Soc. Spec. Publ.* 184, 139–  
42 1359 164.  
43  
44 1360  
45  
46  
47 1361 Rosenberg, C.L., 2004. Shear zones and magma ascent: a model based on a review of the  
48 Tertiary magmatism in the Alps. *Tectonics* 23, TC302.  
49 1362  
50  
51  
52 1363 Rosenberg, C.L., Handy, M.R., 2005. Experimental deformation of partially melted granite  
53 revisited: implications for the continental crust. *J. Metamorph. Geol.* 23, 19–28.  
54 1364  
55  
56  
57 1365 Ruiz-Agudo, E., Putnis, C.V., Putnis, A., 2014. Coupled dissolution and precipitation at  
58 1366 mineral–fluid interfaces. *Chem. Geol.* 383, 132–146.  
59  
60  
61  
62  
63  
64  
65

- 1367 Ryan, C.G., Cousens, D.R., Sie, S.H., Griffin, W.L., 1990. Quantitative analysis of PIXE  
1368 spectra in geoscience applications. *Nucl. Instrum. Methods Phys. Res. B* 49, 271–276.  
1369 Ryan, C.G., Jamieson, D.N., Churms, C.L., Pilcher, J.V., 1995. A new method for on-line true-  
1370 elemental imaging using PIXE and the proton microprobe. *Nucl. Instrum. Methods*  
1371 *Phys. Res. B* 104, 157–165.  
1372 Ryan, C.G., Kirkham, R., Hough, R.M., Moorhead, G., Siddons, D.P., De Jonge, M.D.,  
1373 Paterson, D.J., De Geronimo, G., Howard, D.L. Cleverley, J.S., 2010. Elemental X-ray  
1374 imaging using the Maia detector array: The benefits and challenges of large solid-  
1375 angle. *Nucl. Instrum. Methods Phys. Res. A* 619, 37–43.  
1376 Ryan, C.G., Laird, J.S., Fisher, L.A., Kirkham, R., Moorhead, G.F., 2015. Improved Dynamic  
1377 Analysis method for quantitative PIXE and SXRF element imaging of complex  
1378 materials. *Nucl. Instrum. Methods Phys. Res. B* 363, 42–47.  
1379 Sawyer, E.W., 1999. Criteria for the recognition of partial melting. *Phys. Chem. Earth A* 24,  
1380 269–279.  
1381 Sawyer, E.W., 2008. Atlas of migmatites. *Can. Mineral., Spec. Publ. 9*. NRC Research press,  
1382 Ottawa, Canada.  
1383 Sawyer, E.W., Cesare, B., Brown, M., 2011. When the continental crust melts. *Elements* 7,  
1384 229–234.  
1385 Schmidt, M.W., Poli, S., 1998. Experimentally based water budgets for dehydrating slabs and  
1386 consequences for arc magma generation. *Earth Planet. Sci. Lett.* 163, 361–379.  
1387 Schulmann, K., Martelat, J.E., Ulrich, S., Lexa, O., Štípská, P., Becker, J.K., 2008. Evolution  
1388 of microstructure and melt topology in partially molten granitic mylonite: Implications  
1389 for rheology of felsic middle crust. *J. Geophys. Res. Solid Earth* 113, B10406.  
1390 Scrimgeour, I.R., 2003. Developing a revised framework for the Arunta Region. In: Munson,  
1391 T.J., Scrimgeour, I.R. (eds.), *Annual Geoscience Exploration Seminar (AGES) Record*  
1392 *of Abstracts*. Northern Territory Geological Survey, Record 2003-001, Darwin, 1–8.

- 1393 Scrimgeour, I.R., 2013. Aileron Province, In: Ahmad, M., Munson, T. J. (eds.), *Geology and*  
1  
2 1394 *Mineral Resources of the Northern Territory*. Northern Territory Geological Survey,  
3  
4 1395 *Spec. Publ. 5*.  
5
- 6  
7 1396 Selverstone, J., Morteani, G. Staude, J.M., 1991. Fluid channelling during ductile shearing:  
8  
9 1397 transformation of gran- odiorite into aluminous schist in the Tauern Window, eastern  
10 1398 Alps. *J. Metamorph. Geol.* 9, 419–431.  
11  
12
- 13 1399 Seydoux-Guillaume, A.M., Montel, J.M., Bingen, B., Bosse, V., De Parseval, P., Paquette, J.  
14  
15 1400 L., Janots, E., Wirth, R., 2012. Low-temperature alteration of monazite: Fluid mediated  
16  
17 1401 coupled dissolution–precipitation, irradiation damage, and disturbance of the U-Pb and  
18  
19 1402 Th-Pb chronometers. *Chem. Geol.* 330, 140–158.  
20  
21
- 22 1403 Shaw, R.D., Stewart, A.T., Black, L.P., 1984. The Arunta Inlier: a complex ensialic mobile belt  
23  
24 1404 in central Australia. Part 2: tectonic history. *Aust. J. Earth Sci.* 31, 457–484.  
25  
26
- 27 1405 Sibson, R.H., 1994. Crustal stress, faulting and fluid flow. *Geol. Soc. Spec. Publ.* 78, 69–84.  
28  
29
- 30 1406 Sibson, R.H., Robert, F., Poulsen, K.H., 1988. High-angle reverse faults, fluid-pressure  
31  
32 1407 cycling, and mesothermal gold-quartz deposits. *Geology* 16, 551–555.  
33  
34
- 35 1408 Silva, D., Piazzolo, S., Daczko, N.R., Houseman, G., Raimondo, T., Evans, L., 2018.  
36  
37 1409 Intracontinental Orogeny Enhanced by Far- Field Extension and Local Weak  
38  
39 1410 Crust. *Tectonics* 37, 4421–4443.  
40
- 41 1411 Skemer, P., Katayama, I., Jiang, Z., Karato, S.I., 2005. The misorientation index: Development  
42  
43 1412 of a new method for calculating the strength of lattice-preferred  
44  
45 1413 orientation. *Tectonophysics* 411, 157–167.  
46  
47
- 48 1414 Smart, K.A., Tappe, S., Ishikawa, A., Pfänder, J.A., Stracke, A., 2019. K-rich hydrous mantle  
49  
50 1415 lithosphere beneath the Ontong Java Plateau: Significance for the genesis of oceanic  
51  
52 1416 basalts and Archean continents. *Geochim. Cosmochim. Acta* 248, 311–342.  
53  
54
- 55 1417 Smith, J.R., Piazzolo, S., Daczko, N.R., Evans, L., 2015. The effect of pre- tectonic reaction  
56  
57 1418 and annealing extent on behaviour during subsequent deformation: insights from paired  
58  
59  
60  
61  
62  
63  
64  
65

- 1419 shear zones in the lower crust of Fiordland, New Zealand. *J. Metamorph. Geol.* 33,  
1 557–577.  
2  
3  
4  
5 1421 Sobolev, A.V., Chaussidon, M., 1996. H<sub>2</sub>O concentrations in primary melts from supra-  
6 subduction zones and mid-ocean ridges: Implications for H<sub>2</sub>O storage and recycling in  
7 1422 the mantle. *Earth Planet. Sci. Lett.* 137, 45–55.  
8  
9  
10  
11 1424 Spruzeniece, L., Piazzolo, S., 2015. Strain localization in brittle-ductile shear zones: fluid-  
12 abundant vs. fluid-limited conditions (an example from Wyangala area, Australia).  
13 1425 *Solid Earth* 6, 881–901.  
14  
15 1426  
16  
17  
18 1427 Stepanov, A.S., Hermann, J., 2013. Fractionation of Nb and Ta by biotite and phengite:  
19 Implications for the “missing Nb paradox”. *Geology* 41, 303–306.  
20  
21  
22  
23 1429 Stern, R.J., 2002. Subduction zones. *Rev. Geophys.* 40, 1–38.  
24  
25  
26 1430 Stipp, M., Stunitz, H., Heilbronner, R., Schmid, S.M., 2002a. Dynamic recrystallization of  
27 quartz: correlation between natural and experimental conditions. *J. Geol. Soc. London*  
28 1431 200, 171–190.  
29  
30 1432  
31  
32  
33 1433 Stipp, M., Stunitz, H., Heilbronner, R., Schmid, S.M., 2002b. The eastern Tonale fault zone: a  
34 ‘natural laboratory’ for crystal plastic deformation of quartz over a temperature range  
35 1434 from 250 to 700°C. *J. Struct. Geol.* 24, 1861–1884.  
36  
37 1435  
38  
39  
40 1436 Stipp, M., Tullis, J., Scherwath, M., Behrmann, J.H., 2010. A new perspective on  
41 1437 paleopiezometry: Dynamically recrystallized grain size distributions indicate  
42 mechanism changes. *Geology* 38, 759–762.  
43 1438  
44  
45  
46 1439 Stuart, C.A., Daczko, N.R., Piazzolo, S., 2017. Local partial melting of the lower crust triggered  
47 by hydration through melt–rock interaction: an example from Fiordland, New Zealand.  
48 1440 *J. Metamorph. Geol.* 35, 213–230.  
49  
50 1441  
51  
52  
53 1442 Stuart, C.A., Meek, U., Daczko, N.R., Piazzolo, S., Huang, J.X., 2018a. Chemical signatures of  
54 melt–rock interaction in the root of a magmatic arc. *J. Petrol.* 59, 321–340.  
55 1443  
56  
57  
58  
59  
60  
61  
62  
63  
64  
65

- 1444 Stuart, C.A., Piazzolo, S., Daczko, N.R., 2016. Mass transfer in the lower crust: Evidence for  
1 incipient melt assisted flow along grain boundaries in the deep arc granulites of  
2 1445 Fiordland, New Zealand. *Geochem. Geophys. Geosyst.* 17, 3733–3753.  
3  
4 1446  
5  
6 1447 Stuart, C.A., Piazzolo, S., Daczko, N.R., 2018b. The recognition of former melt flux through  
7 1448 high- strain zones. *J. Metamorph. Geol.* 36, 1049–1069.  
8  
9  
10  
11 1449 Stussi, J.M., Cuney, M., 1996. Nature of biotites from alkaline, calc-alkaline and peraluminous  
12 1450 magmas by Abdel-Fattah M. Abdel-Rahman: a comment. *J. Petrol.* 37, 1025–1029.  
13  
14  
15  
16 1451 Tappe, S., Foley, S.F., Jenner, G.A., Heaman, L.M., Kjarsgaard, B.A., Romer, R.L., Stracke,  
17 1452 A., Joyce, N., Hoefs, J., 2006. Genesis of ultramafic lamprophyres and carbonatites at  
18 1453 Aillik Bay, Labrador: a consequence of incipient lithospheric thinning beneath the  
19 1454 North Atlantic craton. *J. Petrol.* 47, 1261–1315.  
20  
21  
22  
23  
24  
25 1455 Tetley, M.G., Daczko, N.R., 2014. Virtual Petrographic Microscope: a multi-platform  
26 1456 education and research software tool to analyse rock thin-sections. *Aust. J. Earth Sci.*  
27 1457 61, 631–637.  
28  
29  
30  
31 1458 Teyssier, C., 1985. A crustal thrust system in an intracratonic tectonic environment. *J. Struct.*  
32 1459 *Geol.* 7, 689–700.  
33  
34  
35  
36 1460 Thompson A.B., Connolly J.A.D., 1992. Migration of metamorphic fluid – some aspects of  
37 1461 mass and heat transfer. *Earth Sci. Rev.* 32, 107–21.  
38  
39  
40  
41 1462 Thompson, A.B., 1982. Dehydration melting of pelitic rocks and the generation of H<sub>2</sub>O-  
42 1463 undersaturated granitic liquids. *Am. J. Sci.* 282, 1567–1595.  
43  
44  
45  
46 1464 Varga, J., Raimondo, T., Daczko, N., Adam, J., 2020. Experimental alteration of monazite in  
47 1465 granitic melt: Variable U-Th-Pb and REE mobility during melt-mediated coupled  
48 1466 dissolution-precipitation. *Chem. Geol.* 544, 119602.  
49  
50  
51  
52  
53 1467 Vernon, R.H., 2011. Microstructures of melt-bearing regional metamorphic rocks. *Mem. Geol.*  
54 1468 *Soc. Am.* 207, 1–11.  
55  
56  
57  
58 1469 Vignerresse, J.L., 1995. Crustal regime of deformation and ascent of granitic magma.  
59 1470 *Tectonophysics* 249, 187–202.  
60  
61  
62  
63  
64  
65

- 1471 Waters, F.G., 1987. A suggested origin of MARID xenoliths in kimberlites by high pressure  
1472 crystallization of an ultrapotassic rock such as lamproite. *Contrib. Mineral. Petrol.* 95,  
1473 523–533.
- 1474 Watson, E.B., Baxter, E.F., 2007. Diffusion in solid-Earth systems. *Earth Planet. Sci. Lett.* 253,  
1475 307–327.
- 1476 Weinberg, R.F., Hasalová, P., 2015. Water-fluxed melting of the continental crust: A review.  
1477 *Lithos* 212, 158–188.
- 1478 Weinberg, R.F., Sial, A.N., Pessoa, R.R., 2001. Magma flow within the Tavares pluton,  
1479 northeastern Brazil: Compositional and thermal convection. *Geol. Soc. Am. Bull.* 113,  
1480 508–520.
- 1481 Wheeler, J., 2014. Dramatic effects of stress on metamorphic reactions. *Geology* 42, 647–650.
- 1482 White, S.T., Knipe, R.J., 1978. Transformation-and reaction-enhanced ductility in rocks. *J.*  
1483 *Geol. Soc. London* 135, 513–516.
- 1484 Whitney, D.L., Evans, B.W., 2010. Abbreviations for names of rock-forming minerals. *Am.*  
1485 *Mineral.* 95, 185–187.
- 1486 Winter, J.D., 2013. *Principles of Igneous and Metamorphic Petrology*. Pearson education,  
1487 London, U.K.
- 1488 Wintsch, R.P., Christoffersen, R., Kronenberg, A.K., 1995. Fluid–rock reaction weakening of  
1489 fault zones. *J. Geophys. Res. Solid Earth* 100, 13021–13032.
- 1490 Wyllie, P.J., Sekine, T., 1982. The formation of mantle phlogopite in subduction zone  
1491 hybridization. *Contrib. Mineral. Petrol.* 79, 375–380.
- 1492 Yardley, B.W., 2009. The role of water in the evolution of the continental crust. *J. Geol. Soc.*  
1493 *London* 166, 585–600.
- 1494 Žák, J., Verner, K., Týcová, P., 2008. Grain-scale processes in actively deforming magma  
1495 mushes: New insights from electron backscatter diffraction (EBSD) analysis of biotite  
1496 schlieren in the Jizera granite, Bohemian Massif. *Lithos* 106, 309–322.

1497 Závada, P., Schulmann, K., Racek, M., Hasalová, P., Jeřábek, P., Weinberg, R.F., Štípská, P.,  
1498 Roberts, A., 2018. Role of strain localization and melt flow on exhumation of deeply  
1499 subducted continental crust. *Lithosphere* 10, 217–238.

## FIGURE CAPTIONS

**Fig. 1.** Generalised geological map of the southeastern Arunta Region, emphasising the distribution of regional schistose high strain zones (yellow structures numbered on map) that cross-cut the dominantly granulite and amphibolite facies rocks comprising this basement terrane. Also represented are the regional anastomosing high-strain zones and thrust faults. Simplified structural cross-section A–A' (modified after Raimondo *et al.*, 2014) shows the principal crustal discontinuities and high-strain zones in the Arunta Region associated with the Alice Springs Orogeny (Collins & Teyssier, 1989; Ballèvre *et al.*, 2000; Maidment, 2005; Raimondo *et al.*, 2011; Scrimgeour, 2013). Regional high strain zones: #1 Gough Dam shear zone (GDSZ); #2 West Bore shear zone; #3 Wallaby Knob shear zone; #4 Yambah shear zone; #5 Southern Cross shear zone; #6 Harry Creek shear zone (HCSZ); #7 Erontonga/Two Mile Bore shear zone; #8 Illogwa shear zone; #9 Delny shear zone; #10 Yalbadjandi shear zone. AB, Amadeus Basin; GB, Georgina Basin; HRG, Harts Range Group; SMC, Strangways Metamorphic Complex; RAR, Reynolds-Anmatjira Ranges.

**Fig. 2.** Photographs of outcrops and collected samples representative of strained rocks in the Gough Dam shear zone, from (a) outer area of the shear zone; (b, c) adjacent to the central area of the shear zone; and (d–i) central area of the shear zone. (d) Outcrop looking west of meter-scale glimmerite schist with a well-developed foliation (S1, white line) that contains layers and lenses of felsic rock types (i.e., granitic gneiss and quartzite mylonite). Elongated quartzite mylonite (along S1) and granitic gneiss bodies are surrounded by glimmerite schist. Field sense of shear is north-up reverse (along a steeply-plunging L1); (e) Granitic gneiss elongated along S1 surrounded by glimmerite schist and granite lenses. Granite lenses in glimmerite schist are elongate parallel to S1 foliation. Glimmerite embayments (white arrows) are observed in the granitic gneiss body; (f) Magnification of granitic gneiss lenses 'invaded' by glimmerite along fractures at a high angle to the foliation; (g) Quartzite mylonite in glimmerite schist unit surrounded and cross-cut at a high angle to the foliation by glimmerite seams. Some K-feldspar grains are present in the glimmerite schist; (h) Magnification of the sampled quartzite mylonite

1529 hosting sample GD1609A (L-Qtz) within the glimmerite schist unit surrounded by glimmerite  
1530 seams. Less glimmerite ‘invaded’ along high angle fractures to the foliation is observed; (i)  
1531 Quartzite mylonite samples GD1609B–C (H-Qtz, M-Qtz and GL samples, respectively).  
1532 Glimmerite seams warp around and ‘invade’ the quartzite mylonite, involving most of the H-  
1533 Qtz sample.

**Fig. 3.** Back-scattered electron (BSE) images of thin sections from (a) to (d) granite mylonite  
1534 outcrop in Fig 2a; (e) to (h) glimmerite schist outcrop in Fig 2b; and (i) to (l) glimmerite schist  
1535 outcrop in Fig 2c, containing the following microstructures highlighted by coloured triangles:  
1536 yellow – interstitial grains and/or finger-like protrusions; blue – grains terminating with  
1537 apparent low dihedral angles; purple – myrmekitic intergrowth of quartz and plagioclase; green  
1538 – triple junction of K-feldspar grains presenting straight grain boundaries and  $\sim 120^\circ$  dihedral  
1539 angles. Mineral abbreviations follow Whitney & Evans (2010).

**Fig. 4.** Petrography and X-ray elemental mapping of quartzite samples L-Qtz, H-Qtz and M-  
1540 Qtz/GL. (a–c) Crossed-polarised light thin section photomicrographs in top image and thin  
1541 section  $\mu$ -XRF maps in bottom image. Magenta triangles highlight high grain mobility features  
1542 in quartz grains; blue triangles highlight bands rich in sillimanite that are inferred to be former  
1543 melt migration pathways and include pockets inferred to have pseudomorphed melt; (d) Plane-  
1544 polarised light photomicrograph of sillimanite-rich bands in sample H-Qtz (blue triangles); (e)  
1545 Synchrotron X-ray elemental concentration maps of Sr and Cu for area shown in image (d)  
1546 highlighting the emplacement of a cryptic Si-Al alteration product (red arrows) relative to  
1547 biotite (green arrows), plagioclase (white arrows) and quartz grains (light blue arrows). Mineral  
1548 abbreviations follow Whitney & Evans (2010).

**Fig. 5.** BSE and cathodoluminescence images of inferred melt microstructures present in (a–c)  
1549 H-Qtz and (d–j) M-Qtz/GL samples. (a) Inferred melt pocket displayed in Fig. 4b, d and e, with  
1550 peraluminous granite mineral assemblage. Biotite has interlocking boundaries with  
1551 surrounding quartz and finger-like protrusions (yellow arrows); (b, c) Biotite, muscovite and  
1552 sillimanite microstructures; (b) Biotite and muscovite grains presenting elongated interstitial  
1553 grains/finger-like protrusions (yellow arrows) and low apparent dihedral angles (blue arrows)  
1554 between other grains; (c) Biotite located in sample H-Qtz showing interlocking boundary with  
1555 quartz (yellow arrow); (d–f) Biotite, muscovite and sillimanite microstructures; (d) Biotite  
1556 grain presenting elongated interstitial grains/finger-like protrusions (outside field of view of

1563 thin section shown in Fig. 4c; yellow arrows); (e) Sillimanite grains in quartzite showing  
1564 perpendicular fractures filled with a cryptic alteration product of Si-Al composition (labelled  
1565 Alt.); (f) Biotite and quartz grains wrapping around a large, deformed muscovite grain (outside  
1566 field of view of thin section shown in Fig. 4c); (g–j) Cathodoluminescence images for selected  
1567 regions in sample M-Qtz, showing quartz and biotite grain contacts. Dashed lines highlight  
1568 darker luminescent regions mostly at quartz grain boundaries when in contact with biotite  
1569 grains. Yellow arrows highlight narrow dark bands inferred to be healed fractures within or at  
1570 quartz grain boundaries. Mineral abbreviations follow Whitney & Evans (2010).

1571  
1572 **Fig. 6.** Euler angles and inverse pole figure (IPF) maps describing the interconnectivity of  
1573 neoformed quartz grains and quartzite mylonite dissolution in M-Qtz/GL samples. (a) Crossed-  
1574 polarised light thin section photomicrograph of sample M-Qtz. Blue triangles indicate  
1575 sillimanite-rich bands and red triangles indicate irregular quartz grain shapes; (b) Euler map of  
1576 quartz grains for the area shown in panel (a), shown in more detail in (c) and (d) where similarly  
1577 oriented intragranular quartz grains are identified in respective groups adjacent to the  
1578 sillimanite-rich domain; (e) Quartz IPF map for M-Qtz and GL contact zone (see Fig. 4c for  
1579 location), with colour coding relative to the Z-axis and other phases shown as band contrast.  
1580 Euler angle rotation is coloured as  $\psi$  - red,  $\theta$  - green and  $\phi$  - blue.

1581  
1582 **Fig. 7.** Description of quartz grains preferential orientation in H-Qtz, M-Qtz and GL samples;  
1583 inverse pole figure (IPF) with colour coding relative to the Z-axis for (a) M-Qtz and GL  
1584 samples, and (d) H-Qtz sample. Regions displayed in each sample represent individual quartz  
1585 orientation calculation subsets; (b, c) and (e, f) EBSD-derived quartz crystallographic  
1586 orientation pole figures and neighbouring quartz pair misorientation angle distributions (blue  
1587 bars) for the respective samples and displayed regions. Note that scale bars for pole figure  
1588 contouring vary between pole figures.

1589  
1590 **Fig. 8.** Graph depicting the mean area weighted quartz grain size for the different regions  
1591 shown in Fig. 7.

1592  
1593 **Fig. 9.** Harker diagrams for whole rock major oxides ( $\text{Al}_2\text{O}_3$ ,  $\text{TiO}_2$ ,  $\text{FeO}$ ,  $\text{MgO}$  and  $\text{K}_2\text{O}$  vs  
1594  $\text{SiO}_2$ ) for selected rock types present in the Strangways Metamorphic Complex, sample GL  
1595 (this study) and the average biotite composition for peraluminous granites (Neiva *et al.*, 2002).

1596 See Table S2 for all data references. Standard deviation for average biotite composition  
1597 displayed only if larger than the symbol.

1598  
1599 **Fig. 10.** Graphical representation of biotite geochemical evolution between all samples from  
1600 main study area. (a) Ti atoms per formula unit (a.p.f.u.) vs  $X_{Mg}$  diagram for biotite from all  
1601 samples; (b) Al vs Mg a.p.f.u. classification diagram for biotite in igneous rocks (after Nachit  
1602 *et al.*, 1985 and Stussi & Cuney, 1996); (c) Ternary diagram  $TiO_2 \times 10 - (FeO + Mn) - MgO$  for  
1603 discrimination between primary magmatic, reequilibrated and neoformed biotites (Nachit *et*  
1604 *al.*, 2005); (d)  $P-T$  diagram for Gough Dam shear zone samples, using Ti in biotite for  
1605 temperature (Henry *et al.*, 2005) and Si in phengite for barometry (Massonne & Schreyer,  
1606 1987).

1607  
1608 **Fig. 11.** Chondrite-normalised trace elements and REE patterns for biotite in (a–c) Gough Dam  
1609 shear zone samples and (d) literature compilation (migmatite leucosome, Bea *et al.*, 1994b;  
1610 pegmatite, Hulsbosch *et al.*, 2014; mica schist, Laul & Lepel, 1987; peraluminous granite, Bea  
1611 *et al.*, 1994a; metapelite enclave, Acosta-Vigil *et al.*, 2010; experimental Nb-Ta, Stepanov &  
1612 Hermann, 2013; rhyodacite, Nash & Crecraft, 1985). Selected rocks are detailed in Table S4.  
1613 Colours for samples L-Qtz, H-Qtz and M-Qtz/GL correspond to those used for symbols in other  
1614 diagrams.

1615  
1616 **Fig. 12.** Bivariate plots for Ti vs Ba, Ti vs Sc, Ti vs Nb/Ta and Ti vs Li from Gough Dam  
1617 shear zone samples and additional data from El Hoyazo enclaves (Table S4; Acosta-Vigil *et*  
1618 *al.*, 2010). Black error bars represent the measured uncertainty ( $2\sigma$ ) of an individual analysis;  
1619 red error bars represent the standard deviation ( $2\sigma$ ) of multiple analyses.

1620  
1621 **Fig. 13.** Textural relationships for monazite grains in (a–b) sample GL with higher biotite  
1622 modal composition, and (c–d) sample M-Qtz with lower biotite modal composition.

1623  
1624 **Fig. 14.** Monazite morphology, texture and U-Pb geochronology from sample M-Qtz/GL. (a)  
1625 Morphology and textures of representative monazite grains from sample M-Qtz in back-  
1626 scattered electron (BSE) imaging.  $^{206}Pb/^{238}U$  ages with associated errors (2 SE) are displayed,  
1627 and full analytical results are given in Table S5. White arrows indicate inward-penetrating  
1628 boundary interfaces between dark and light BSE response and yellow arrows indicate thorite  
1629 inclusions; (b) Tera-Wasserburg concordia plot showing U-Pb geochronological data from

1630 samples M-Qtz and GL and kernel density estimation for data with < 2% discordance. Linear  
1631 regression age estimates are calculated using only sample M-Qtz analyses.

1632  
1633 **Fig. 15.** Schematic block models showing the metasomatic (*s.l.*) evolution of the Gough Dam  
1634 shear zone and formation of meter-scale glimmerite zones via melt-rock interaction. (a) Shear  
1635 zone melt inflow at the inception stage (*c.* 450 Ma): south-directed thrust shear of granulite  
1636 terranes in the Arunta Region. Melt sourced from lower crustal levels infiltrates and flows  
1637 upward along lithological boundaries and pre-existing foliations. Melt flow intensity is higher  
1638 towards the centre of the shear zone; (b) Shear zone metasomatism (*s.l.*) at the final stage (*c.*  
1639 370 Ma): shear zone glimmerite formation with increasing biotite content towards the centre  
1640 of the deformation zone. Granitic lenses close to the shear zone boundaries increase in size and  
1641 morph into sheets towards the centre of the shear zone; (c) Inset of main glimmerite domain in  
1642 the Gough Dam shear zone, summarising the melt-rock interaction structures from this study.  
1643 Orthogonal fragmentation of quartzite mylonite lenses due to rheological contrast enhances  
1644 melt flow and subsequent melt-rock interaction to form glimmerite. HRG, Harts Range Group;  
1645 SMC, Strangways Metamorphic Complex.

1646  
1647 **Table 1:** Electron microprobe data of key minerals from the reacted quartzites and  
1648 glimmerite seams in the Gough Dam shear zone.

1649  
1650 **Table 2:** Representative LA-ICP-MS trace element and REE compositional data for biotite  
1651 grains from the Gough Dam shear zone, and comparison to published data from multiple  
1652 locations and formation settings exogenous to the study area.

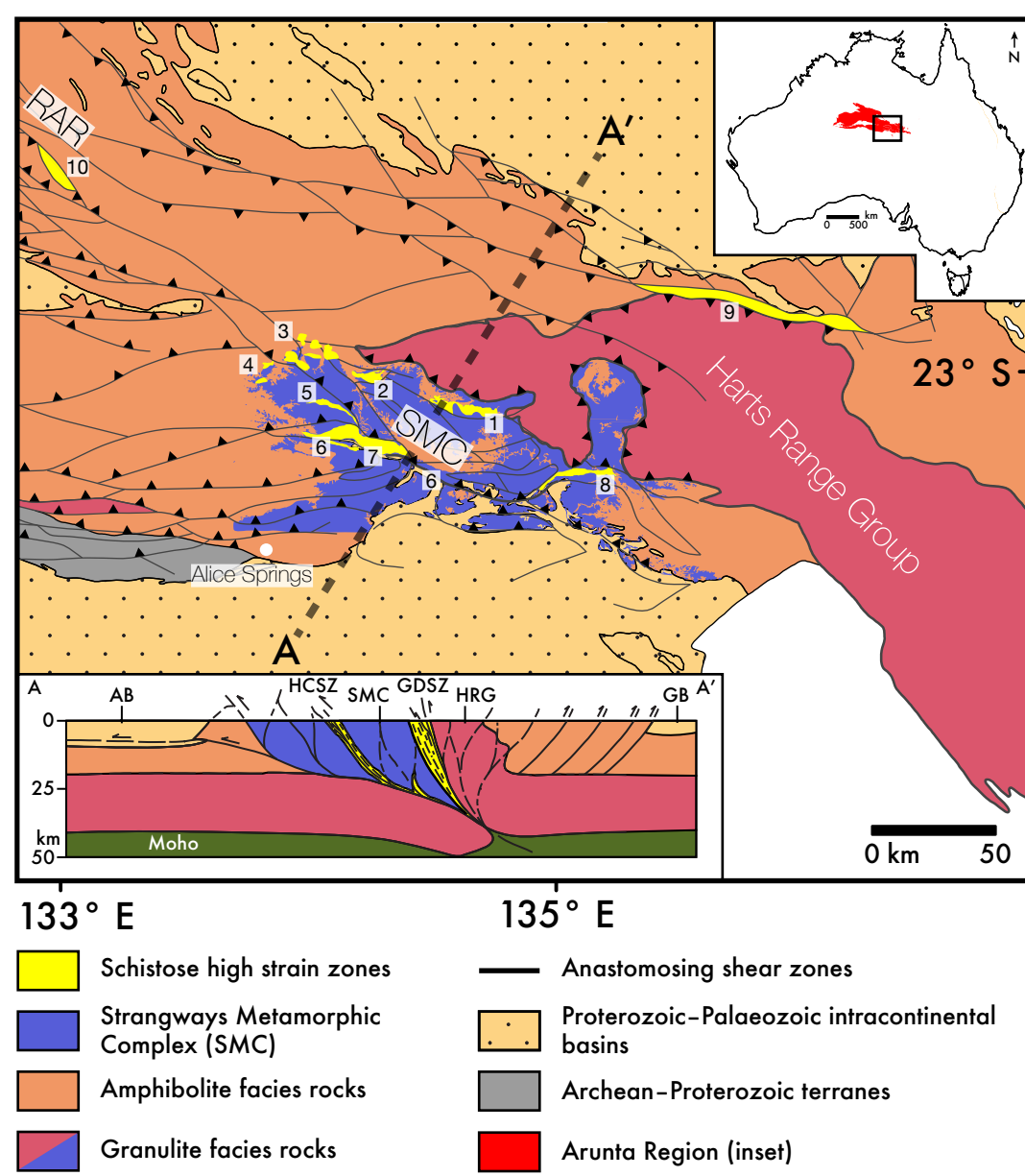
1653  
1654 **Table 3:** Calculation of the melt volume forming hydrous minerals in a high-strain zone for  
1655 samples L-Qtz and H-Qtz.

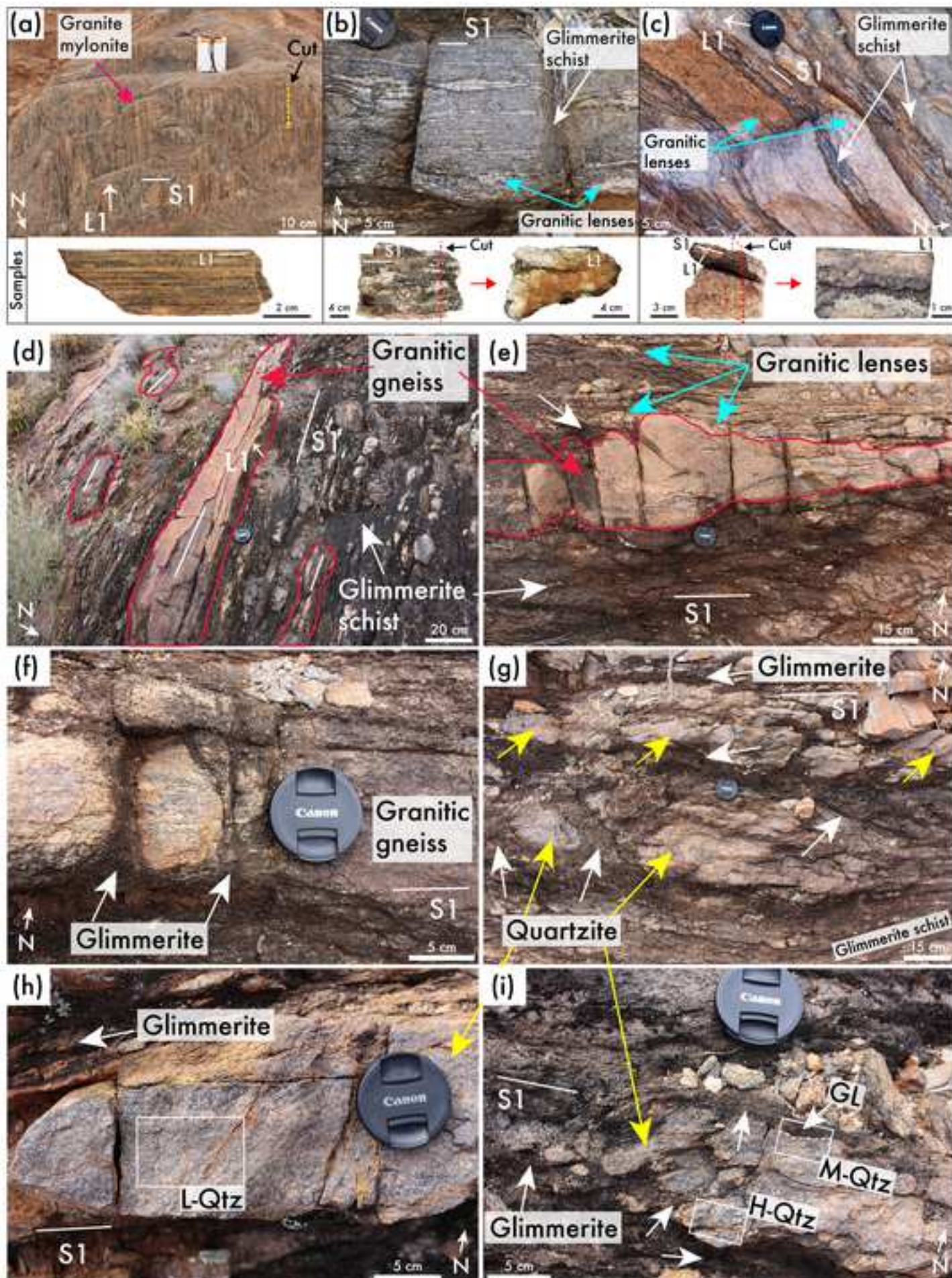
## 1656 1657 1658 **SUPPLEMENTARY DATA**

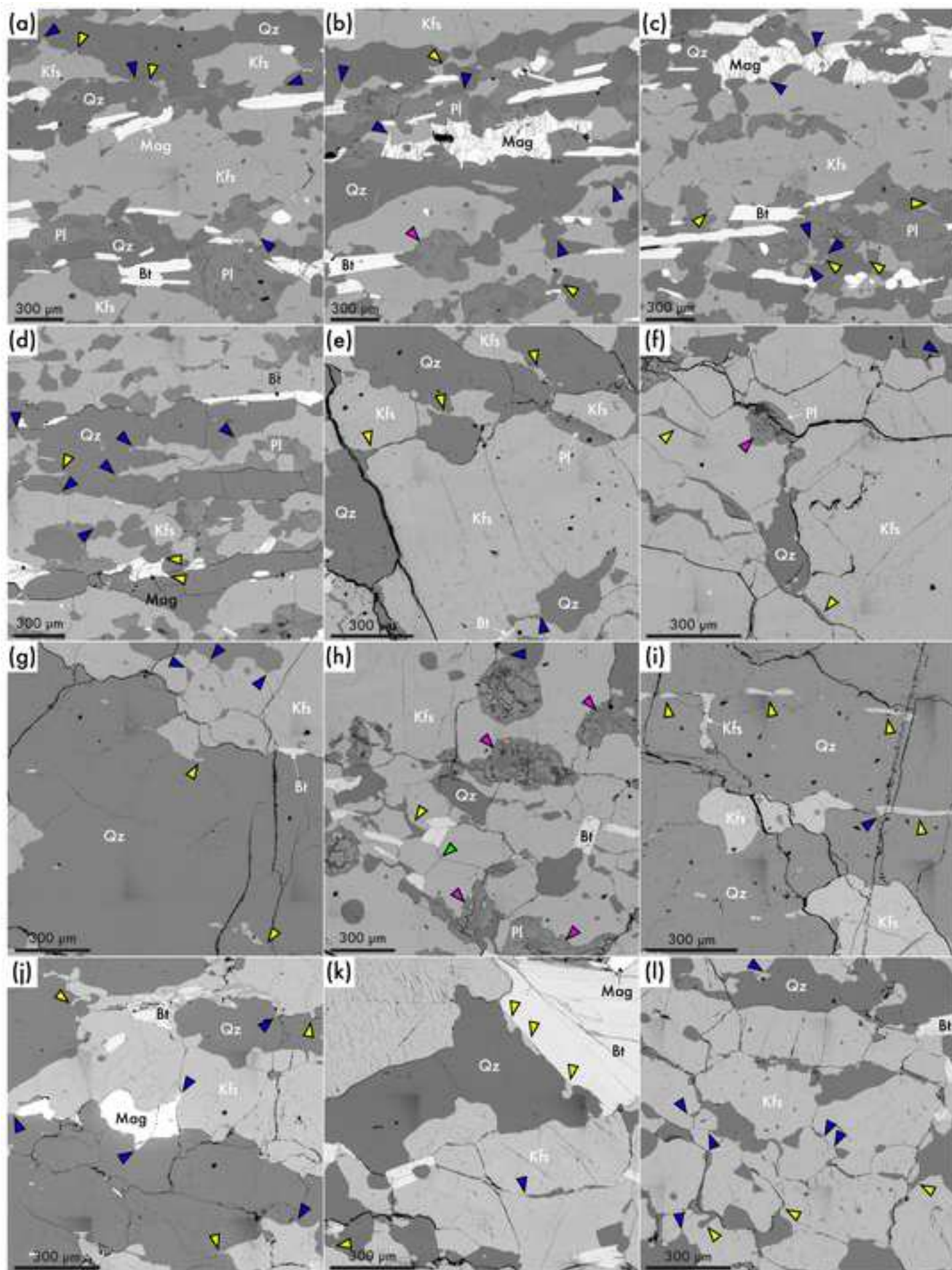
1659  
1660 **Fig. S1.** Back-scattered electron (BSE) image showing the spatial distribution of monazite ages  
1661 in sample M-Qtz/GL.

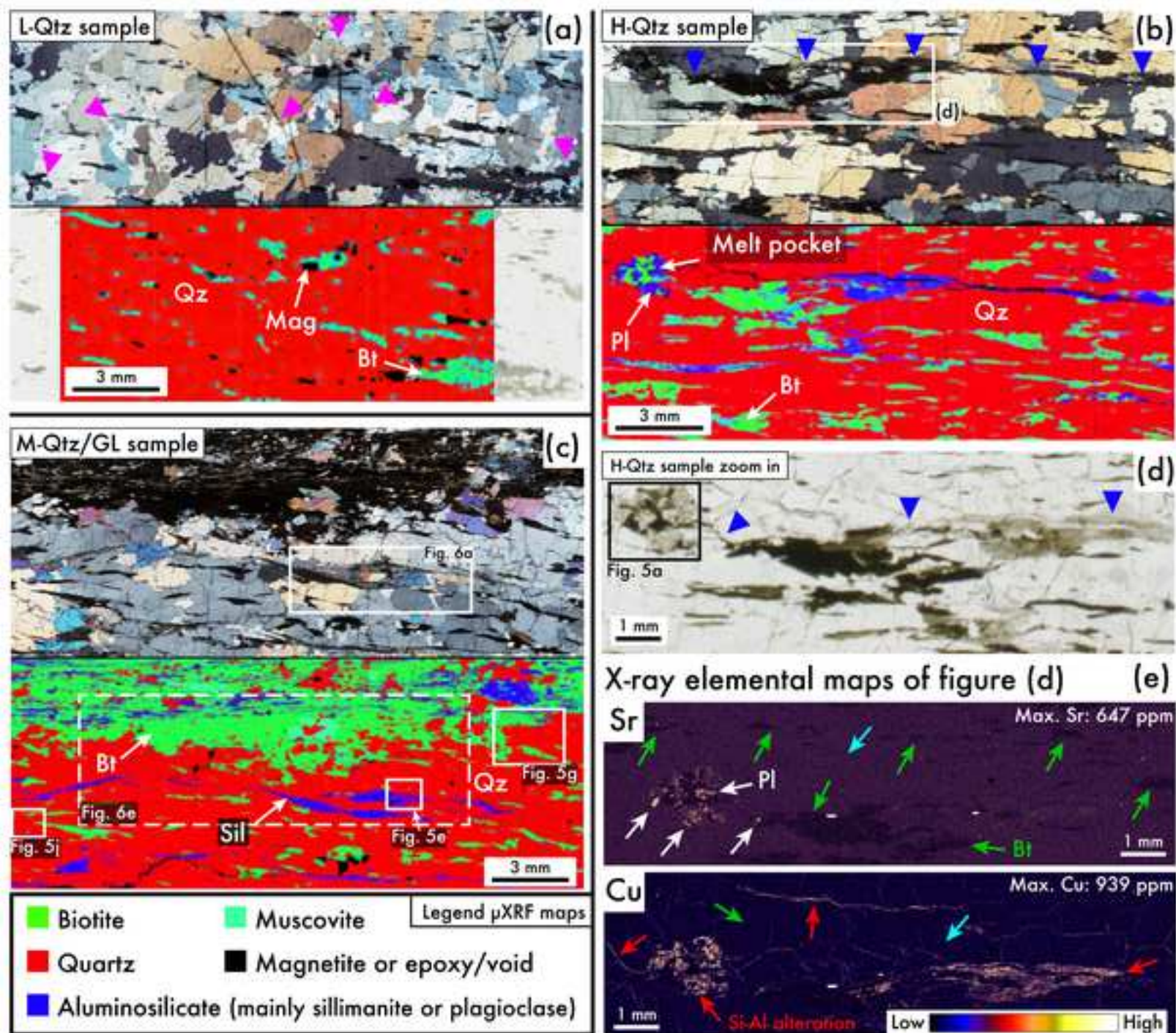
1662

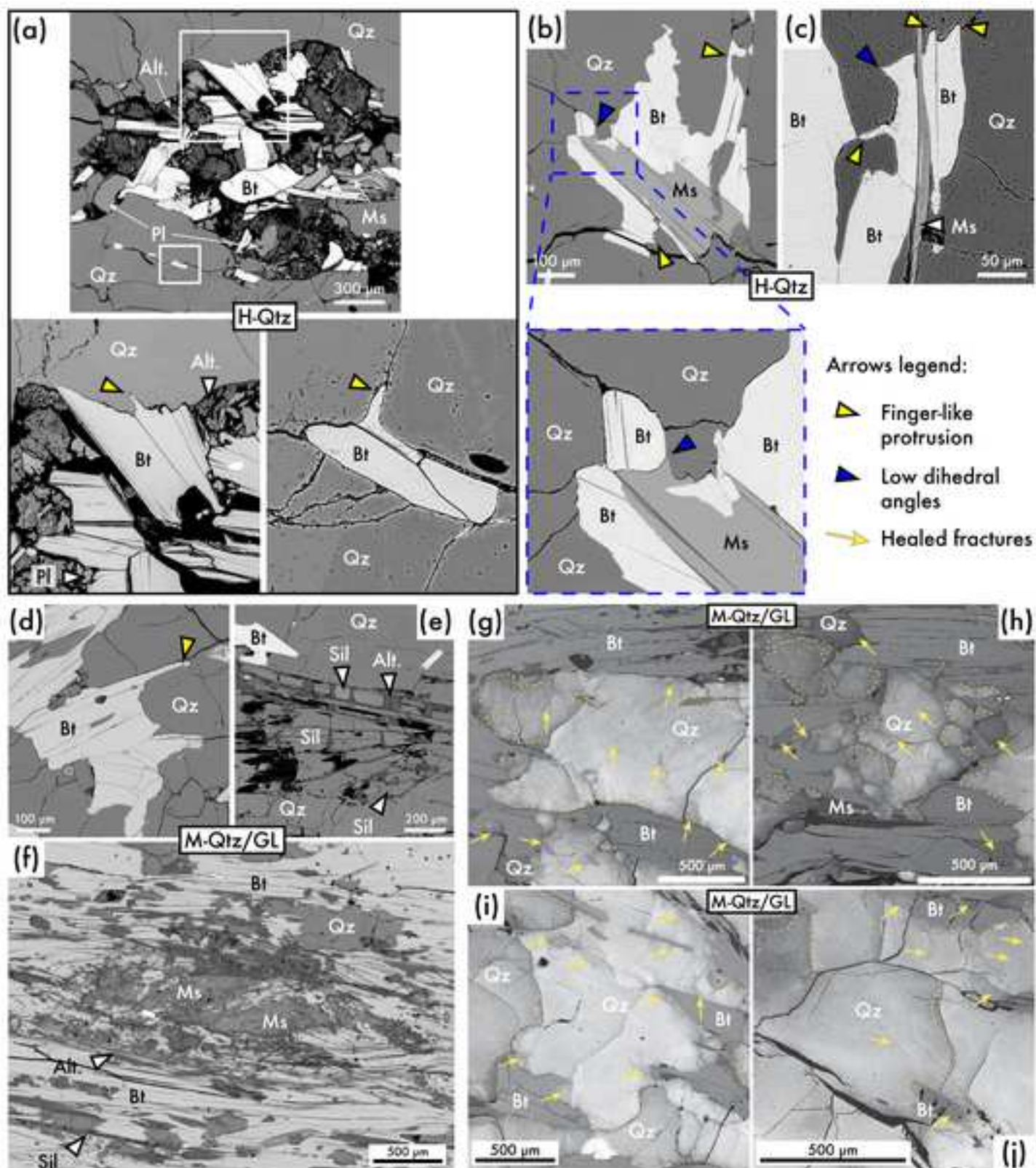
1663 **Table S1:** Electron microprobe data of additional minerals from reacted quartzites and  
1  
2 1664 glimmerite seams in the Gough Dam shear zone.  
3  
4 1665  
5 1666 **Table S2:** Whole rock major oxide concentrations for sample GL in comparison to average  
6  
7 1667 peraluminous granite from the literature and major rock types of the Strangways Metamorphic  
8  
9 1668 Complex.  
10  
11 1669  
12  
13 1670 **Table S3:** LA-ICP-MS biotite trace element data.  
14  
15 1671  
16 1672 **Table S4:** Description of biotite samples from the literature for comparison with those sampled  
17  
18 1673 from the Gough Dam shear zone.  
19  
20  
21 1674 **Table S5:** LA-ICP-MS monazite U-Pb data.  
22  
23  
24  
25  
26  
27  
28  
29  
30  
31  
32  
33  
34  
35  
36  
37  
38  
39  
40  
41  
42  
43  
44  
45  
46  
47  
48  
49  
50  
51  
52  
53  
54  
55  
56  
57  
58  
59  
60  
61  
62  
63  
64  
65

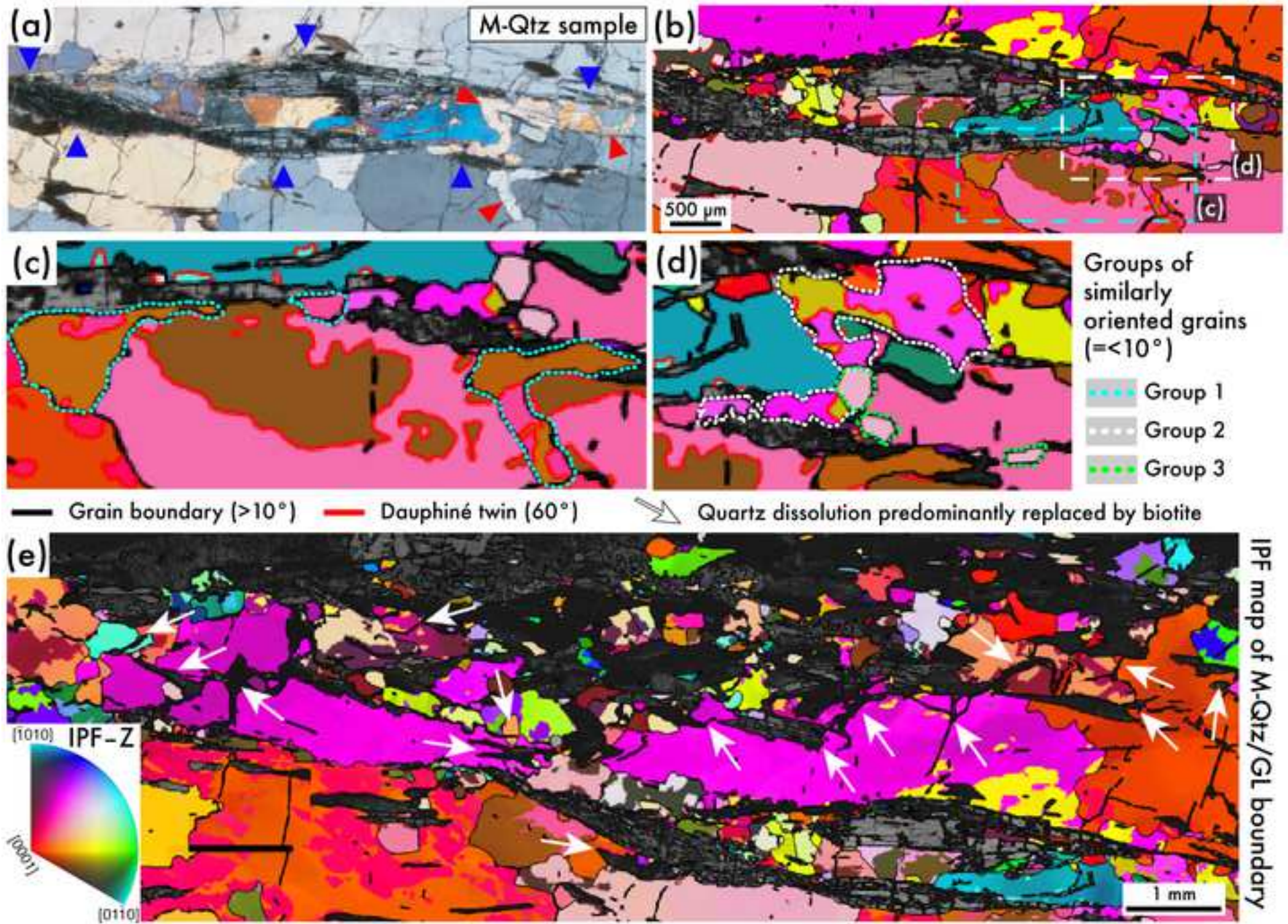


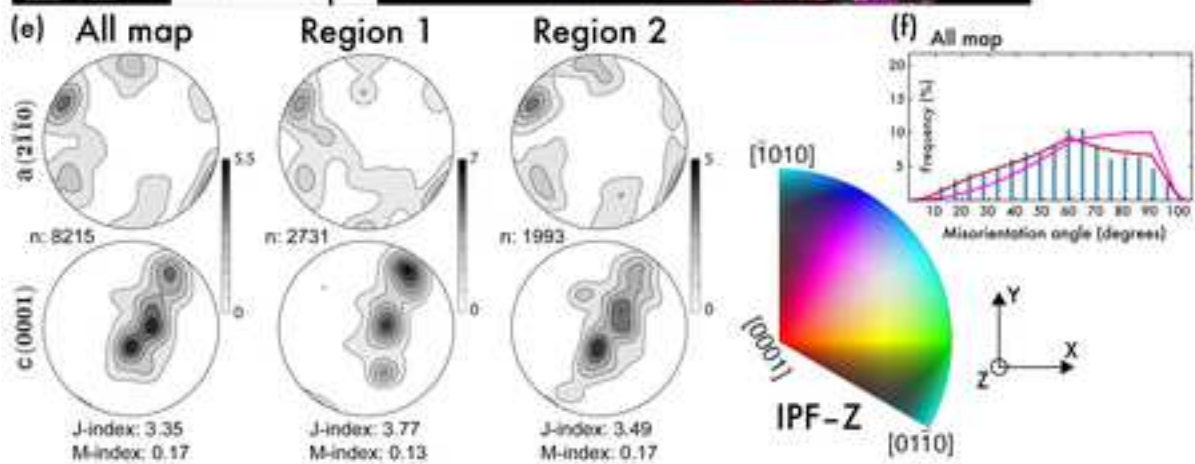
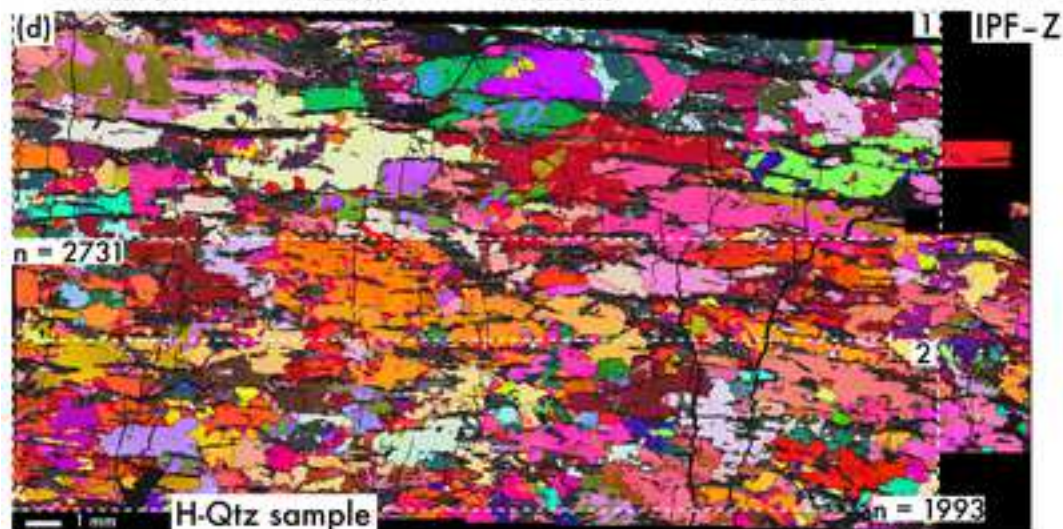
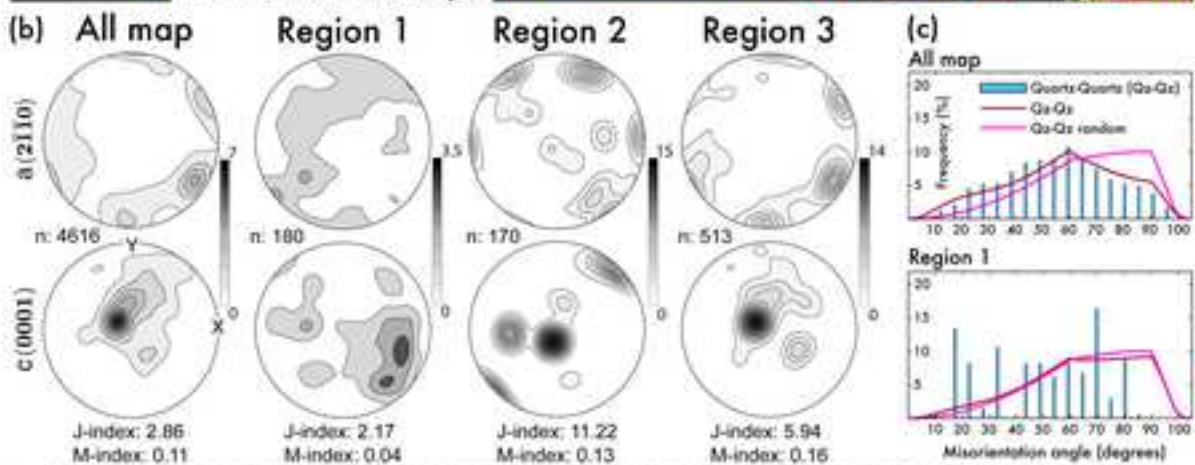
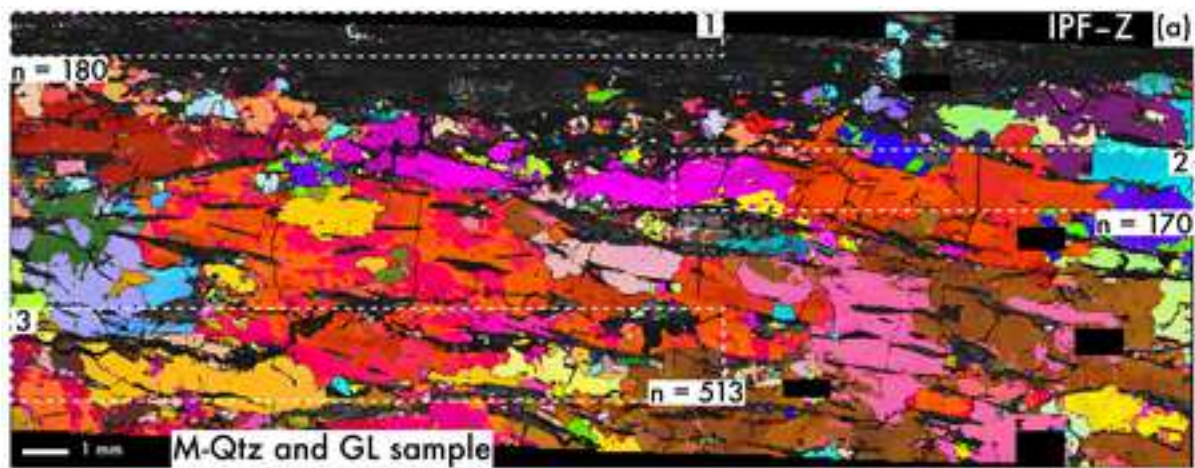


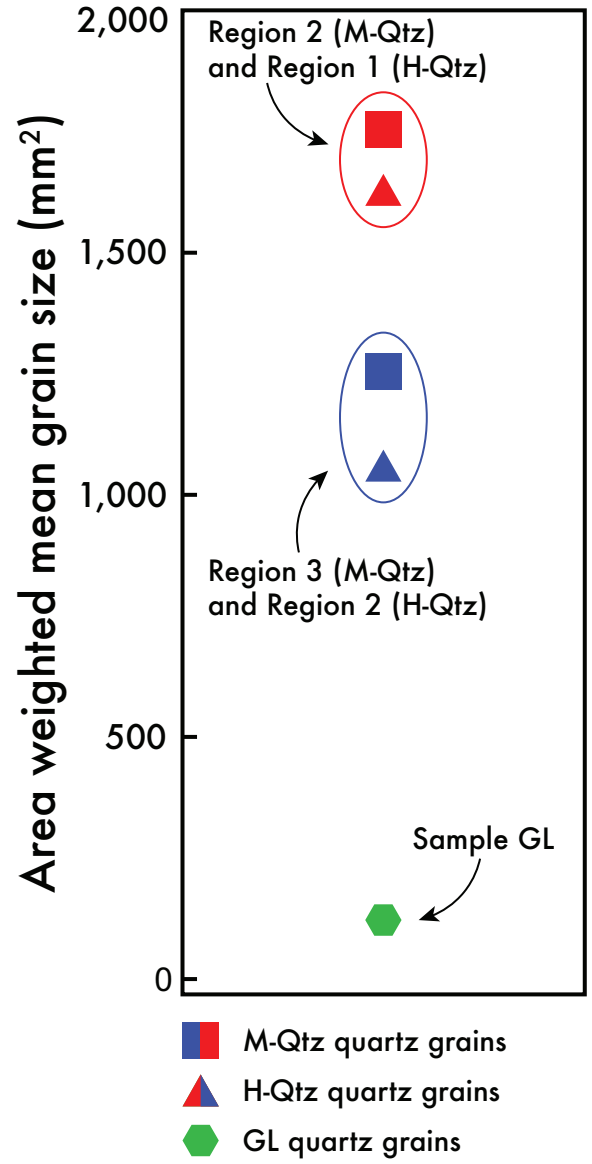












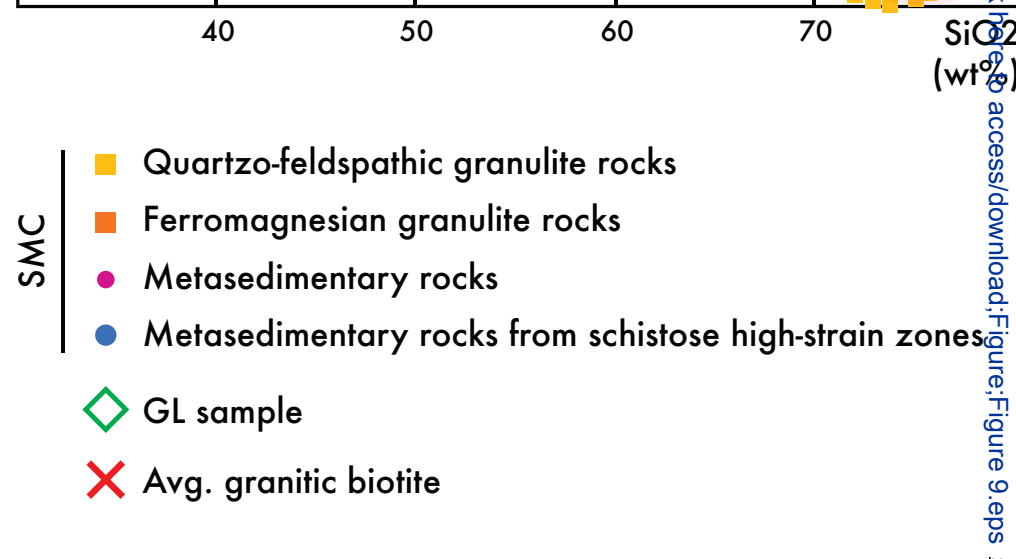
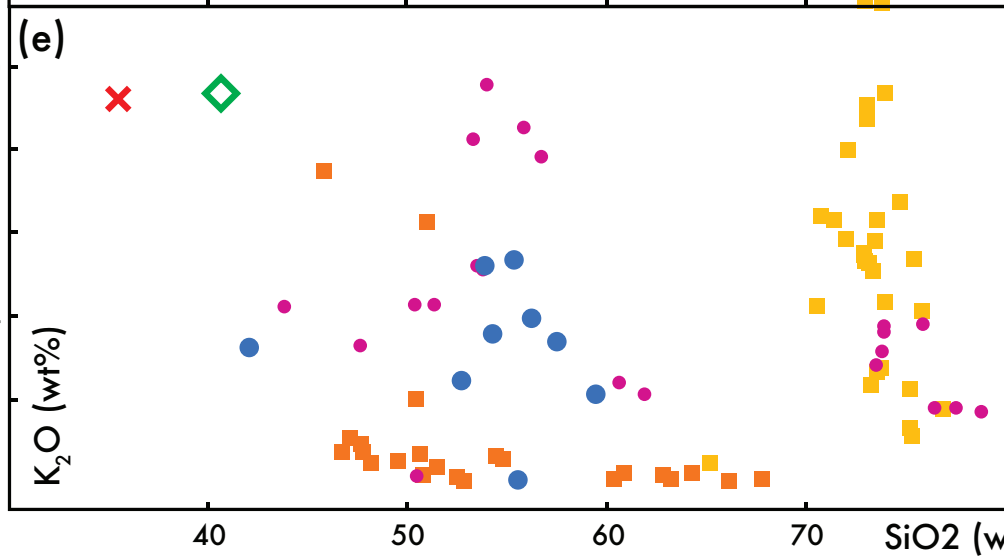
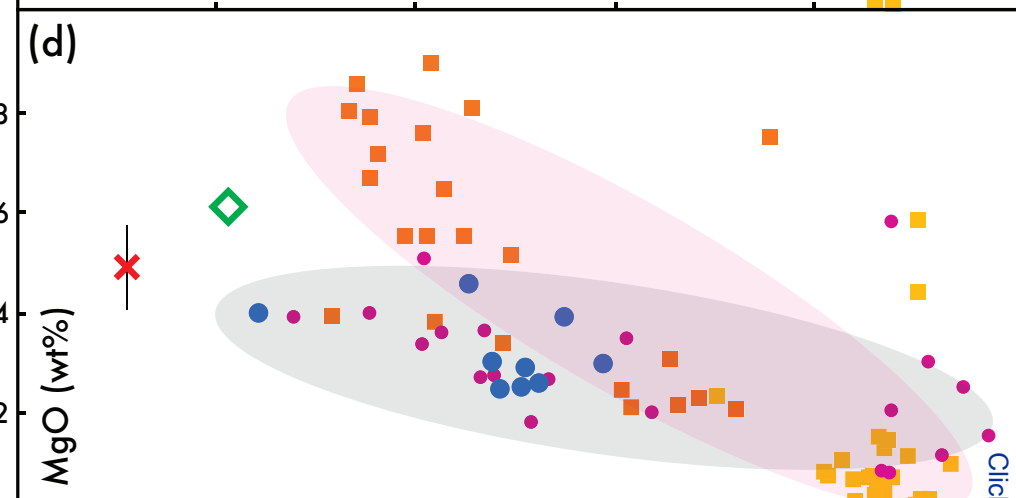
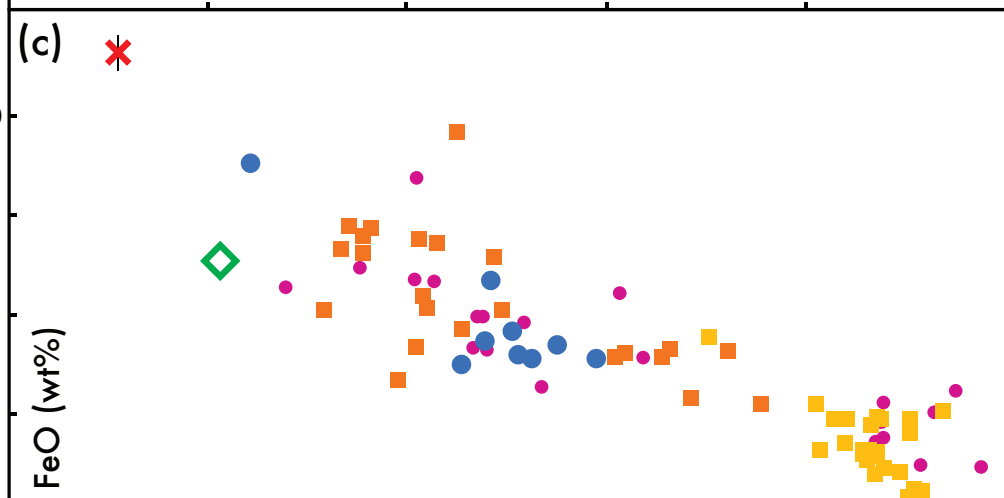
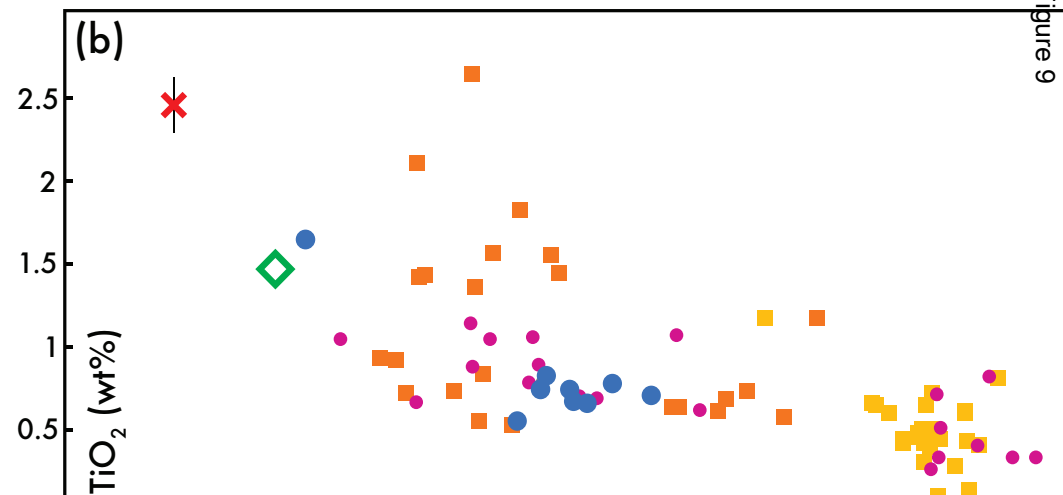
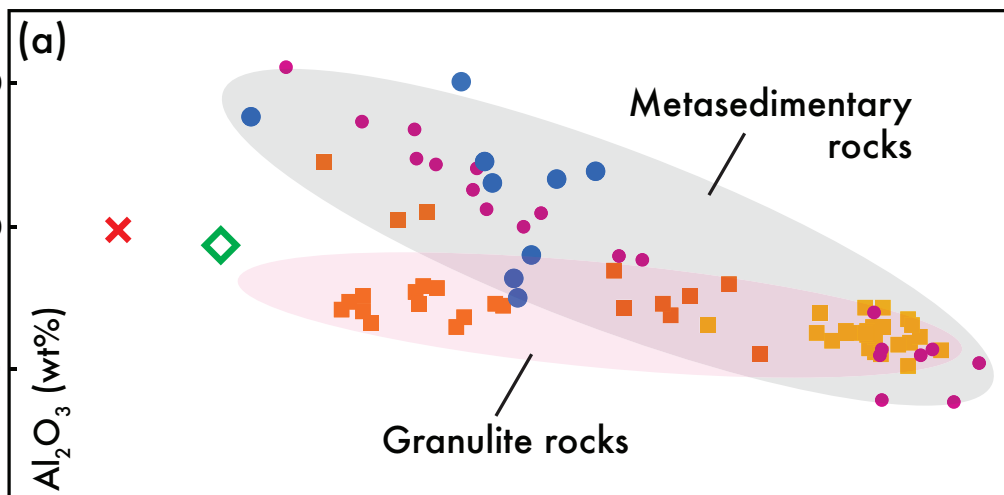
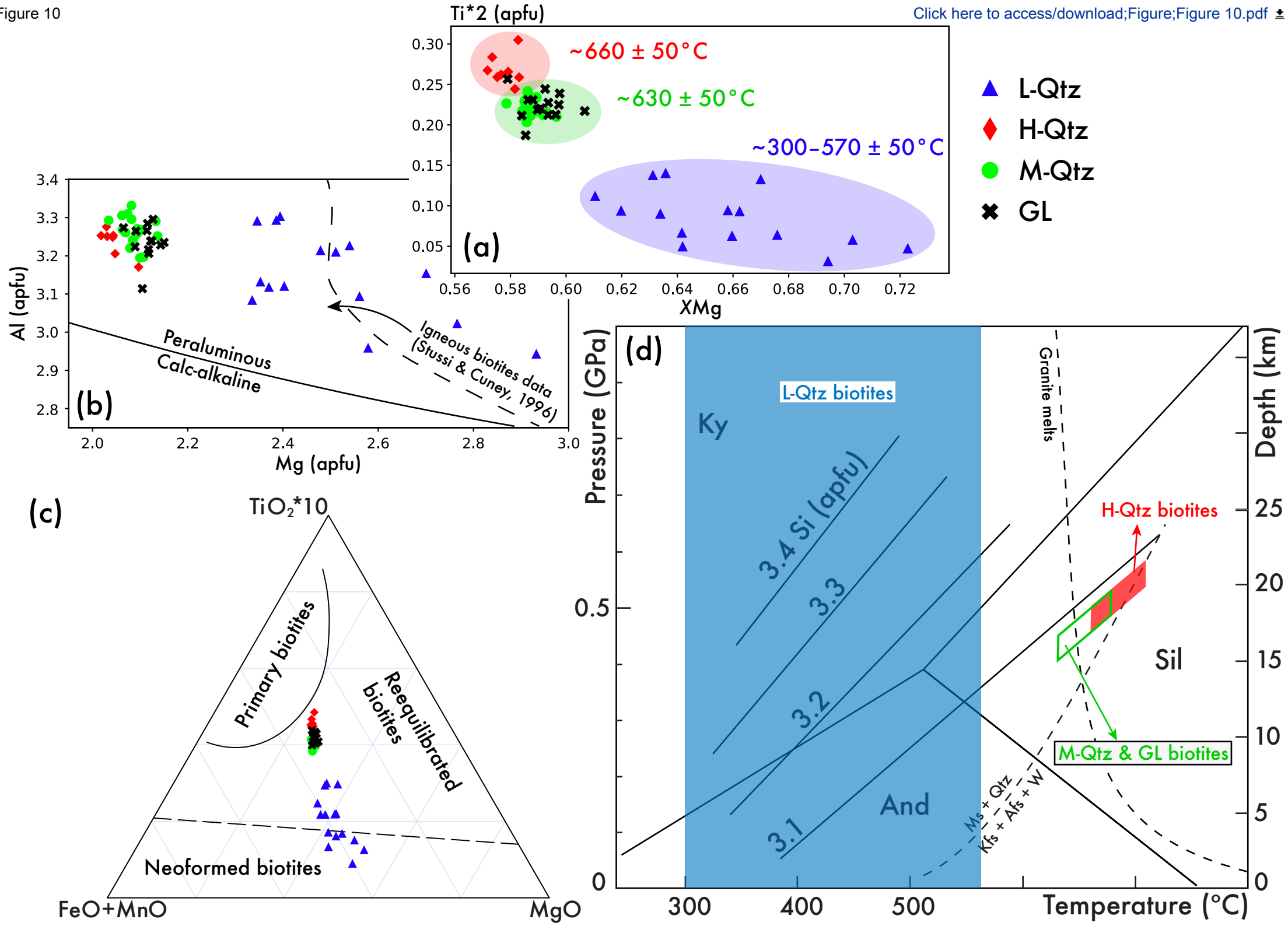


Figure 10

[Click here to access/download;Figure;Figure 10.pdf](#)

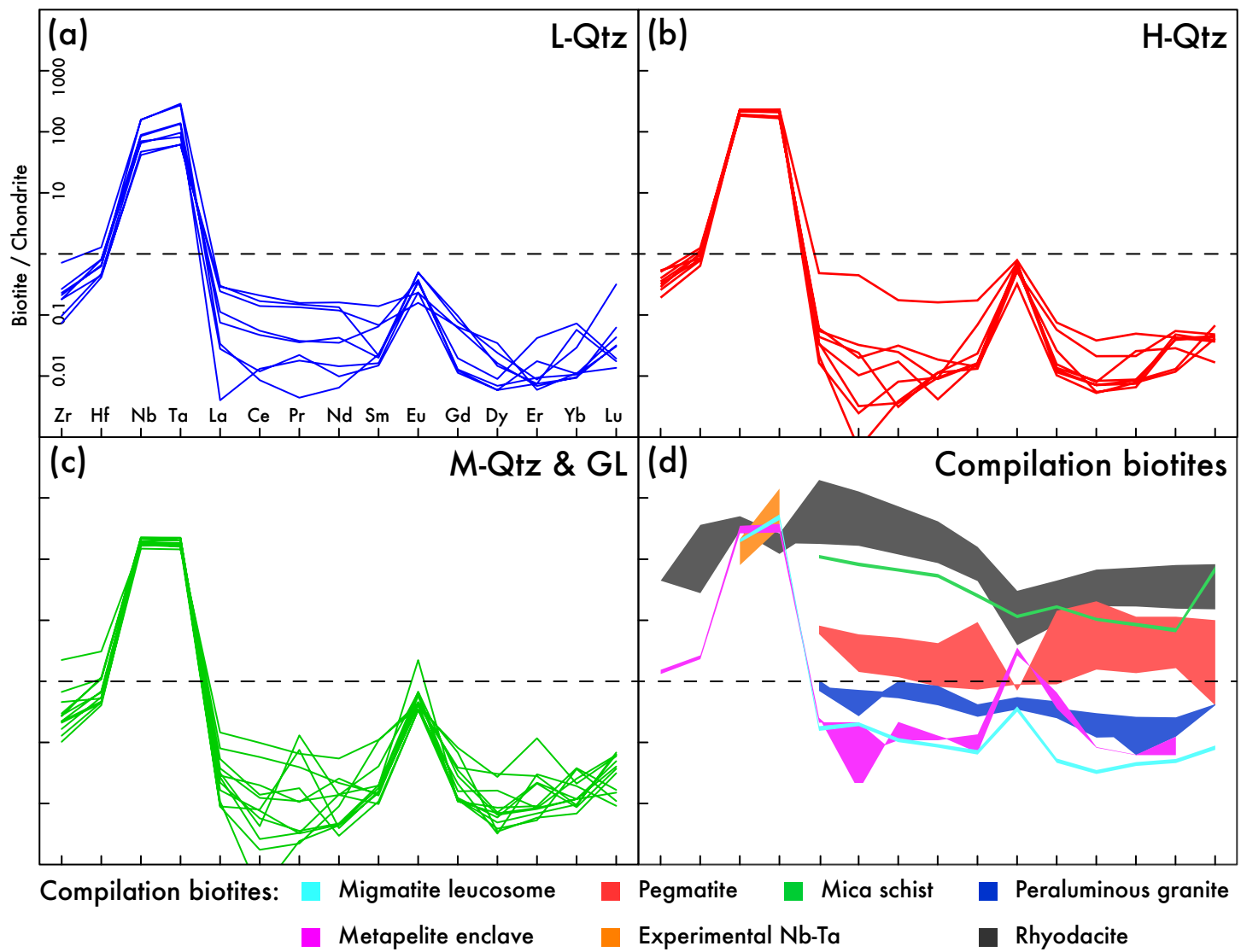
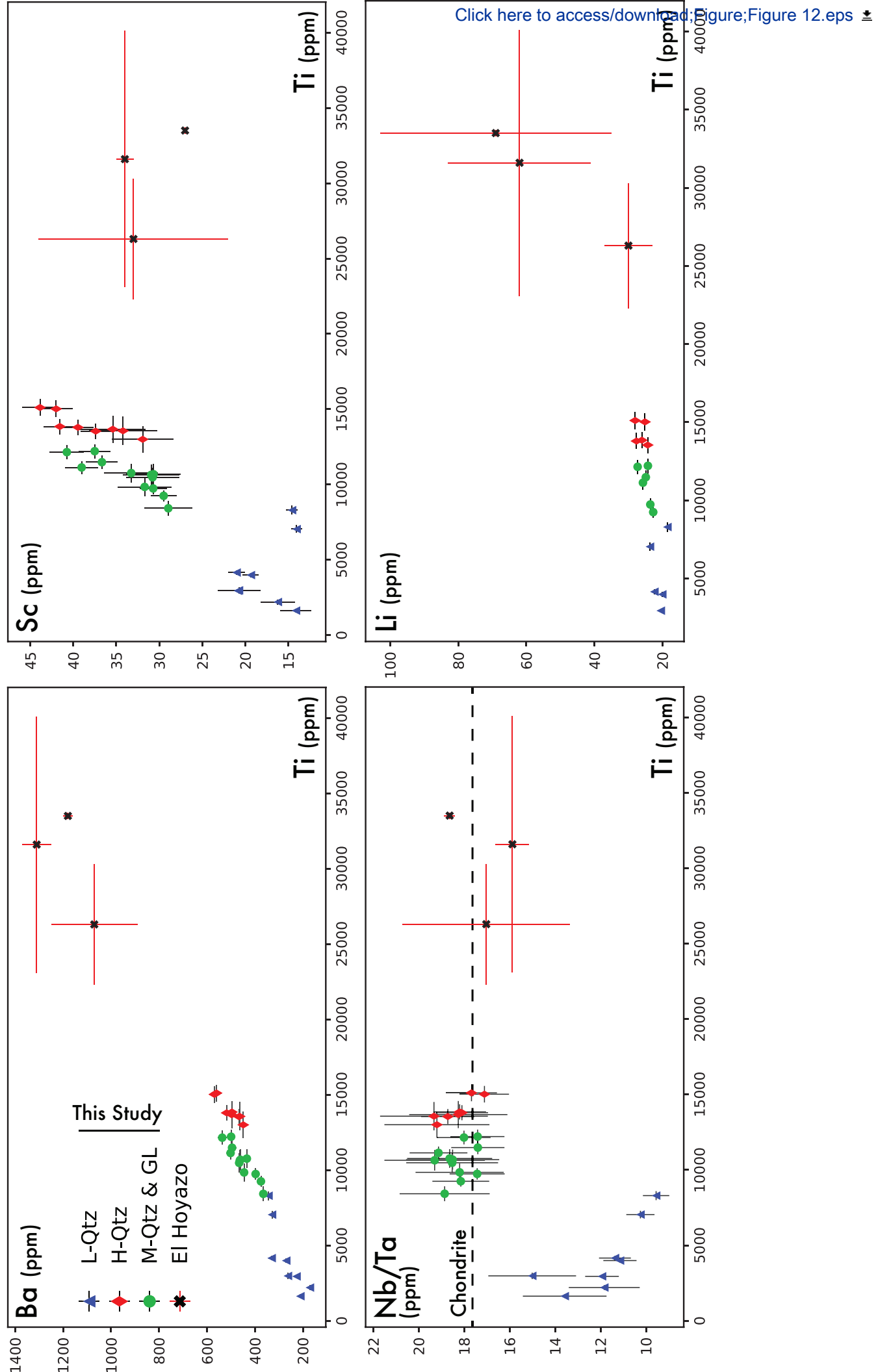
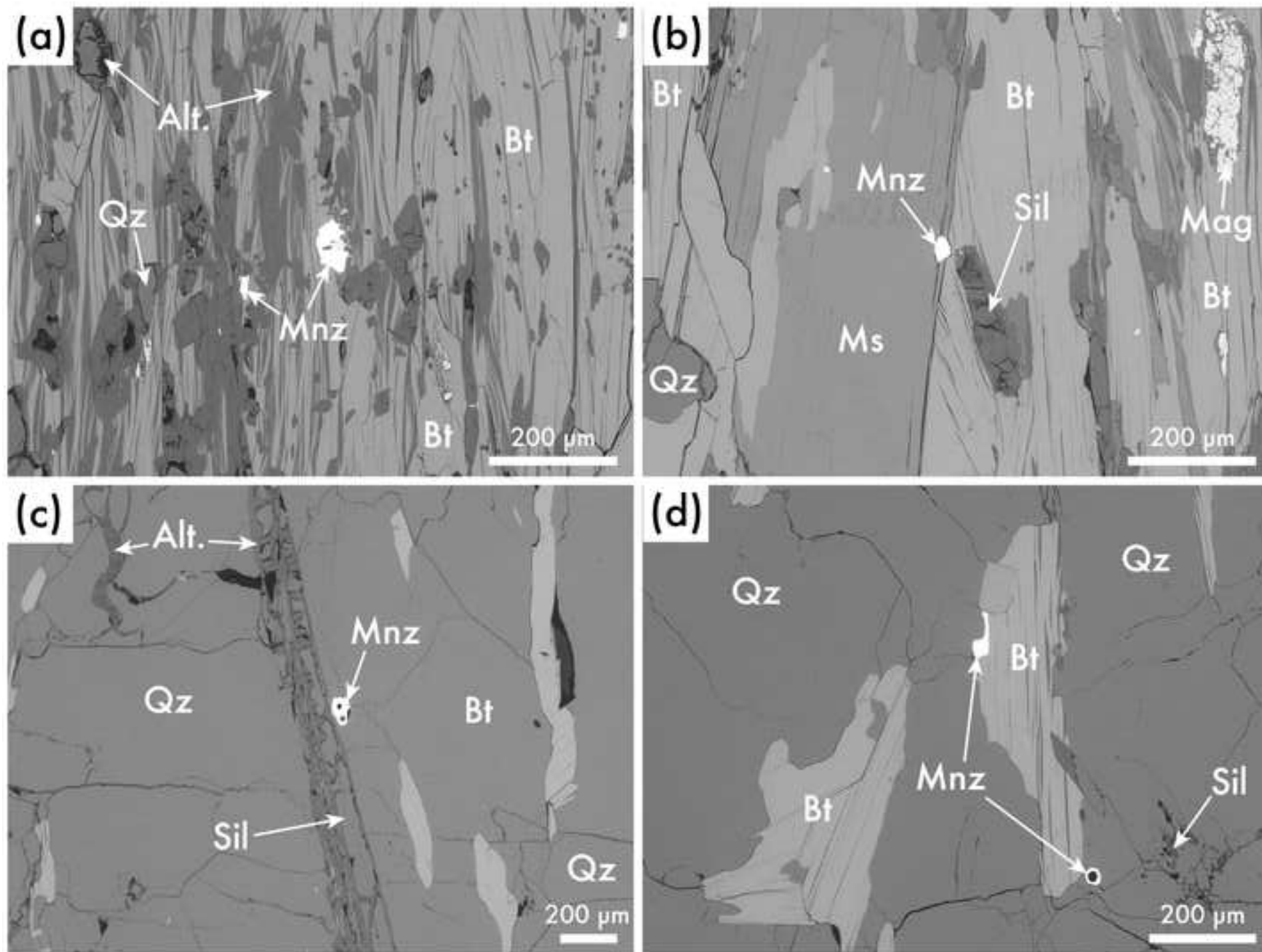
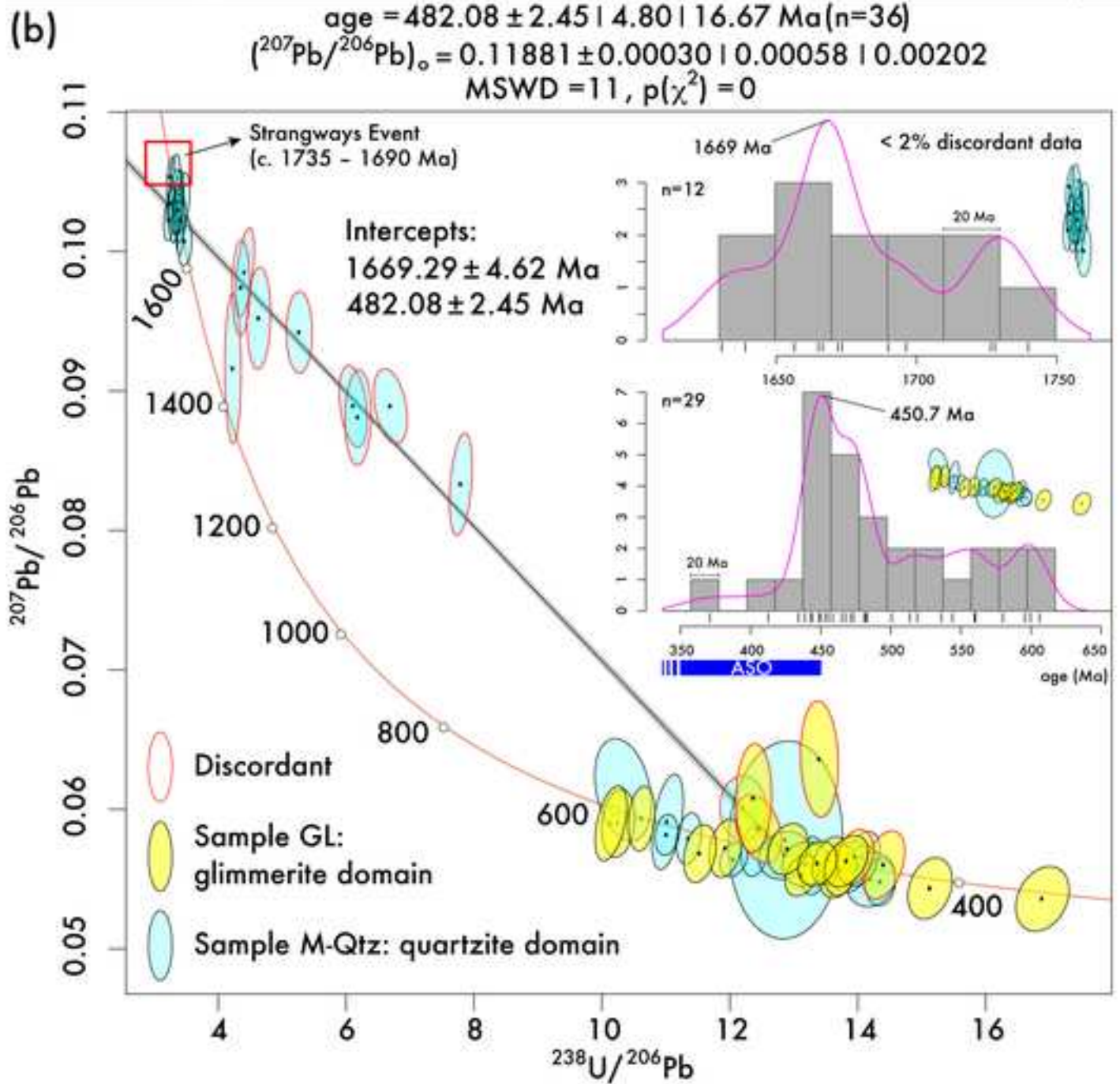
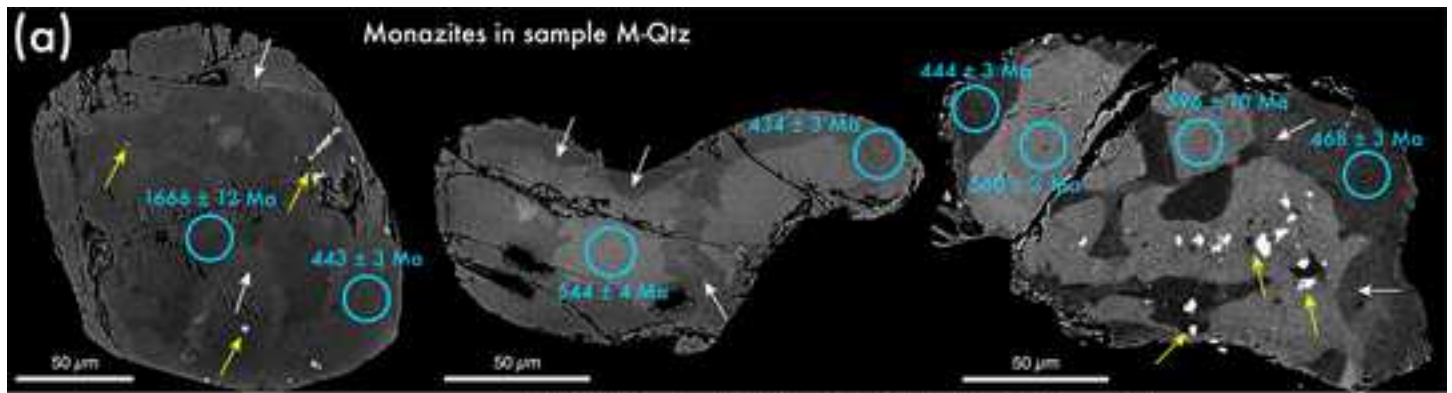
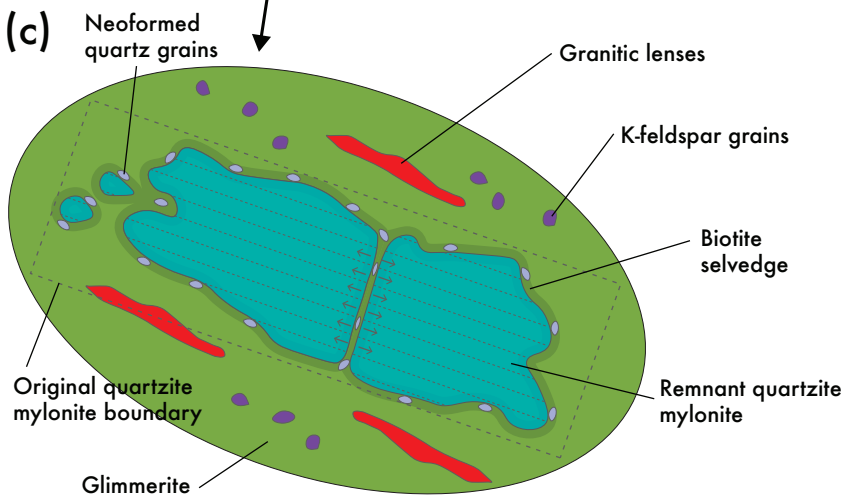
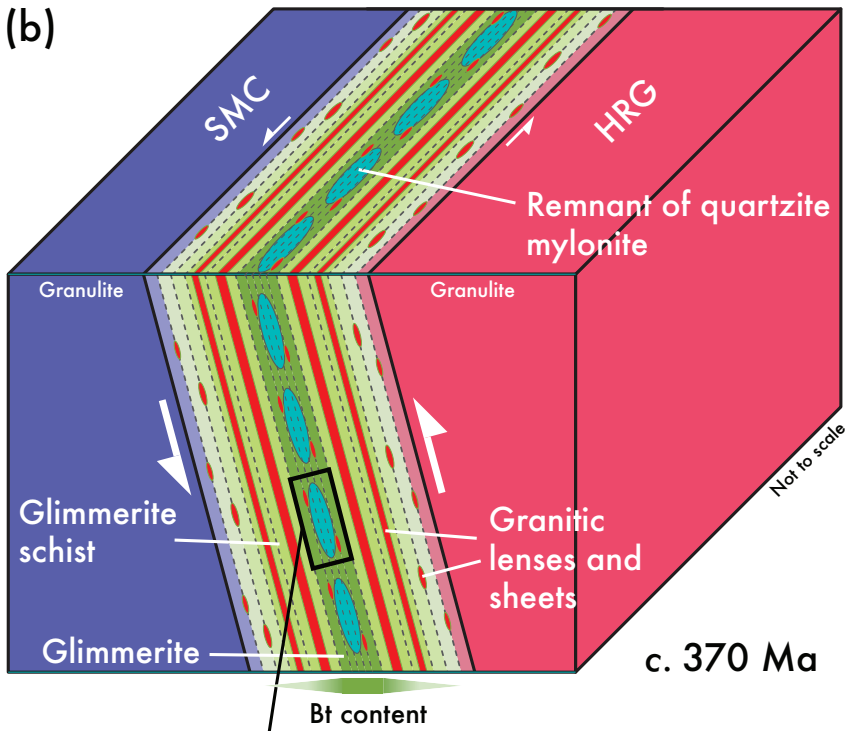
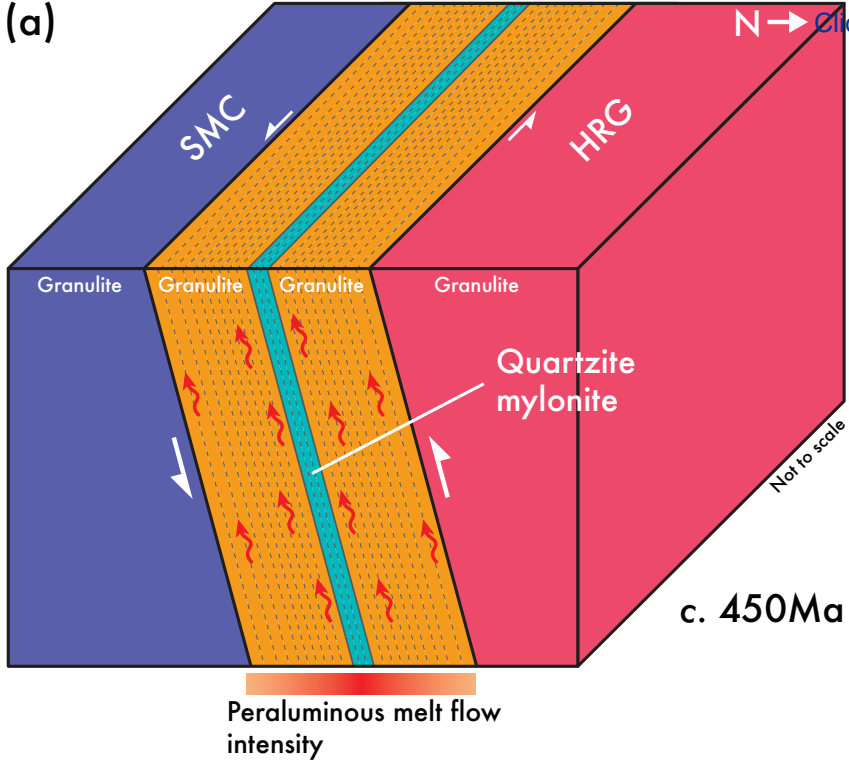


Figure 12









**Table 1:** Electron microprobe data of key minerals from the reacted quartzites and glimmerite seams in the Gough Dam shear zone.

Sample <i>Mineral</i>	L-Qtz		H-Qtz			M-Qtz			GL		
	<i>Bt</i>	<i>Mag</i>	<i>Bt</i>	<i>Ms</i>	<i>Pl</i>	<i>Bt</i>	<i>Ms</i>	<i>Sil</i>	<i>Bt</i>	<i>Ms</i>	<i>Sil</i>
SiO <sub>2</sub> wt%	36.74	–	35.70	44.49	62.89	35.89	44.55	36.03	35.64	44.56	36.06
TiO <sub>2</sub>	0.83	0.03	2.35	0.86	–	1.86	0.60	–	1.97	0.60	–
Al <sub>2</sub> O <sub>3</sub>	17.49	0.43	18.23	32.82	23.00	18.28	33.32	63.23	18.36	33.07	63.41
V <sub>2</sub> O <sub>3</sub>	–	0.06	0.05	–	–	0.06	0.03	–	0.04	0.03	–
Cr <sub>2</sub> O <sub>3</sub>	–	–	–	–	–	–	–	–	0.04	–	–
FeO <sub>total</sub>	13.92	92.19	16.22	3.24	0.05	15.70	3.36	0.84	15.20	3.21	0.83
NiO	–	–	–	–	–	–	–	–	0.06	–	–
MnO	0.05	0.07	0.07	–	–	0.06	–	–	0.05	–	–
MgO	15.32	0.06	12.15	0.97	–	12.53	0.96	–	12.66	0.90	–
CaO	0.03	–	–	–	3.67	–	0.02	–	–	–	–
Na <sub>2</sub> O	0.16	–	0.19	0.51	9.36	0.26	0.63	–	0.23	0.56	–
K <sub>2</sub> O	9.72	–	9.86	10.53	0.19	9.82	10.00	0.01	9.79	10.63	–
P <sub>2</sub> O <sub>5</sub>	–	–	–	–	0.07	0.03	–	–	–	–	–
SO <sub>3</sub>	–	–	–	–	–	–	–	–	–	–	–
Cl	0.26	–	0.18	–	0.02	0.18	0.06	–	0.19	0.02	–
F	0.92	–	0.67	0.06	–	0.66	0.12	–	0.71	0.08	–
O	-0.45	0.04	-0.32	-0.03	-0.02	-0.32	-0.07	0.00	-0.34	-0.04	-0.01
H <sub>2</sub> O	3.99	0.00	3.96	4.45	0.00	3.97	4.45	0.00	3.98	4.45	0.00
<i>Total</i>	<i>98.99</i>	<i>92.89</i>	<i>99.30</i>	<i>97.89</i>	<i>99.25</i>	<i>99.00</i>	<i>98.04</i>	<i>100.11</i>	<i>98.57</i>	<i>98.07</i>	<i>100.30</i>

Mineral abbreviations follow Whitney & Evans (2010). (–): Below detection limit. The complete dataset is available in Supplementary Material, Table S1.

**Table 2:** Representative LA-ICP-MS trace element and REE compositional data for biotite grains from the Gough Dam shear zone, and comparison to published data from multiple locations and formation settings exogenous to the study area.

Sample	Gough Dam shear zone			Compilation of published biotite compositions						
	L-Qtz (GD1609A)	H-Qtz (GD1609B)	M-Qtz & GL (GD1609C)	Two-mica granite <sup>(1)</sup>	Diatexite migmatite <sup>(2)</sup>	Metapelite xenolith <sup>(3)</sup>	Pegmatite <sup>(4)</sup>	Mica schist <sup>(5)</sup>	Rhyolite/ Rhyodacite <sup>(6)</sup>	Experiment <sup>(7)</sup>
Zr	0.21	0.35	0.28	--	--	1.41	--	--	40.05	--
Hf	0.66	0.96	0.66	--	--	2.52	--	--	27.77	--
Nb	85.13	221.75	188.88	--	197.08	341.67	--	--	283.33	208.33
Ta	134.71	216.18	183.09	--	462.50	323.53	--	--	119.85	1397.06
La	--	0.016	0.009	0.717	0.169	0.253	7.890	107.173	342.194	--
Ce	0.013	0.002	0.002	0.277	0.196	0.016	5.726	81.240	274.062	--
Pr	0.018	0.008	--	0.970	0.108	0.216	5.065	--	--	--
Nd	0.014	0.009	0.009	0.700	0.088	0.131	4.136	52.516	133.479	--
Sm	--	--	0.107	0.405	0.068	0.068	8.851	24.662	53.243	--
Eu	0.357	0.702	0.444	0.533	0.355	2.664	0.710	11.368	7.105	--
Gd	--	--	0.068	0.452	0.050	0.653	13.920	16.332	--	--
Dy	--	--	--	0.122	0.033	0.081	19.553	10.163	17.195	--
Er	0.018	--	--	0.125	0.044	0.063	11.000	--	--	--
Yb	--	--	--	0.124	0.050	0.124	10.932	6.832	15.466	--
Lu	0.043	0.067	0.031	--	0.081	--	9.756	69.106	15.041	--

REE and trace elements values were normalised using McDonough & Sun (1995) chondritic values.

(1) Bea *et al.*, 1994a; (2) Bea *et al.*, 1994b; (3) Acosta-Vigil *et al.*, 2010; (4) Hulsbosch *et al.*, 2014; (5) Lau & Lepel, 1987; (6) Nash & Crecraft, 1985;

(7) Stepanov & Herman, 2013. The complete dataset is available in Supplementary Material, Table S3. (–): Below detection limit; (–): Not available.

**Table 3:** Calculation of the melt volume forming hydrous minerals in a high-strain zone 1

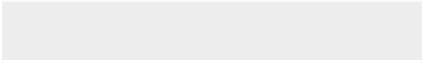
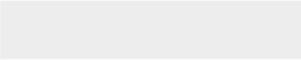
<i>Sample</i>	<b>Hydrous minerals wt%</b>	
	<i>L-Qtz</i>	<i>H-Qtz</i>
Biotite (3.97 H <sub>2</sub> O wt%)	8.0	15.0
Muscovite (4.44 wt%)	0.0	2.0
<i>Total sample H<sub>2</sub>O (wt%)</i>	<i>0.32</i>	<i>0.68</i>
<b>Melt H<sub>2</sub>O (wt%)</b>	<b>Volume of melt per m<sup>3</sup> rock</b>	
	3.0	0.11
	6.0	0.05
	9.0	0.04
	12.0	0.03

for samples L-Qtz and H-Qtz.





Click here to access/download  
**e-component**  
Table S1.xlsx





Click here to access/download  
**e-component**  
Table S2.xlsx



Click here to access/download  
**e-component**  
Table S3.xlsx



Click here to access/download  
**e-component**  
Table S4.xlsx



Click here to access/download  
**e-component**  
Table S5.xlsx